Structural rearrangements upon opening of Channelrhodopsin-2

Im Fachbereich Physik der Freien Universität Berlin
eingereichte Dissertation zur Erlangung des Grades
eines Doktors der Naturwissenschaft (Dr. rer. nat.)

vorgelegt von

Nils Krause

Januar 2016

Erster Gutachter: Prof. Dr. Joachim Heberle

Zweiter Gutachter: Prof. Dr. Robert Bittl

Tag der Disputation: 13.04.2016

Das Projekt wurde in der Arbeitsgruppe von Dr. Ramona Schlesinger am Fachbereich Physik der Freien Universität Berlin durchgeführt und durch die Deutsche Forschungsgemeinschaft im Rahmen des Sonderforschungsbereiches 1078 „Protonation Dynamics in Protein Function“ gefördert.

Publications related to the PhD project:

Published:

1. Lorenz-Fonfria, V. A., Resler, T., Krause, N., Nack, M., Gossing, M., Fischer von Mollard, G., Bamann, C., Bamberg, E., Schlesinger, R., and Heberle, J. (2013) Transient protonation changes in channelrhodopsin-2 and their relevance to channel gating. *Proceedings of the National Academy of Sciences of the United States of America* **110**, E1273-1281

2. Krause, N.[#], Engelhard, C.[#], Heberle, J., Schlesinger, R., and Bittl, R. (2013) Structural differences between the closed and open states of channelrhodopsin-2 as observed by EPR spectroscopy. *FEBS letters* **587**, 3309-3313

3. Volz, P.[#], Krause, N.[#], Balke, J., Schneider, C., Walter, M., Schneider, F., Schlesinger, R., and Alexiev, U. (2016) Light and pH-induced changes in structure and accessibility of transmembrane helix B and its immediate environment in Channelrhodopsin-2. *The Journal of biological chemistry*

#: Both authors contributed equally.

Table of Contents

APPENDIX 125

1 Introduction

Channelrhodopsins (ChRs) are ion channels that have been shown to regulate phototaxis of green algae (1,2). The functional unit comprises a retinal chromophore embedded in Seven Transmembrane Helices (7TM). Up to now ChRs are the only light gated ion channels found in nature. After the discovery in 2003 (3) it was soon exploited as a tool to trigger nerve cell action potentials (4). A new field of research, named optogenetics, was established. *Pubmed* lists about 500 published articles related to optogenetics in 2015. A number that manifests the heavy interest in this young research field. ChRs can be used to modulate and shape nerve cell activity in order to understand neurological processes and counteract neurological dysfunctions (4,5).

The 7TM architecture of ChRs is wide spread in nature. A diverse set of functionalities is associated with the 7TM blueprint: In prokaryotes microbial rhodopsins are able to pump protons (bacteriorhodopsin) and chloride (halorhodopsin) over the membrane. Thus light energy is converted into an electrochemical gradient (6). Other microbial rhodopsins control phototaxis of some halobacteria (sensory rhodopsin) (7,8). In eukaryotes 7TM proteins are responsible for the reception of light both in visualization (visual rhodopsin) and synchronization of the circadian rhythm (melanopsin) (9). Additionally, the superfamily of G-Protein Coupled Receptors (GPCRs) communicates the recognition of various stimuli in form of intracellular signaling cascades. These processes are crucial for photo- and olfactory sensation, but also for regulation of homeostasis and the modulation of neuronal functions (10). Basic research yielding molecular mechanistic understanding of members of this family will have implications for a broad range of research fields including applications like rational design of GPCR ligands in drug discovery. Because ChRs undergo a cyclic reaction triggered by light they can be used for a large set of different biophysical techniques. Thereby they are ideal candidates to study the structure-function relationship on molecular level.

1.1 Channelrhodopsin 2

The best studied ChR originates from *Chlamydomonas reinhardtii*, a unicellular green alga and plant model organism (3). In *C. reinhardtii* two ChR isoforms were found to be located in the plasma membrane of the so-called “eyespot” equatorial to the flagellar axis (Figure 1) (11). Below the plasma membrane carotenoid granula reflect photons back on the photoreceptors. The eyespot rotates around the flagellar axis which provides the propelling force for cell motility (Figure 1). This rotation leads to a light-dependent modulation of the membrane potential by ChR2, which is enforced by voltage gated cation channels. The modulation regulates the flagellar movement (11). The native ChR isoforms consist of about 700 amino acids, half of which belong to a hydrophilic domain that protrudes into the cytosol (3). The hydrophilic domain has no role in ion channeling and is believed to bind the cytoskeleton to ensure localization in the eyespot. Thus, in optogenetics and biophysics the first ~300-350 amino acids of the N-terminus of ChR2 are used. A low resolution structure of ChR2 shows it as a homodimer with helices C and D at the dimeric interface (12). In 2012 the X-ray crystal structure of the transmembrane part of a ChR was published. The crystallized protein consists of the first five helices of ChR1 and the last two helices f ChR2 from *C. reinhardtii*. Channelrhodopsin 1 and 2 are homodimeric protein

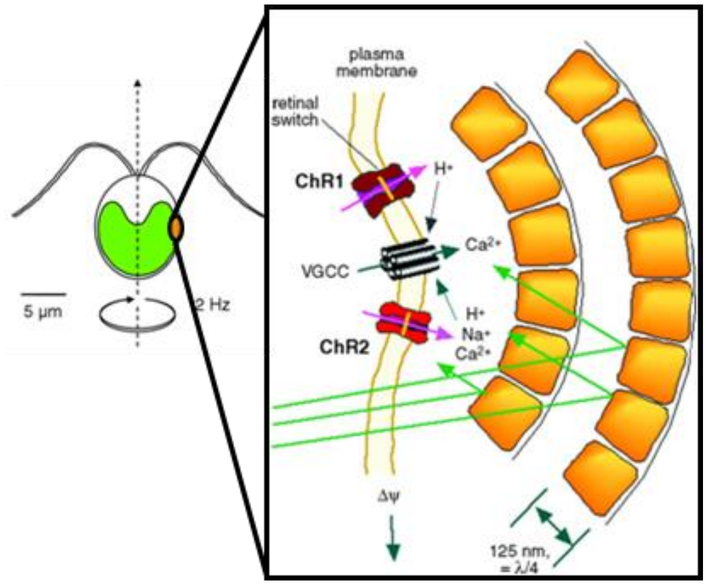

Figure 1: Organization of the eyespot: The plasma membrane, featuring ChR-1, -2 and a voltage gated cation channel (VGCC), is underlayed with several layers of carotenoid granula. Reproduced from (16).

complexes in which the monomers are covalently connected by three and two disulfide bridges (13), respectively.

1.1.1 The photocycle intermediates

The conductance of cations through the membrane, thus emergence of a photocurrents results from a cyclic reaction initiated by light absorption. In order to characterize the basic events that lead to channel opening, nanosecond LASER pulses were employed to excite ChR and observe thermal relaxation (single turnover conditions). Under continuous illumination a mixture of intermediate states accumulate and the photocycle might branch to additional intermediates ((14) is reviewing the biophysical perspective on single and multi turnover). Therefore, although it is closer to “native” conditions, continuous illumination complicates the interpretation of spectroscopic results. The reaction cycle discussed in the following refers to single turnover conditions. It comprises four intermediates P_1^{500} – P^{480} which were identified by the shift of the retinal UV/Vis absorption (15). These intermediates reflect certain changes in the retinal binding pocket or retinal itself. Photocycle intermediates are numbered by the order of their appearance and labeled with the UV/Vis absorbance maximum (Figure 2). The retinal chromophore is bound to lysine 257 (K257) via a Schiff base (13). In the dark-adapted ground state ChR2 shows a population of all-trans retinal of up to 100% (16-18) with only minor fractions of cis-isomerized species. However, it was shown that the light induced all-trans to 13-cis isomerization drives the photocycle (19).

After absorption of a photon all-trans retinal isomerizes to 13-cis retinal. The absorption is red-shifted from 470 nm (ground state) to 500 nm in the first intermediate, P_1^{500}. Formation of P_1^{500} takes place within picoseconds after the light absorption. FTIR light-dark difference spectra show substantial band changes in the amide I region, which are suggested to indicate changes in the hydration of the protein backbone and/or some extent conformational changes (20).

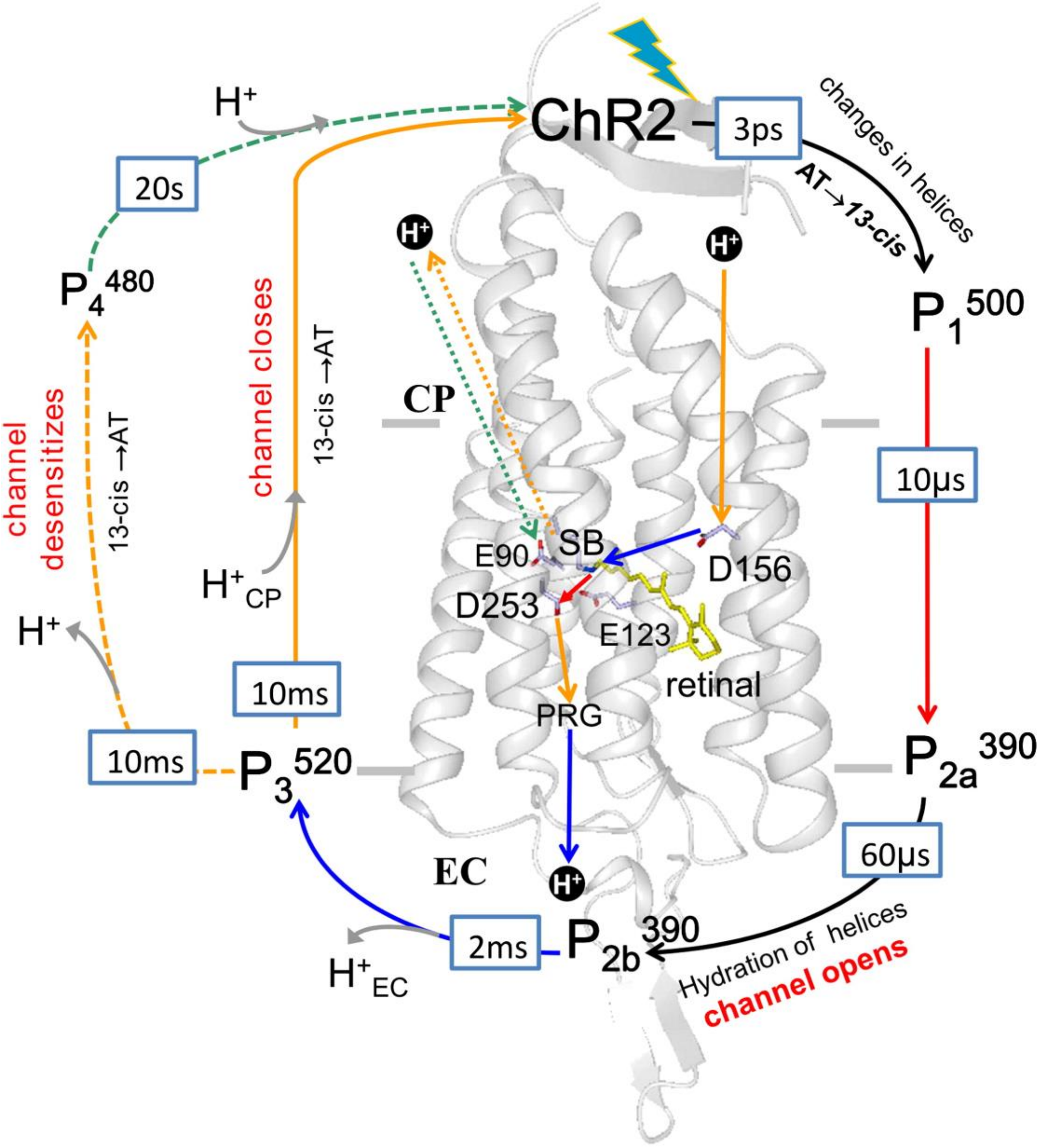

Figure 2: The photocycle (under single turnover conditions) of ChR2-WT summarizing the recent findings of protonation events and helix hydration (18). The cycle starts from ground state, “ChR2”. After illumination, as indicated by the blue flash, the retinal isomerizes from all-trans (AT) to 13-cis retinal. The time constants for the transitions from one intermediate to the other (arrows) are demarced in the rectangles. Protonation events coinciding with certain transitions in the photocycle are denoted by arrows in the same color as the transition. The dashed arrows of the transition to P_4^{480} indicate that only 25% of the protein population go along this reaction branch. Reproduced from (18).

Subsequently, deprotonation of the retinal Schiff base gives rise to the blue-shifted P_{2a}^{390} intermediate (τ~10 µs). After deprotonation of the Schiff base difference bands in the amide I region are observed (P_{2b}^{390} with τ~60 µs). These differences were assigned to the hydration of α–helices and suggested to correspond to pore formation and channel opening (21). In a second phase helix hydration reaches a maximum (τ~2 ms), which was observed to coincide with the maximal conductance in electrophysiological experiments. Furthermore, reprotonation of the retinal Schiff base by aspartate 156 (D156) and the concomitant red-shift of the retinal absorption was observed, which indicates the formation of P_3^{530}. With the decay of P_3^{530} (τ~10 ms) the photocycle splits in two branches, both promoting the relaxation of 13-cis retinal into all-trans (15). 75% decay directly from P_3^{530} to ground state. With a probability of 25% back isomeration coincides with the deprotonation of glutamate 90 (E90) and gives rise to a comparatively stable intermediate P_4^{480}. The amplitude of the amide I difference bands is similar to P_3^{530} thus indicating similar hydration patterns (15). P_4^{480} is the most long lived state and decays with τ~10s.

1.1.2 The Channel Activity – Electrophysiological Measurements

In optogenetics and electrophysiology continuous illumination is used to achieve current densities with a sufficient ratio of signal to noise. Thus, the excitation light can interfere with several intermediates or even induce multiple turnover. Under continuous illumination as depicted in Figure 3 the photocurrents of wild-type ChR2 reach a maximum after a few ms (I_p) and decrease in less than 100 ms to a steady state level (I_{ss}) ("desensitization"). The current density of a downstream illumination cycle depends on the duration of the irradiation break in between cycles. If the break is shorter than ~15 s the current amplitude is smaller compared to the first cycle ("light-adaption" (22,23)). Since P_4^{480} was spectroscopically shown to accumulate under continuous illumination (24) and its lifetime is in the same range as the light-adaption, it is discussed to be the desensitized state. The maximum turnover of 4 x 10^4 Na^+/s at -60 mV (14) is in the same order of magnitude as in on-transporters like

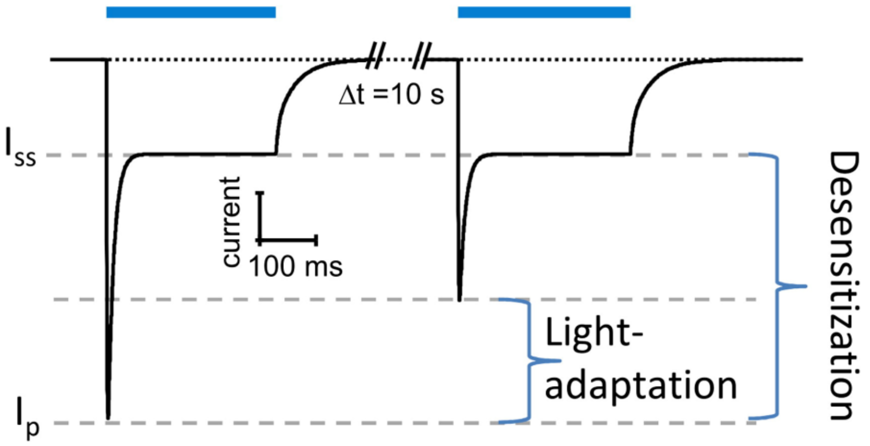

Figure 3: Scheme of a photocurrent measurement. The scheme is typical for an electrophysiological measurement in voltage clamp mode at a negative holding potential. Illumination (blue bars on top) give rise to a negative photocurrent (cation influx). Reproduced from (18).

e.g. ClC-ec1 (25). ChR2 is not very selective and also channels protons (26). The conductance is inversely proportional to the radii of passing ions, which indicates that most of the hydration shell is stripped away by some selectivity filter (26). On the basis of the conductance/ion radii relationship the diameter for this constriction was estimated to be ~6.2 Å (26).

1.1.3 Structural determinants of pore opening

The overall scaffold of ChR in the ground state is similar to bacteriorhodopsin with the exception of helix A and B being tilted outwards (13). This allows for an electronegative hydrophilic funnel between the helices A, B, C and G intruding towards the Schiff base in the middle of the transmembrane region. Helix B features a motif of seven polar residues that face towards helices C and G and account for the electronegativity of the half-channel. Next to the Schiff base the pore is lined by the side chain of glutamate 90 (E90), which is held in place by hydrogen bonding with asparagine 258 (N258), jointly referred to as “central gate” (13). The so-called “inner gate” is formed by tyrosine 70 (Y70), whose phenol ring blocks water influx and the glutamates E82 and E83 with their respective hydrogen bonding partners histidine 134 (H134) and arginine 268 (R268) (27,28). The inner gate is located close to the cytoplasmic interface at the putative pore exit. In order to assure a minimum pore diameter of 6.2 Å (26) major conformational rearrangements are expected.

Slightly remote from the pore, cysteine 128 (C128) and aspartate 156 (D156) have been shown to crucially influence the photocycle kinetics. Side directed mutagenesis leads to a dramatic (up to 10^4 fold) slowdown in the decay of P_2^{390}/P_3^{530} and prolonged photocurrents (29-32). For optogenetic purposes these mutations increase the light sensitivity (32). Both residues have been shown to be hydrogen bonded to each other and are referred to as “DC Gate” (30). The variant with C128 substituted by threonine (ChR2-C128T) has been shown to accumulate P_3^{530} under continuous illumination (29,31). This substitution is frequently used to make the open state of ChR2 more accessible and to study its characteristics (30,34,35).

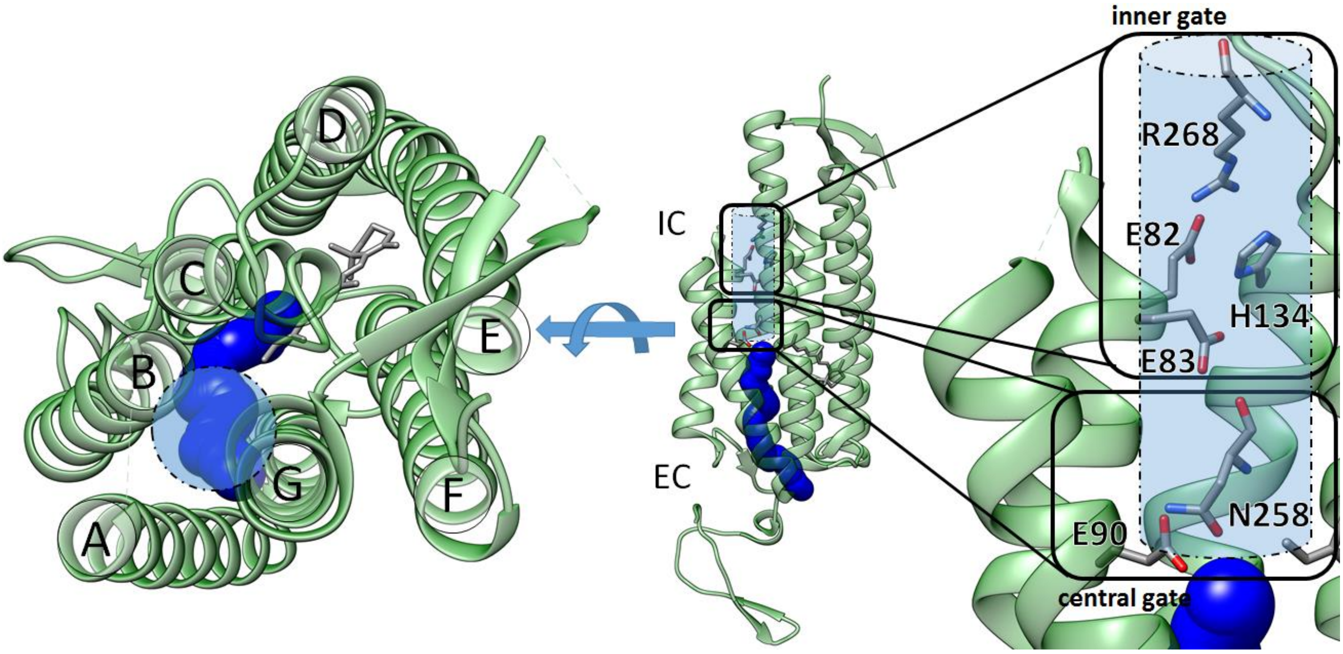

Figure 4: The funnel in ChR2: Hydrophilic pore (dark blue) in the ChR chimera structure (PDB: 3UG9) The pore is located between helices A, B, C and G, as well as the assumed pore elongation after channel opening (light blue). Inner and central gate refer to the constriction sites that prevent a continous pore.

1.2 *The aims of this thesis*

In recent years a lot of knowledge about ChR2 was established: The ground state structure of a ChR variant was solved in high resolution. The role of several residues was characterized by electrophysiological studies and specific dynamics of certain residues (e.g. hydrogen bonding, protonation/deprotonation) were described by FTIR. On this basis an increasing amount of *in silico* studies tries to model the dynamics of ChR. For the design and evaluation of these models experimental data of the structural dynamics during channel opening is of crucial relevance. In this thesis cysteine variants for side directed spin labeling were engineered. As depicted in Figure 5, spin-spin distance measurements were conducted in the closed and open state to locate structural rearrangements.

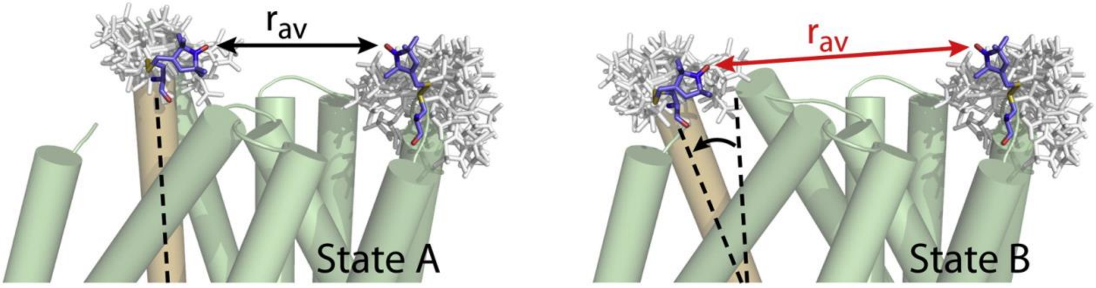

Figure 5: Schematic depiction of the experimental approach in this thesis. Reproduced from (36).

2 Material and Methods

2.1 Material

In times of a broad market of lab supplies and successful standardization of most commonly used chemicals a comprehensive list of all chemicals used is redundant. The same holds true for the basic lab equipment, where with the given parameter in the following routines are easily transferable from one manufacturer to the other. This section provides a list of rare or sensitive chemicals, buffers, media and sensitive equipment.

2.1.1 Chemicals

Designation	full name	Supplier
BHI BHI agar	Difco Brain Heart Infusion Difco Brain Heart Infusion agar	Becton, Dickinson and Company, Sparks, Maryland, USA
DM	n-Decyl-β-D-Maltopyranoside	GLYCON Biochemicals, Luckenwalde, Germany
gelred	GelRed™ nucleic acid gel stain	Biotium, Hayward, California, USA
MTSL	(1-Oxyl-2,2,5,5-tetramethyl-Δ3-pyrroline-3-methyl) Methanethiosulfonate	Toronto Research Chemicals, Toronto, Canada
Protease Inhibitor tablet	cOmplete Protease Inhibitor Cocktail Tablets	Roche, Mannheim, Germany
Restriction enzymes	FastDigest restriction enzymes	Life Technologies GmbH, Darmstadt, Germany
YNB	Yeast Nitrogen Base	Carl Roth, Karlsruhe, Germany

2.1.2 Plasmids

Designation	Organisms	Selectable marker	Manufacturer
pET28a	*E. coli*	Kanamycin	Merck Millipore, Billerica, Massachusetts, USA
pPIC9K	*E. coli* *P. pastoris*	Kanamycin G418	Life Technologies GmbH, Darmstadt, Germany

2.1.3 Strains

Designation	Genotype	Selectable marker	Manufacturer
P. pastoris:			
SMD1163	Δ*his4* Δ*pep4* Δ*prb1*	Histidine auxotroph	Life Technologies GmbH, Darmstadt, Germany
E. coli:			
Top10	F- *mcrA* Δ(*mrr*-*hsd*RMS-*mcr*BC) Φ80*lac*ZΔM15 Δ *lac*X74 *rec*A1 *ara*D139 Δ(*araleu*)7697 *gal*U *gal*K *rps*L (StrR) *end*A1 *nup*G		Life Technologies GmbH, Darmstadt, Germany
BL21-CodonPlus(DE3)-RIL	*argU* (AGA, AGG), *ileY* (AUA), *leuW* (CUA)	Chloramphenicol	Agilent Technologies GmbH & Co. KG, Waldbronn, Germany

2.1.4 Buffers

Name	Ingredients
Buffer A	20 mM HEPES pH 7.4 100 mM NaCl
Buffer Ad	20 mM HEPES pH 7.4 100 mM NaCl 0.2% (m/v) DM
Buffer C	20 mM MES pH 6.0 100 mM NaCl
Buffer Cd	20 mM MES pH 6.0 100 mM NaCl 0.2% (m/v) DM
Breaking buffer	50 mM sodium phosphate pH 6.0 1 mM EDTA 5% (v/v) Glycerol
MSP buffer	40 mM Tris-HCL pH 8.0 300 mM NaCl
MSPe buffer	20 mM Tris-HCL pH 7.4 100 mM NaCl 0.5 mM EDTA
TAE	40 mM Tris acetate pH 8.0 0.05 M EDTA
TE	10 mM Tris pH 8.0 1 mM EDTA

2.1.5 Media

Abbreviation	full name	Ingredients
BMGY	Buffered Glycerol-complex Medium	1% (m/v) yeast extract 2% (m/v) peptone added after autoclaving: 100 mM potassium phosphate pH 7.4 1.34% (m/v) yeast nitrogen base (YNB) $4 * 10^{-5}$% (m/v) biotin 1% (v/v) glycerol
BMMY	Buffered Methanol-complex Medium	1% (m/v) yeast extract 2% (m/v) peptone added after autoclaving: 100 mM potassium phosphate pH 7.4 1.34% (m/v) yeast nitrogen base (YNB) $4 * 10^{-5}$% (m/v) biotin 0.5% (v/v) methanol
BHI BHI agar	Brain Heart Infusion Brain Heart Infusion agar	3.7% (w/v) BHI 5.2% (w/v) BHI agar
TB	Terrific broth	1.2% (m/v) tryptone 2.4% (m/v) yeast extract 0.5% (v/v) glycerol added after autoclaving: 89 mM potassium phosphate pH 7.4
MD	Minimal Dextrose	1.34% (m/v) yeast nitrogen base (YNB) $4 * 10^{-5}$% (m/v) biotin 2% (m/v) glucose
MM	Minimal Methanol	1.34% (m/v) yeast nitrogen base (YNB) $4 * 10^{-5}$% (m/v) biotin 0.5% (v/v) methanol
YPD	Yeast extract Peptone Dextrose	1% (m/v) yeast extract 2% (m/v) peptone 2% (m/v) glucose

Agar of the respective medium was prepared by adding 1.5% (w/v) agar.

2.1.6 Equipment

Designation	**Tradename, Manufacturer**
Äkta	Äkta avant 25, GE Healthcare
Äkta size exclusion columns	HiLoad™ superdex 200 16/60 prep grade and superdex 200 10/300 GL, GE Healthcare
Cell Disrupter	Cell Disrupter TS Series, Constant Systems Ltd, Low March, Daventry Northants, United Kingdom
Concentrator	10 kDa/50 kDa, amicon ultra, Millipore, Carrigtwohill, Tullagreen, Ireland
Electroporator	MicroPulser™ Electroporator, Bio-Rad, Hercules, California, USA
Miniprep kit	NucleoSpin® Plasmid, Macherey-Nagel, Düren, Germany
10DG column	Econo-Pac® 10DG Column, Bio-Rad, Hercules, California, USA
50 L-bioreactor	50 L CellMaker Regular, Cellexus

2.2 Biochemical Methods

2.2.1 *Pichia pastoris*/pPIC9K expression system

The over expression of eukaryotic membrane proteins sets high demands on the expression host. Eukaryotic proteins often need posttranslational modifications and membrane proteins depend on machinery that enables the incorporation into the membrane. These requirements exclude *E. coli* as an expression host in many cases. Among the membrane protein structure entries in the Protein Data Bank, yeast cells are the most common expression hosts (37) and remarkably *P. pastoris* is the most often used yeast organism (38). A wide range of ion channels and GPCRs has been successfully expressed in *P. pastoris* (38,39).

The *P. pastoris* expression system used in this work was adapted to ChR2 by Christian Bamann and coworkers (25,40). It comprises the pPIC9k plasmid (Invitrogen) together with the *P. pastoris* strain SMD1163 (Δ*his4* Δ*pep4* Δ*prb1*). The lack of proteinase activity in this strain (Proteinase A, *pep4* and Proteinase B, *prb1*) helps to avoid degradation of recombinant protein (41). The *his4* gene encodes for a histidinol dehydrogenase and the *his4* deficiency turns SMD1163 into a histidine auxotrophic

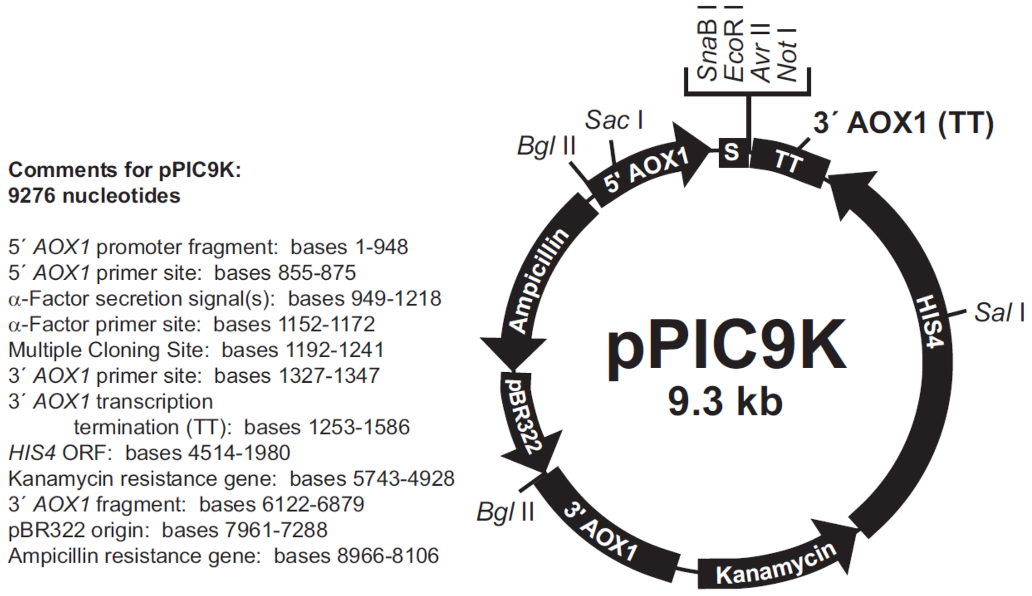

Comments for pPIC9K:
9276 nucleotides

5´ *AOX1* promoter fragment: bases 1-948
5´ *AOX1* primer site: bases 855-875
α-Factor secretion signal(s): bases 949-1218
α-Factor primer site: bases 1152-1172
Multiple Cloning Site: bases 1192-1241
3´ *AOX1* primer site: bases 1327-1347
3´ *AOX1* transcription termination (TT): bases 1253-1586
HIS4 ORF: bases 4514-1980
Kanamycin resistance gene: bases 5743-4928
3´ *AOX1* fragment: bases 6122-6879
pBR322 origin: bases 7961-7288
Ampicillin resistance gene: bases 8966-8106

Figure 6: Vector map for pPIC9K. Reproduced from (42).

strain, which enables to utilize the *his4* gene as a selection marker on the pPIC9K plasmid (Figure 6 (42,43)).

The pPIC9K plasmid is a shuttle vector, featuring an *E. coli* origin of replication and antibiotic resistance cassettes (ampicillin, kanamycin) making cloning in *E. coli* possible. Since *P. pastoris* has no native plasmids the expression construct needs to be integrated into the chromosome (44). Regions homologous to the *P. pastoris* chromosome (*his4*, *aox1*) permit stable integration of the linearized plasmid into the chromosome by homologous recombination. The kanamycin resistance cassette confers a G418 (geneticin) resistance in *P. pastoris*. The multiple cloning sites are located next to the *S. cerevisiae* alpha-mating factor signal sequence, fusing the gene insert to this sequence. The alpha-mating factor signal sequence allows the secretion of soluble proteins and was shown to increase expression of some membrane proteins (45,46).

After digestion with *Sal*I (Figure 6) the linearized plasmid is preferentially transplaced in the *his4* gene of the chromosome (see 2.2.1.2). The transplacement gives a functional *his4* gene and therefore an autotrophic strain. By plating on histidine depleted minimal media agar plates it can be screened for successful transformants. In several cases a correlation between gene dosage and the expression level was observed (44). The probability for multiple insertions is about 1-10% (42). Consequently a second selection screening for multicopy transplacements is done. In this second selection round the G418 resistance is used.

The fusion construct is under the control of the AOX1 promoter. The *aox1* gene codes for the alcohol oxidase 1, which functions as the first enzyme in the methanol metabolism, converting methanol to formaldehyde (47). The AOX1 promoter is methanol induced and leads to high transcription.

2.2.1.1 Mutation of the recombinant ChR2 DNA constructs

The ChR2 constructs used in this work originate from the wild-type sequence of the transmembrane part of the ChR2 (*chop 2* coding for aa residues 1–307 of GenBank accession number AF461397) fused upstream of *chop 2* to the alpha-mating factor signal sequence and downstream to a coding sequence for a 10× His-tag by insertion with *EcoR*I/*Not*I to the pPIC9K vector (Figure 7).

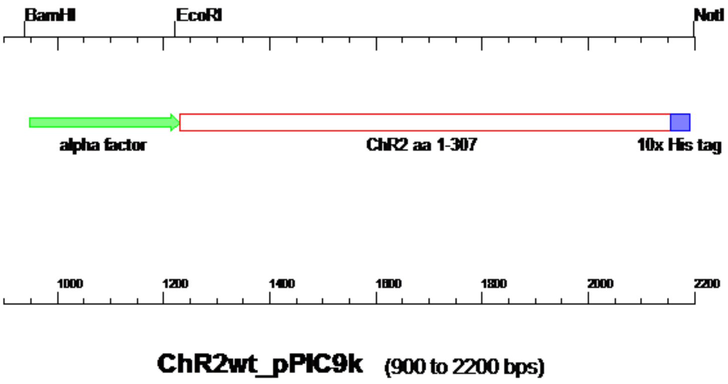

Figure 7: Gene map of ChR2 construct

From the wild-type construct 5 different constructs (C34A/C36A/C79A/C87A, C34A/C36A/C259A, C34A/C36A, C179A/C183A/C259A, CA-C79/C208; see Table 4, p. 46) were incurred from R. Schlesinger having different sets of cysteines exchanged by alanines.

From construct “C79/C208” other mutations for the cysteine-reduced variants were derived by introducing mutations in single codons with the quikchange PCR approach. The mutation Y196F and T159C were directly introduced to the “WT” construct. The quikchange PCR amplifies the whole plasmid using completely or partially complementary primer pairs with a mutated sequence of the template plasmid (Table 1).

1 µL	plasmid template (~100 ng/µL)
1.5 µL (each)	forward and reverse primer (10 pM)
1 µL	nucleotide triphosphate mix (dNTPs, 10 mM)
10 µL	5 times high fidelity Phusion buffer
2.5 µL	DMSO
32 µL	Milli-Q water
0.5 µL	Phusion hot start DNA-polymerase

Cycling program

time	T	
45 s	98°C	
15 s	98°C	18 times repetitions
60 s	60°C	
80 s	72°C	
5 min s	72°C	
forever	4°C	

1 µL of *Dpn*I, a restriction enzyme which cuts only methylated DNA, was added to the PCR product and incubated for 1 h at 37°C. In this step solely the parental template DNA is digested, as it originates from *E.coli* methylating its own DNA. The digested DNA was loaded on a 1% agarose gel in TAE-Buffer with gelred (1:10000 dilution). The DNA band around 10 kb was excised and purified using a gel extraction kit. The purified product DNA was transformed into *E. coli* Top10 cells by electroporation ("EC2" program, 0.2 cm cuvette, 2.5 kV, ~5 ms) with subsequent selection on ampicillin/kanamycin (amp/km) BHI-agar plates. Small cultures (amp/km BHI-medium) of single *E. coli* colonies were inoculated, harvested and plasmid purified according to the instructions of the miniprep kit. Several plasmids from single cell clones were digested with *EcoR*I/*Not*I and analyzed on an agarose gel confirming the right size of the fragments. Plasmids matching the right size were sent for sequencing to verify the successful mutation.

Table 1: Primer used for quikchange mutagenesis (sequence from 5' to 3'). Mutation depicts the sequence position and the amino acid codon, which is introduced at this position.

Mutation	Sequence	Primer name
79T	CCAAACATGGAAGTCAACCACTGGCTGGGAGGAGATC	FPChR2_C79T
	GATCTCCTCCCAGCCAGTGGTTGACTTCCATGTTTGG	GPChR2_C79T
79S	CCAAACATGGAAGTCAACCTCTGGCTGGGAGGAGATC	FPChR2_C79S
	GATCTCCTCCCAGCCAGAGGTTGACTTCCATGTTTGG	GPChR2_C79S
87S	GCGGCTGGGAGGAGATCTATGTGTCTGCTATCGAGATGG	FP_C87S
	GCGGCTGGGAGGAGATCTATGTGTCTGCTATCGAGATGG	GP_C87S
90C	CAGGCCACCGCGTCTGCTGGTTGCGTTACGCCGAG	FP_ChR2E90C
	CTCGGCGTAACGCAACCAGCAGACGCGGTGGCCTG	GP_ChR2E90C
117C	GTGGCTTCTCACCTGCCCGGTCATTCTC	FP_C2_Q117C
	GAGAATGACCGGGCAGGTGAGAAGCCAC	GP_C2_Q117C
128C	CCGAGTGGCTTCTCACCTCTCCGGTCATTCTCATTCACC	FP ChR2 wtC128
	GGTGAATGAGAATGACCGGAGAGGTGAGAAGCCACTCGG	GP ChR2 wtC128
128S	CACGCTGCCAAGGCCTGCATCGAGGGTTACC	FP ChR2 C128S
	GGTAACCCTCGATGCAGGCCTTGGCAGCGTG	GP ChR2 C128S
159C	CACGCTGCCAAGGCCTTCATCGAGGGTTACC	FPT159C_ChR2
	GGTAACCCTCGATGAAGGCCTTGGCAGCGTG	GPT159C_ChR2
159Y	GCCGAAGGGCCGGGCTCGCCAGGTGGTGAC	FPT159Y_ChR2
	GTCACCACCTGGCGAGCCCGGCCCTTCGGC	GPT159Y_ChR2
196C	GCCGAAGGGCCGGACTCGCCAGGTGGTGAC	FP_C2_Y196C
	GTCACCACCTGGCGAGTCCGGCCCTTCGGC	GP_C2_Y196C
196F	GCCGAAGGGCCGGTCTCGCCAGGTGGTGAC	FP_C2_Y196F
	GTCACCACCTGGCGAGACCGGCCCTTCGGC	GP_C2_Y196F
208C	CTATGTGTGCGCTATCTGCATGGTCAAGGTGATTCTCGAG	FP ChR2 C208
	CTCGAGAATCACCTTGACCATGCAGATAGCGCACACATAG	GP ChR2 C208
208T	CTGCTTGTGTCTGATATTGGCTGCATTGTGTGGG	FP ChR2 C208T
	GGAAGTGGCGCCCCACACAATGCAGCCAATATCAGAC	GP ChR2 C208T
208S	CTGCTTGTGTCTGATATTGGCTACATTGTGTGGG	FP ChR2 C208S
	GGAAGTGGCGCCCCACACAATGTAGCCAATATCAGAC	GP ChR2 C208S

2.2.1.2 Transformation of *Pichia pastoris* with pPIC9k-ChR2 constructs and selection of multicopy clones

The pPIC9k ChR2 plasmid was digested with *Sal*I for at least 1h at 37°C:

24 µL	pPIC9k (~100 ng/µL)
3 µL	Fast digest green buffer (10x)
3 µL	*Sal*I (Fermentas)

The digested DNA was desalted and purified from the restriction enzyme by using a miniprep kit. 120 µL AW-buffer (as supplied in the miniprep kit listed in 0, p. 13) were added to the digestion mix, subsequently loaded on a mini prep column and washed and eluted with 30 µL 10 times diluted TE buffer, following the manufacturer instructions. To 40 µL electrocompetent *P. pastoris* cells 10 µL purified DNA was added, incubated for 5 min on ice, transferred into a precooled electroporation cuvette (2 mm) and electroporated using the “PIC” program (5 kV, ~5 ms). Immediately 1 mL cold 1 M sorbitol was added and the resuspended cells were plated on a minimal medium agar plate (MD-agar). After 2-4 days of incubation at 30°C single colonies were visible. The screen for multicopy insertions using the G418 resistance was done in two different ways:

1. The initial protocol in our research group envisaged the successive transfer of single clones from the minimal media plate to nutrient medium agar plates (YPD-agar) with increasing concentrations of G418 as described here (42). Single clones were streaked from the MD-agar plates to YPD-agar plates with 0.1 to 0.2 mg/mL G418. After 1-2 days of incubation at 30°C these clones were streaked on two YPD-agar plates of higher G418 concentration and incubated again as before. This routine was repeated until growth of single colonies at a concentration of 4 mg/mL G418 was achieved.
2. The colonies on the MD-agar plate were resuspended (OD_{600}~0.2) in nutrient medium (YPD) and incubated at 30°C for 1h under agitation. 100 µL of the cell suspension were plated on YPD-agar plates with 0.5 mg/mL G418 and incubated for 3-4 days at 30°C. Single clones were streaked on an YPD-agar plate with 4 mg/mL G418.

The second way saves time and effort. It also allows screening hundreds of clones at once, which is necessary in order to find a clone with the rare event of a multiple insertion. It is an adaption of the Invitrogen^{TM} protocol (42) with the additional step of a 1 h incubation at 30°C. This step was necessary to make the protocol work in our hands. The Invitrogen^{TM} protocol is not optimized for the SMD1163 strain, which is known to be more G418 sensitive compared to not protease deficient strains (48).

The level of resistance is dependent on the cell density. For that reason the G418 screen can give false positive results. Additionally small differences in gene copy number can lead to dramatic differences in the expression level (49). Thus, as the last step of clone selection every clone needs to be checked for target protein expression. Most of the ChR2 variants including the C128T mutation have an absorption maximum at 480 nm and appear red. SMD1163 cells itself have a slightly beige color. Therefore for these variants a ~10 mL expression culture is sufficient to check for red appearance. Clones with variants featuring the wild-type C128 are yellow in color and needed to be checked for expression levels by purification of a 3-5 L expression culture, since we failed in establishing a western blot protocol relying in these constructs only on the poly-HIS tag as epitope, because we had no specific antibody available. For the detailed expression protocol see 2.2.1.3.

From clones, exhibiting the highest expression, the total DNA (including the genomic DNA, gDNA) was extracted and the ChR2 genes were amplified by PCR and sent for sequencing. Since usually several variants were prepared in parallel, sequencing of the expression clone was done to exclude a mix-up of variants. The protocol for this procedure was adapted from (50). 30 µL of a 24 h YPD culture were pelleted, resuspended in 100 µL 0.2 M lithium acetate, 1% SDS and incubated for 5 min at 70°C. After addition of 300 µL ethanol (p.a.), the suspension was briefly vortexed and centrifuged for 3 min at 15000xg. The supernatant was discarded, 30 µL TE-buffer were added and the tube was carefully agitated in order to dissolve pelleted gDNA.

Thereafter a PCR was conducted:

1 µL	gDNA template
1 µL (each)	forward and reverse primer (10 pM)
1 µL	nucleotide triphosphate mix (dNTPs, 10 mM)
10 µL	5 times high fidelity Phusion buffer
2.5 µL	DMSO
33 µL	Milli-Q water
0.5 µL	Phusion hot start DNA-polymerase

Cycling program

time	T	
45 s	98°C	
10 s	98°C	35 times repetitions
60 s	65°C	
30 s	72°C	
1 min s	72°C	
forever	4°C	

2.2.1.3 Expression of ChR2 in *Pichia pastoris*

The AOX1 promoter is repressed by glucose and induced by methanol. Accordingly to get maximal induction cells from an YPD culture needed to be derepressed prior to induction. Derepression was achieved by growth in a glucose free medium with glycerol as carbon/energy source (BMGY).

Preculture:

0.5 L BMGY medium in a 2.5 L baffled flask was inoculated with a ~50 mL YPD preculture.

Main culture:

The main culture of ChR2 was done on a small scale (≤12 L) in flask culture (see 1.) or on a larger scale in a 50 L-bioreactor (see 2.).

1. 0.5 L BMMY medium supplemented with 1% methanol and 5 µM all-*trans* retinal in a 2.5 L baffled flask was inoculated in the morning with 50-100 mL of a fresh BMGY preculture. Per flask 7.5 mL methanol supplemented with 1 mM all-*trans* retinal was added in the evening, the next day in the morning and the evening and the following day in the morning during the 48 h of fermentation at 30°C.
2. 45 L of a 1.1x concentrated BMMY supplemented with 1.1% methanol (final concentration) and 5.5 µM all-*trans* retinal in the bioreactor were inoculated in the morning with 5 L of a fresh BMGY preculture. The initial OD_{600} was ~7. 0.5 mL defoamer was added to prevent foam formation. Altogether 0.75 L methanol supplemented with 1 mM all-*trans* retinal was added during the 48 h of fermentation at 30°C. The final OD_{600} was ~40.

Cells were pelleted by centrifugation (6000xg, 10 min) and stored at -80°C.

2.2.1.4 ChR2 purification

The purpose of the purification is to isolate ChR2 proteins from the plasma membranes of the yeast cells. Summarized this process comprises 4 steps:

2.2.1.4.1 *Cell disruption*

The cell and therefore the plasma membranes are fragmented. The frozen cell pellet is thawed, breaking buffer is added and the cell suspension was passed through a cell disruptor 4 times at 2.7 kbar. Passing the cell suspension at high pressure through a small hole to the disruption of the membrane. Protease inhibitors (PMSF 20 µg/mL, benzamidine 10 µg/mL and 1 protease inhibitor tablet/~100g cells) were added. Intact cells and cell debris were pelleted (10 min, 5000xg), passed through the cell disruptor 3-4 times and centrifuged as before.

2.2.1.4.2 *Collecting the membrane*

The membrane fragments are separated from the soluble fractions. The soluble fraction contains large quantities of protein, which are removed. The supernatant from both centrifugation steps was subjected to ultracentrifugation (~4 h, 125000xg).

2.2.1.4.3 *Protein solubilization*

In order to isolate membrane proteins the lipids as membrane protein joining elements has to be removed. The membrane and its accommodated proteins are solubilized with the help of a detergent. The pelleted membrane fraction was homogenized in buffer A (1 g membrane in 10 mL buffer A). 1% (w/v) DM and 2 M urea were added and the suspension was stirred over night at 4°C. The suspension was ultracentrifuged (1h, 125000xg).

2.2.1.4.4 *Isolating ChR2 from other solubilized proteins*

The solubilized ChR2 is isolated using liquid chromatography. At first in an affinity chromatography step, the protein is bound via its C-terminal poly-histidine stretch to a Ni^{2+}-cation, which is immobilized on a solid matrix. By adding imidazole, a competitive ligand of Ni^{2+} in large excess, the protein can be eluted. By size exclusion chromatography the ChR2 purity is further improved and imidazole is removed. The affinity chromatography was in most cases performed on an Äkta avant 25 system (GE healthcare). The 60 mM imidazole were added to the supernatant and it was loaded ~4 times on a Ni-NTA column. Unspecific bound protein was washed away with 5 column volumes (cv) 60 mM imidazole in buffer Ad and 5 cv 120 mM imidazole in buffer Ad.

The bound protein was eluted by a linear imidazole concentration gradient starting from 120 mM to 500 mM over 10 cv using reverse flow. Thereafter the protein solution was concentrated (50 kDa concentrator). Dependent on the purpose of the protein it was subjected to a manual (10DG column) or Äkta (GE healthcare, superdex

200 10/300) automated size exclusion column using buffer Ad. The protein was concentrated to typically 100-200 µM and shock frozen in liquid nitrogen.

2.2.2 Labeling

2.2.2.1 Spin labeling with MTSL

Initial PELDOR measurements were done with the solubilized protein. The labeling procedure for the solubilized protein is described in this section. Later on the measurements were done on nanodisc-reconstituted ChR2, the MTSL labeling for these samples is part of the reconstitution and described in the next section 2.2.3.

To the solubilized protein in buffer Cd a 20 fold excess of MTSL over ChR2-cysteines was added. The protein was incubated at 4°C with gentle agitation overnight. Unbound MTSL was removed by washing in a concentrator using buffer Cd or by size exclusion chromatography (manual 10DG column or on Äkta with Superdex 200 10/300) using buffer Ad.

2.2.3 Nanodisc reconstitution

2.2.3.1 Expression and purification of MSP1D1in *E. coli*

The MSPs can be expressed recombinant in *E. coli* using the widely used pET system, hence the gene is under control of the strong T7 promotor and the expression is induced by IPTG. For further details on the pET expression system refer to (51).

The expression protocol was adopted from (52). 1 L terrific broth (TB) medium (50mg/L kanamycin) was inoculated with 40 mL of an overnight culture of *E. coli* RIL-pET28a-MSP1D1 cells in dYT medium (50mg/L kanamycin) and incubated at 37°C, 250 rpm. After reaching of an OD_{600}~0.8 the expression was induced with 1 mM IPTG and incubated at identical conditions for additional 4 h. The cells were collected by centrifugation at 8000xg for 15 min and stored at -80°C.

The cells were resuspended in buffer MSPa with 1% (v/v) Triton-X100 and 1 mM PMSF. The cells were lysed by sonification pulses in total 8 min with pauses in between to allow the cell suspension to equilibrate with the surrounding ice bath. The lysate was cleared by centrifugation (20 min, 125000xg) and sterile filtration (0.2 µm). The cleared lysate was loaded 4 times on a Ni-NTA column (~5 mL per 1 L of cell culture) and a washing protocol applied of 4 cv of each following:

1. Buffer MSP + 1% (V/V) Triton-X100
2. Buffer MSP + 50 mM cholate
3. Buffer MSP
4. Buffer MSP + 50 mM imidazole

Finally, the protein was eluted applying a linear imidazole gradient starting from 50 mM to 300 mM over 10 cv using reverse flow. Thereafter the protein solution was concentrated (10 kDa concentrator) and subjected to an Äkta (GE healthcare, Superdex 200 16/60) automated size exclusion column using buffer MSPe. The pure protein (typically ~15 mg/L cell culture) was concentrated to 200 µM, shock frozen in liquid nitrogen, lyophilized and stored at -80°C.

2.2.3.2 Reconstitution of ChR2 in DMPC nanodiscs

The protocol was adopted from (53). MSP1D1 (typically 200 µM), 50 mM/100 mM DMPC/cholate and ChR2 (typically 100-200µM) were mixed in a molar ratio of 1 to 55 to 0.5. Cholate (200 mM) was added to adjust the end concentration to 20 mM. All stock solutions added were prepared in buffer MSPe or buffer A. The mix was incubated for 1 h at 25°C. Afterwards bio beads were added (0.5 to 1 g per mL reconstitution mix), for spin-labeling MTSL was added (MTSL/cysteine = 20) and incubated for 2 h at 25°C to remove the detergent. The protein solution was removed from the bio beads using a cannula, concentrated if necessary (volumne≤0.5 mL) and centrifuged for 20 min at 21000xg to remove larger aggregates. The supernatant was loaded on Äkta automated size exclusion column (Superdex 200 10/300). A typical chromatogram is shown in Figure 34. The peak around 11.4 mL was concentrated and buffer exchanged if necessary.

2.3 Biophysical Methods

2.3.1 Spectroscopic methods

Spectroscopy is the examination of the interaction between electromagnetic irradiation and matter. Dependent on the wavelength different energetic transition in molecules can be excited (Figure 8). Ultraviolet/visible (UV/Vis), infrared and electron paramagnetic (using microwave radiation) spectroscopy were employed in this thesis and will be briefly discussed in the following.

2.3.1.1 Optical spectroscopy

In a spectrometer a certain irradiation intensity I_0 is passed through a sample and thereafter the intensity I is measured. The common logarithm of the ratio of I_0 to I is defined as absorbance A. A is proportional to the molar concentration c of an absorbing compound. The relationship is given by the Beer-Lambert law:

$$A = \varepsilon c d = \lg\left(\frac{I_0}{I}\right) \qquad (1)$$

ε is the molar extinction coefficient at a certain radiation energy and d the path length the irradiation has to pass through the sample.

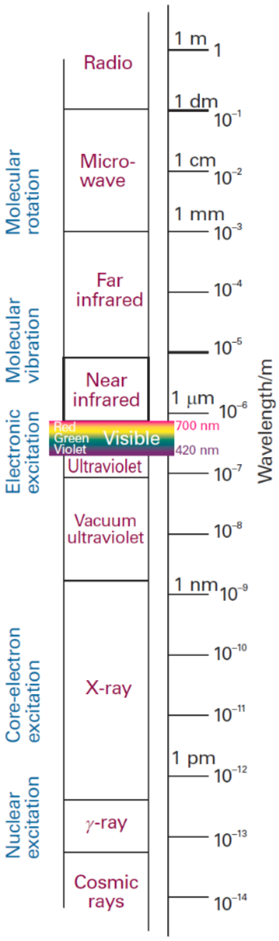

Figure 8: The electromagnetic spectrum and accordant types of excitation. Reproduced from (54).

2.3.1.1.1 *UV/Vis spectroscopy*

The UV/Vis region covers the wavelength from ~10 nm to ~800 nm. UV/Vis light excites electronic transitions in the sample molecule. Typically in protein science UV/Vis spectra are recorded down to ~250 nm. Below 200 nm atmospheric gases start to absorb, which puts additional requirements on the experimental setup. Organic molecules that have high ε in the UV/Vis feature delocalized π–systems. The absorption maximum λ_{max} of all four proteinogenic amino acids that are aromatic, histidine (λ_{max}=211 nm, ε=5700 $M^{-1}cm^{-1}$ (55)), tyrosine, phenylalanine and tryptophan, are in the UV above 210 nm (Figure 9). Equation 1 allows to use absorbance bands to estimate the concentration of molecules. This approach is routinely used to determine protein concentrations by the absorption at 280 nm (like in 3.4.1.3.1, p. 66ff). Here tryptophan has by far the largest ε but also tyrosine, the cystine of disulfide bridges and to a small extent phenylalanine contribute.

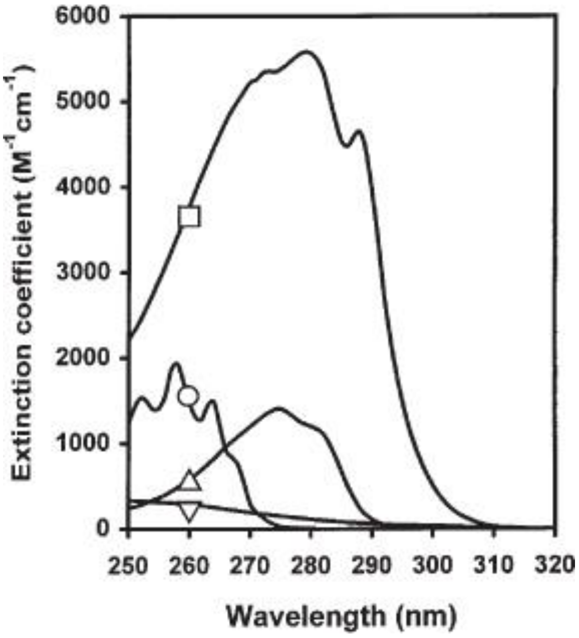

Figure 9: Absorption spectra of tryptophan (□), tyrosine (Δ), phenylalanine (○; spectrum multiplied by 10), and cystine (∇) recorded in 10 mM phosphate buffer (pH 7.0). Reproduced from (55).

Especially photoactive proteins have chromophores, like retinal, that absorb visible light. The ratio of protein (λ_{max}=280 nm) and retinal (ground state ChR2-WT= λ_{max}=470 nm) absorbance serves as measure for the purity of a ChR2 protein sample. The higher the ratio the smaller is the fraction of retinal reconstituted ChR2 protein in the total protein. Consequently the ratio decreases with increasing purity.

The extinction coefficient, ε, (band intensity) as well as the energy of the electronic transition (band position) of retinal are tuned by the protein surrounding (in particular the electrostatic environment). Therefore time-resolved measurements of the UV/Vis absorption of retinal are used to trace the reaction kinetics of ChR2. In flash photolysis measurements ChR2 is excited by a 10 ns laser pulse and the thermal relaxation via several quasi-stable intermediates is observed at a certain wavelength. The experimental setup uses a monochromator for the probing light to separate certain wavelengths from a polychromatic light source. In flash photolysis experiments a second monochromator is used to separate the scattered excitation light from the probing light.

2.3.1.1.2 ***FTIR difference spectroscopy***

The infrared (IR) light spans the spectral region from ~0.8 µm to ~1000 µm. Electromagnetic radiation of that frequency excites transitions between rotational and vibrational states. In protein science typically the region from ~50 µm to ~2.5 µm (~200 cm^{-1} to ~4000 cm^{-1}), called mid infrared, is investigated. In order absorb light in the infrared spectral region, a molecule must possess vibrational modes that induce an oscillating dipole moment. Thus only vibrations with a change in dipole moment are excited in IR spectroscopy. This excludes the symmetrical stretching vibration mode of CO_2 or the stretching vibration of N_2.

Fourier transform Infrared (FTIR) spectrometer are most commonly used for data acquisition. Their measuring principle is different from the one used in a conventional UV/Vis setup, as described above. FTIR spectrometer use polychromatic measuring light in combination with an interferometer. A scheme of Michelson Interferometer is shown in Figure 10. Polychromatic IR light is emitted by a source (S). Half of it is reflected by the beam splitter (dashed line, BS) and travels the distance L to a static mirror (M1). The other half is transmitted to a moving mirror (M2), which center of movement is the distance L to the BS. During the measurements it is moved back and forth by the distance x. When both beam halves are recombined at BS they traveled the way $2L$ and $2(L+x)$, respectively. Thereafter recombined beam are passed through the sample chamber (not shown) before the intensity I is measured at the detector (D). The beam path difference x modulates the relative phase difference of the recombined beam halves. The plot of the light intensity versus x is called interferogram. By a Fourier transform the different light frequency components are resolved and can be plotted as a spectrum (intensity versus wavenumber).

A molecule with *N* atoms has 3*N* vibrational degrees of freedom. Accordingly large molecules like proteins have very complex spectra with many overlapping bands. For the investigation of protein function it is advantageous to record difference spectra, which reflect the spectral differences between two states. I_0 is recorded with dark-equilibrated ChR2-WT (ground state) and *I* after applying a certain illumination protocol (e.g. P_4^{480}). Using Equation 1 gives the difference spectrum exhibiting negative bands for ground state and positive bands for P_4^{480}.

The band positions of a vibration mode is determined to large extent by the bonding strength and mass of the bonding partners. Proteins have large absorption bands arising from vibrational modes of their backbone, namely the amide group. Highly sensitive to the secondary structure configuration and thus to the conformation is the amide I band. It arises mainly from the C=O stretching vibration with minor contributions of out of phase C-N stretching, the CCN deformation and N-H in plane bending. The absorption maximum is around 1650 cm^{-1}. The Conformational sensitivity is a consequence of the crucial involvement of C=O and N-H as hydrogen bond acceptor and donor in secondary structure. The out of phase combination of N-H bending and C-N stretching constitute for the main part the amide II mode at

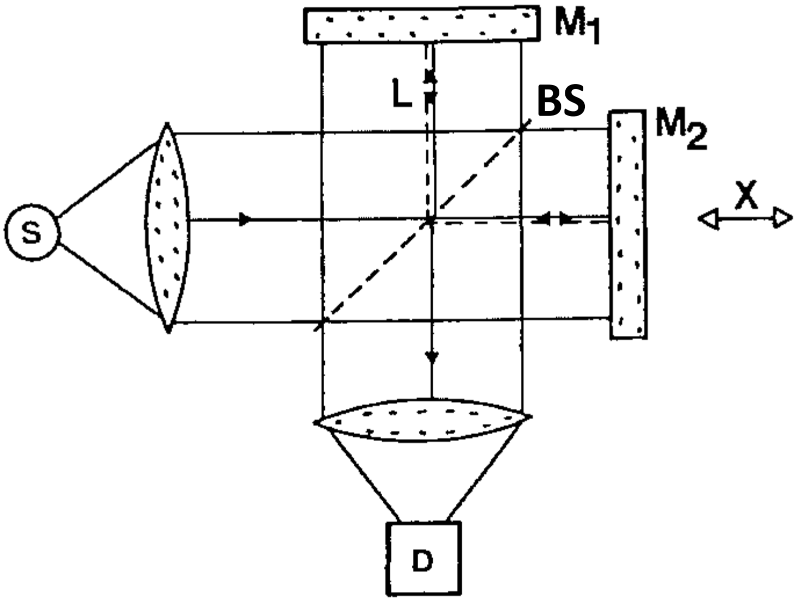

Figure 10: Scheme of a Michelson Interferometer. Explanation see text. Reproduced from (56).

~1550 cm^{-1}. To a minor degree also C-O in plane bending and the C-C/C-N stretching vibrations contribute (57).

Also the amino acid side chains give characteristic bands. Reference (57) gives an extensive overview. However, the position and intensity of certain sidechain groups within proteins varies a lot, since the protein environment modulates their electron density and polarization.

2.3.1.2 Resonance spectroscopy

2.3.1.2.1 *EPR spectroscopy*

In 1922 Otto Stern and Walther Gerlach performed an experiment shooting silver atoms through an inhomogeneous magnetic field. The atom beam split under influence of the magnetic field into two defined bands, thereby proving space quantization of the magnetic momentum of silver atoms (25, 26). Later on, the origin of this magnetic momentum was explained by an intrinsic angular momentum of the electron which is called spin.

Electron paramagnetic resonance (EPR) spectroscopy investigates transitions between the states of these electron spins. Since according to the Pauli principle, the electron spin cancels out for paired electrons, electron spin transitions can only be excited in atoms/molecules featuring an unpaired electron (i.e. paramagnetic materials). In biology, unpaired electrons occur usually in d-metal complexes or transiently in special organic cofactors, for instance in riboflavin derivatives. Therefore most biological matter without these cofactors is EPR silent. From the end of the 80s researchers started to introduce spin label to defined sites in proteins (site directed spin labeling). Continuous wave (CW) EPR was used to measure label mobility and water accessibility. Wayne Hubbell and coworkers used this to distinguish between an α-helical- and a loop-region (58) in bacteriorhodopsin (BR). The adaptation of pulsed EPR enabled researchers to measure spin-spin distances in a range of 1.5 to 5 nm (59) In combination with site directed spin labeling these techniques provide information on local structure with less restrictions concerning the protein size and homogeneity, when compared to NMR or X-ray crystallography. In this work CW and pulsed EPR have been used in order to characterize structural changes in ChR2.

The spin label

2,2,5,5-tetramethyl-pyrroline-1-oxyl methanethiosulfonate (MTSL or MTSSL, see Figure 11) is most commonly used for SDSL. The unpaired electron located mainly at the nitrogen atom is stabilized by the steric shielding of two methyl groups.

It binds highly specifically to thiol groups over a broad pH range. The small size and flexibility of the label helps to avoid unwanted effects on the activity of proteins. As a drawback of the flexible linker, MTSL can adopt different rotamers which can complicate the interpretation of spin-spin distance changes with reference to structural changes of the protein.

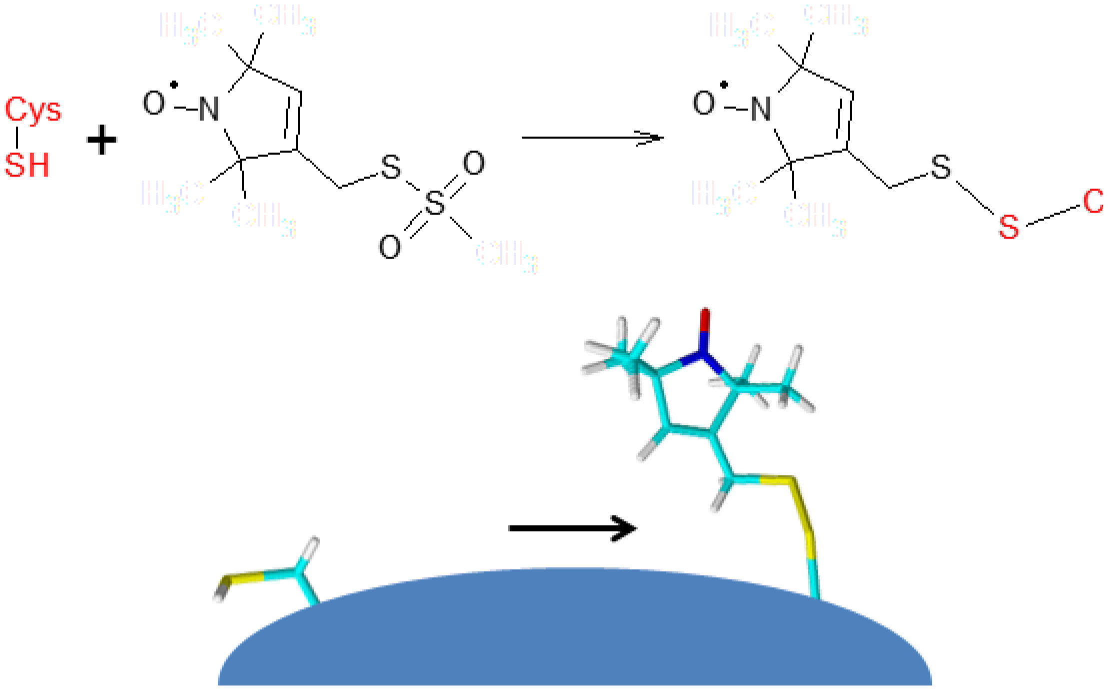

Figure 11: Spin labeling reaction of a cysteine with MTSL.

Theoretical background

The following sections will give a brief introduction to EPR (60), in order to understand the features of an MTSL spectrum and the methods used in this work (54,61).

Zeeman Effect

The orientation of the electron spin and its associated magnetic momentum are quantized. The total magnetic moment of an electron is a multiple of the Bohr magneton, μ_B. For an electron with its spin S = ½, there are two spin states, characterized by the spin quantum numbers $m_s = +1/2$ (also called α-spins) and $m_s = -1/2$ (β-spins), which are degenerate unless an external magnetic field is applied. This lifting of the degeneracy in a magnetic field is called the Zeeman Effect. The resulting splitting of the energy levels of both spin states is given by the electron Zeeman Hamiltonian $\widehat{H}_Z$ (see Figure 12).

$$\widehat{H}_Z = -g\mu_B\hat{S}_z B_0 \tag{2}$$

with the strength of the external magnetic field B_0 and the g-factor characterizing the orientation dependent proportionality between $\hat{S}$ and B_0. One selection rules for an EPR transitions is $\Delta m_S = \pm 1$. Thus the energy difference between both spin states ΔE is

$$\Delta E = h\nu = g\mu_B B_0 \tag{3}$$

, which is also the resonance condition, when $\Delta E = h\nu$ is inserted.

Hyperfine interaction

In formulas (2) and (3) we neglected the influence of neighboring spins on the magnetic field. Having a closer look, the local magnetic field at the site of the unpaired electron is influenced by surrounding magnetic moments, the hyperfine field. A magnetic moment arises from the nuclear spin of the nucleus/nuclei close to the electron. In case of the spin label used for SDSL the radical is in a π-hybridized molecular orbital that is composed of the overlapping p_z-orbital of the N and O atom of the nitroxide radical. While ^{16}O and the nearby ^{12}C have the spin quantum number

I=0, Nitrogen has I=1 and therefore $2I + 1$ possible spin orientations determined by the magnetic spin quantum numbers m_I=+1, 0, -1. So considering Zeeman as well as hyperfine splitting, which are typically the effects dominating the EPR spectra, we get the following Hamiltonian:

$$\widehat{H}_{Z+HF} = -g\mu_B\hat{S}_z B_0 + a\hat{I}_z\hat{S}_z \tag{4}$$

with *a* the hyperfine coupling constant and $\hat{I}_z$ the spin operator of the nucleus. Taking the nucleus' three spin states into account, the hyperfine interaction causes the splitting into three transitions for an electron coupling to a nitrogen nucleus as shown in Figure 12. The splitting due to naturally occurring ^{13}C or the even more distant nuclei is too small to be resolved in a standard EPR spectrum. The hyperfine interaction arises from two phenomena: The isotropic Fermi contact interaction and the anisotropic dipole-dipole interaction. The Fermi contact interaction is a magnetic interaction due to the fact that the electron has a nonzero probability of being at the

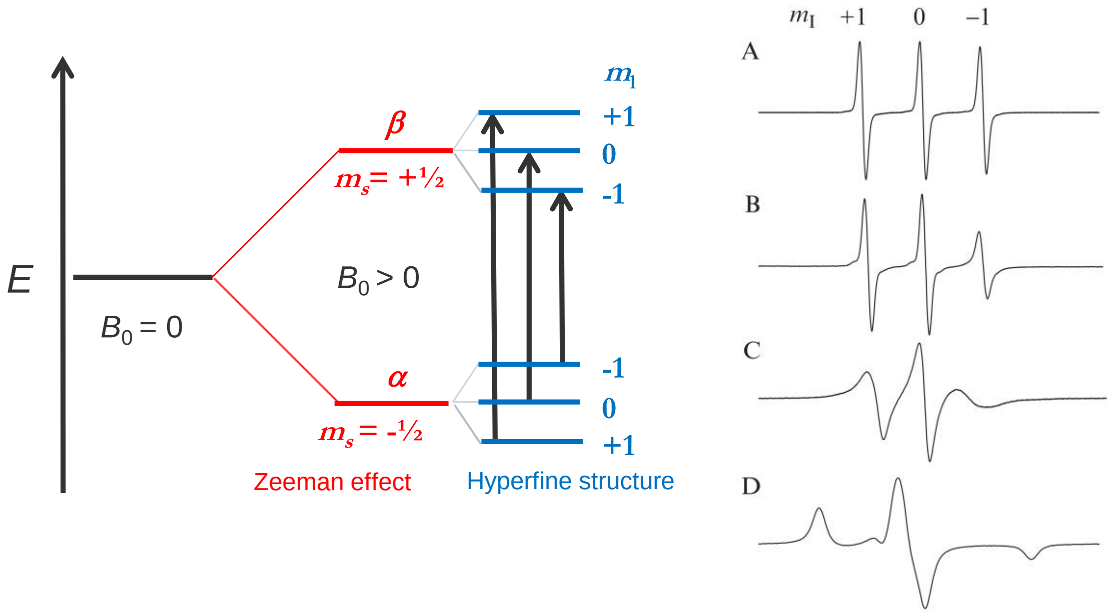

Figure 12: Left: Energy diagram for the Zeeman effect and hyperfine structure for an atom with a nucleus I=1, like nitrogen. The splitting results in three transitions with different ΔE. Note: For clarity the splitting by the hyperfine interaction is strongly exaggerated compared to the Zeeman effect at typical field strength used in EPR. Right: MTSL spectra showing three resonance lines according to the hyperfine interaction with the N nucleus. The spectra exhibiting the effect of different label mobility from the free moving MTSL in A to frozen solution in D and intermediate mobility in B/C. The figure is reproduced from (62).

coordinate of the nucleus. The dipole-dipole interaction can be treated as the interaction between point dipoles and depends on the geometry of the orbital the electron is located in (e.g. the average interaction is zero for the spherical s-orbitals). In the X-band the g-anisotropy is very small compared to the anisotropic part of the hyperfine interaction. Thus mainly the latter gives rise to sensitivity towards a rotational mobility of the label, as Figure 12 shows on the right side. At X-band frequencies (9-10 GHz) label with rotational correlation times τ_C smaller than ~0.1 ns (fast motional limit) show an isotropic splitting (Figure 12, right, A), as the anisotropic dipolar part of the coupling is averaged out. Slower motion leads to progressive line broadening (Figure 12, right, B-C) until at ~100 ns the slow motion limit is reached (Figure 12, right, D).

Interactions with other electron spins

Similar to the hyperfine interaction discussed above, an electron spin also couples also to another electron spin. Analogous to the isotropic Fermi interaction between an unpaired electron and a nucleus, for two unpaired electrons with significantly overlapping orbitals the Heisenberg exchange interaction has to be taken into account. The exchange interaction can be assumed in the context of protein to decay exponentially and can be quantified from the line broadening in the spectrum for distances up to ~1 nm. For spin-spin distances >1.5 nm it usually becomes insignificantly small compared to the dipolar coupling and can be neglected.

In this work, due to the large spin-spin distances that were investigated, absorption line splitting because of nearby electrons can be solely attributed to dipolar coupling. The energy of a system with two electron spins A and B can be described by the dipolar coupling Hamiltonian $\hat{H}_{ee}$.

$$\hat{H}_{ee} = \hat{S}_A D_{ee} \hat{S}_B = \frac{\mu_0}{2\pi} g_A g_B \mu_B^2 \left(\frac{\hat{S}_A \hat{S}_B}{r^3} - \frac{3(\hat{S}_A r)(\hat{S}_B r)}{r^5}\right) \tag{5}$$

where $\hat{S}_A$ and $\hat{S}_B$ are the electron spin operators and D_{ee} the dipolar coupling tensor. We can assume that the dipolar coupling is small compared to the Zeeman splitting (high field approximation) and that the g matrices are only weakly anisotropic. Thus the two spins are parallel and the expression above can be simplified.

$$\hat{H}_{ee} = D_{dip}(1 - 3cos^2\theta)\hat{S}_A\hat{S}_B \tag{6}$$

where θ is the angle between the magnetic field axis and the spin-spin vector (see Figure 13, left) and D_{dip} is the dipolar splitting constant,

$$D_{dip} = \frac{-\mu_0}{4\pi} g_A g_B \mu_B^2 \frac{1}{r^3} \tag{7}$$

with the isotropic g values of the two spins, g_A and g_B, and the distance between both spins r. D_{dip} can be experimentally determined, as described in the next section, and is used to determine r.

In case of a randomly distributed sample in frozen solution the superposition of signals from spins with random orientation θ leads to a band shape called a Pake pattern (Figure 13, right). The symmetrical shape arises from the two different possible B spin orientations (Figure 13, right: orange dotted line, points out one B spin orientation). The most probable orientation of the spin-spin vector is perpendicular to the field axis, therefore θ= 90° is most intense. From there the probability decreases towards the least probable orientation parallel to the magnetic field (θ= 0°).

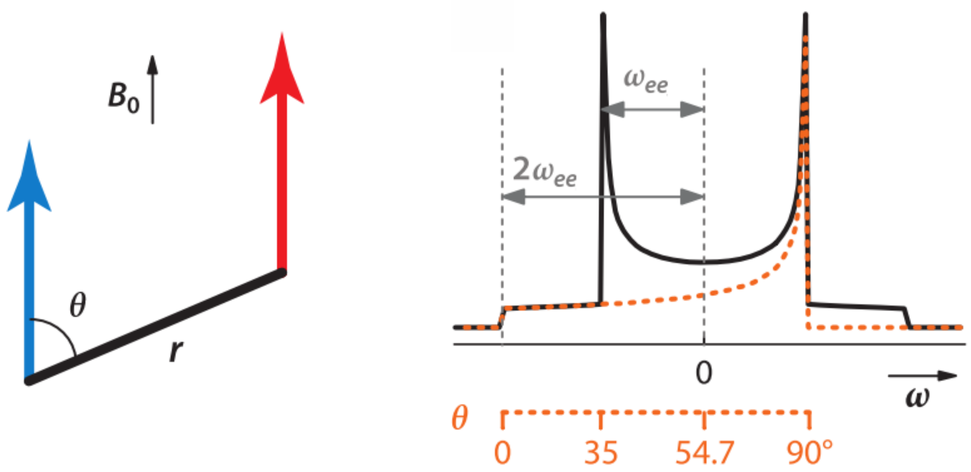

Figure 13: Left: Scheme of the magnetization vectors of spin A (blue) and B (red) both aligned to B_0. r is the spin spin distance and the angle θ characterizes the orientation of both spins with respect to each other. Right: The splitting of the resonance line due to dipolar coupling of the two spins gives the Pake pattern. Reproduced from (61).

Pulsed EPR spectroscopy

Since the effect of dipolar coupling is typically too small to be read out by the line width of an EPR spectrum, advanced pulsed EPR techniques that can extract the dipolar from other couplings need to be applied. Looking closely at an electron spin in an external magnetic field shows that the spin vector does not align parallel to the field axis but with some tilt. In analogy to a spinning top with a tilted rotation axis with respect to the gravitational field, the electron spin is precessing around the field axis, usually defined as the z axis of the coordinate frame, (see Figure 14) with a specific frequency, the Larmor frequency ν_L which is proportional to the local magnetic field and the gyromagnetic ratio of the electron γ_e.

$$\nu_L = \frac{|\gamma_e B_0|}{2\pi} \tag{8}$$

The electron spin population in a sample can be pictured to precess, each spin with its respective ν_L, on two cones according to the α- and β-orientation. The energy difference between both spin states is at the typical measuring conditions (X-band) about 6×10^{-24} J, whereas the available thermal energy ($k_B T 4\times 10^{-21}$ J) is three orders of magnitude higher. The thermal energy allows transitions between both orientations. The β-orientation is energetically more favorable and therefore a net magnetization arises from the very small excess of spins in the β-orientation. After

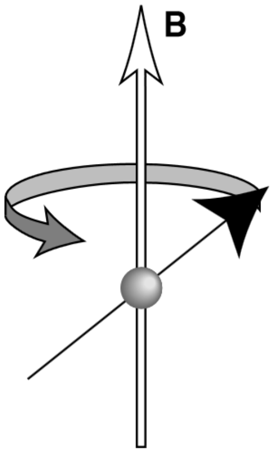

Figure 14: Schematic depiction of an electron spin vector (black arrow) precessing (grey arrow) around the magnetic field *B* (white arrow).

changes of the external magnetic field the spin population will relax to the new thermal equilibrium with the longitudinal relaxation time constant T_1.

By applying an additional magnetic field oscillating with the Larmor frequency of the electrons, the magnetization vector can be tilted from the z axis. In practical terms, as the Larmor frequency is in the GHz range, the oscillating magnetic field is achieved by irradiation with microwaves. The pulse duration and amplitude determines the tilt angle of the magnetization. A pulse tilting the magnetization vector into the xy-plane is called 90°- or $\pi/2$-pulse. While a pulse turning the magnetization beyond the xy-plane, so that it aligns again with the z-axis but with inverse directionality, is called 180°- or π-pulse. After the pulse, the magnetization vector is again precessing in the Larmor frequency around the z-axis. The tilted magnetization vector has a portion in the xy-plane (transverse magnetization). Tracking the intensity of this transverse magnetization at a fixed point in the xy-plane will give a signal oscillating with the Larmor frequency. As a real pulse inverts spins with different Larmor frequencies due to its spectral width, the precessing spins will get out of phase. The observed signal is accordingly a dampened oscillation referred to as the free induction decay (FID). The Fourier transform of the FID will give the Larmor frequencies of the spins and thus the EPR spectrum. In practical terms, this approach is seldom possible, the spectrometer's dead-time after a microwave pulse makes recording the FID impossible. The FID is thus typically observed after applying a pulse sequence called Hahn-Echo. The sequence consists of one $\pi/2$-pulse, which focuses the magnetization in the xy-plane. The magnetization dephases for the duration of τ_1 , is turned by 180° with a p-pulse, refocuses and dephases again, yielding two back-to-back FIDs, the electron spin echo. The decay of magnetization coinciding with the last step of dephasing is measured. The Fourier transform of the FID will give the Larmor frequencies of the spins and thus the EPR spectrum. As EPR spectra are usually too broad to be excited by a single pulse, the spectrum is typically obtained by integration of the echo at different field positions instead of Fourier transform.

4-pulse electron double resonance

The pulse sequence of a 4-pulse electron double resonance (4pELDOR) experiment is shown in Figure 15. The 4pELDOR experiment is conducted with two different microwave pulse frequencies exciting two different populations of spins (blue: probed spins; red: pumped (inverted) spins). If we ignore the second pulse frequency (red), on the observer spin frequency (blue) a Hahn Echo is performed, thereafter the spins are allowed for τ_2 to dephase and another π pulse is applied, leading to another echo after τ_2. This pulse sequence gives two echos with different phase. The second echo is decreased by all kinds of line broadening effects.

If we apply at another frequency a π-pulse inverting the other population of spins, the Larmor frequency of the observer spin population will be altered according to equation (8). Depending on *t* the dephasing and rephase during τ_2 is not symmetrical anymore and the second echo acquires a phase shift, compared to the sequence without the second frequency pulse. As the spin magnetization is detected along the orientation of the echo without the second frequency pulse, this results in a t dependent modulation of the echo amplitude in the 4pELDOR. The frequency of this modulation is solely dependent on the dipolar coupling between the electron spins. To get from the dipolar coupling in the time domain to the frequency domain, Fourier

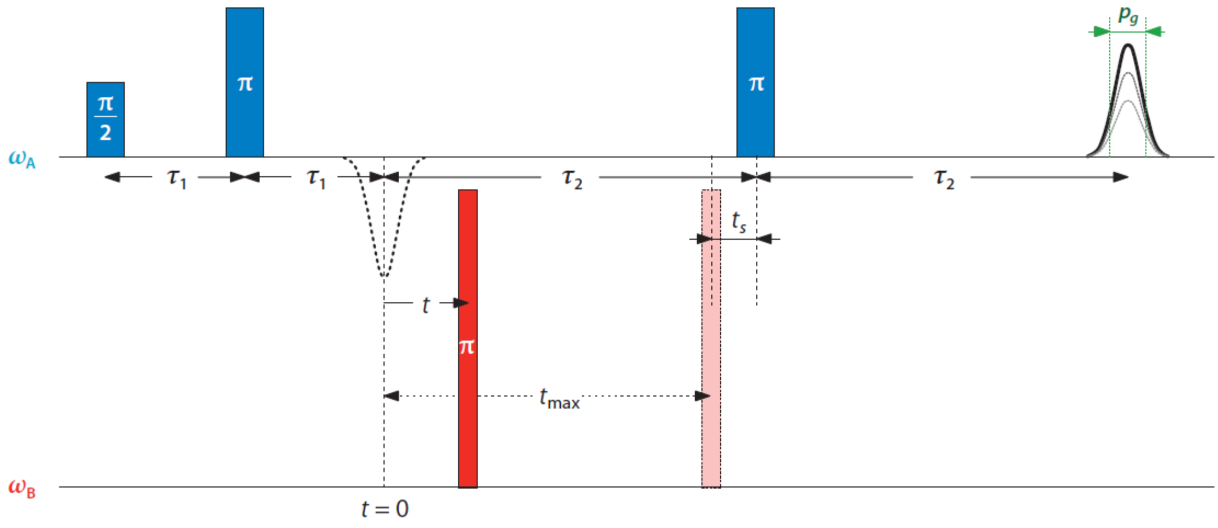

Figure 15: 4-pulse PELDOR sequence: Explanation see text. Reproduced from (61).

Transform is used. The yielded dipolar coupling frequency is according to equation (6) proportional to the third power of the spin-spin distance.

As depicted in Figure 16, the resulting distance distribution contains the targeted intra-molecular distances, but also inter-molecular distances between proteins in solution in solution. Different background models are applied to correct for these long range dipolar couplings (63).

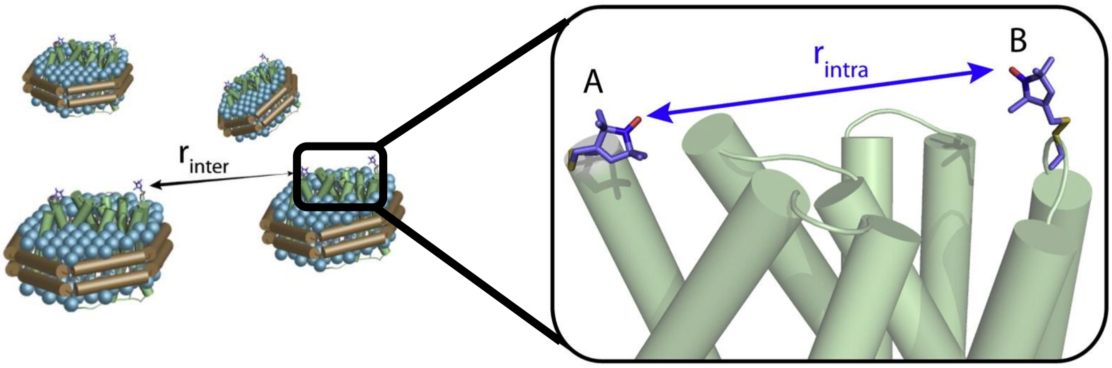

Figure 16: Schematic depiction of inter- and intra-molecular spin-spin distances. Reproduced from (36).

2.3.1.3 Spin labeling efficiency

First, the labeling efficiency for wild type ChR2 was determined to probe the accessibility of cysteines for MTSL label. Continuous wave EPR spectra of labeled ChR2 at room temperature were recorded. A spectrum of MTSL label in solution was normalized to the peak of free label in the ChR2 solution spectrum. The difference of the ChR2 solution spectrum and the normalized MTSL spectrum is essentially the spectrum of spin label bound to ChR2. The second integral of this spectrum related to the second integral of a MTSL solution with known concentration yields the concentration of bound MTSL in the sample.

2.3.2 Electrophysiological measurements

The electrophysiological recordings were done by Franziska Schneider in the research group of Peter Hegemann (Humboldt University, Berlin). For a detailed description of the method and the measuring setup please refer to (64) and (65). Franziska Schneider cloned the ChR2-C79/C128T and ChR2-C79/C128T/C208 gene constructs (not humanized sequence) into the pmCherry-N1 vector and supplied the ChR2-C128T construct (humanized sequence) in the same vector. After transfection the Human Embryonic Kidney 293 (HEK) cells were cultivated for 2-3 days before the measurements were conducted. With a micropipette a conductive connection is established to the interior of the HEK cell. In voltage-clamp mode the voltage between the interior of the cell versus an electrode in the external solution of the cell is clamped to a given value while the current needed to maintain this value is recorded. The current before illumination of the cell is set to 0. The difference to the initial conductance after light excitation of the ChR2 in the plasma membrane of the HEK cells is observed. In ms-time resolution the opening, desensitization and closing of the channel is observed.

The measurements were conducted at pH 7.2 using the buffers in Table 2.

Table 2: Buffers used for the whole cell patch clamp measurements. The micropipette was filled with "internal" buffer in a great excess to the HEK cell volume. Thus the internal buffer can be assumed to be the liquid intracellular of the cell membrane, while the "external" buffer was surrounding immersed the cells. The pH of both buffers was set to 7.2.

	component (mM)						
buffer	Hepes	EGTA	NaCl	KCl	CaCl	$CsCl_2$	$MgCl_2$
internal	10	10	110	1	1	2	2
external	10	-	140	1	1	2	2

3 Results

3.1 Genetic engineering: Designing cysteine-reduced variants

In order to label side specifically the label accessible cysteines have to be removed. ChR2-WT contains 9 cysteines. To estimate the amount of label accessible cysteines the first spin labeling experiments were conducted with ChR2-WT. ChR2-WT was labeled for 2 h and overnight at pH 6.0 and pH 7.4, respectively. The results are shown in Table 3.

Table 3: ChR2-WT spin labeling efficiency (label/ChR2) using MTSL; "±" standard deviation determined by error propagation using the errors of ChR2 and MTSL concentration measurements; labeling conditions: 25°C, 20 fold excess MTSL to cysteines.

Incubation	**pH 6.0**	**pH 7.4**
2 h	1.6 ± 0.3	2.6 ± 0.5
overnight	3.9 ± 1.0	5.7 ± 1.3

In the first 2 h of incubation around 2 cysteines per ChR2 and after incubation overnight 4-6 cysteines were labeled. The labeling efficiency seems to be slightly dependent on the pH, yielding higher label stoichiometry at higher pH. Since the majority of cysteines seems to be label accessible, a cysteine free ChR2 gene (see Table 4), in which all cysteines are replaced by alanines, was tested for expression (as described in 2.2.1.4, p. 22ff). After the purification procedure, UV/Vis absorption spectroscopy and SDS-gel electrophoresis indicated that the cysteine free variant seems not to express. Therefore, in order to identify essential cysteines several variants with different number of cysteines were tested for expression (C34A/C36A/C79A/C87A to C79/C208, Table 4) and analyzed by FTIR (Figure 18) as discussed later in this section. The most interesting variant is only featuring C79 and C208 (C79/C208, Table 1) as both residues are, according to the chimera structure, at the cytosolic side of helix B and F (Figure 17). EPR studies on bacteriorhodopsin and sensory rhodopsin II revealed a movement of helix F (66), therefore the distance between helix B and F is a promising labeling site to detect helix movements in analogy to other microbial rhodopsins.

Unfortunately ChR2-C79/C208 did not express, as well as a variant in which C79, C128 and C208 remained (C79/C128/C208, Table 4). As it was known that C128T mutation in otherwise wild type sequence gives robust expression levels and enables to accumulate the open state (33,34), a variant was generated (C79/C128T/C208, Table 4) by substituting C128 by a threonine while retaining C79 and C208. This gave a variant which showed about 5 times higher expression yields than the wild type. It was previously (31,33) described that the substitution of C128 for a threonine slows down channel closing by more than one order of magnitude and thereby enables to accumulate an open state under continuous illumination.

In order to enable the investigation of other labeling sides the remaining cysteines C79 and C208 were substituted. Replacing additionally C208 by an alanine reduced

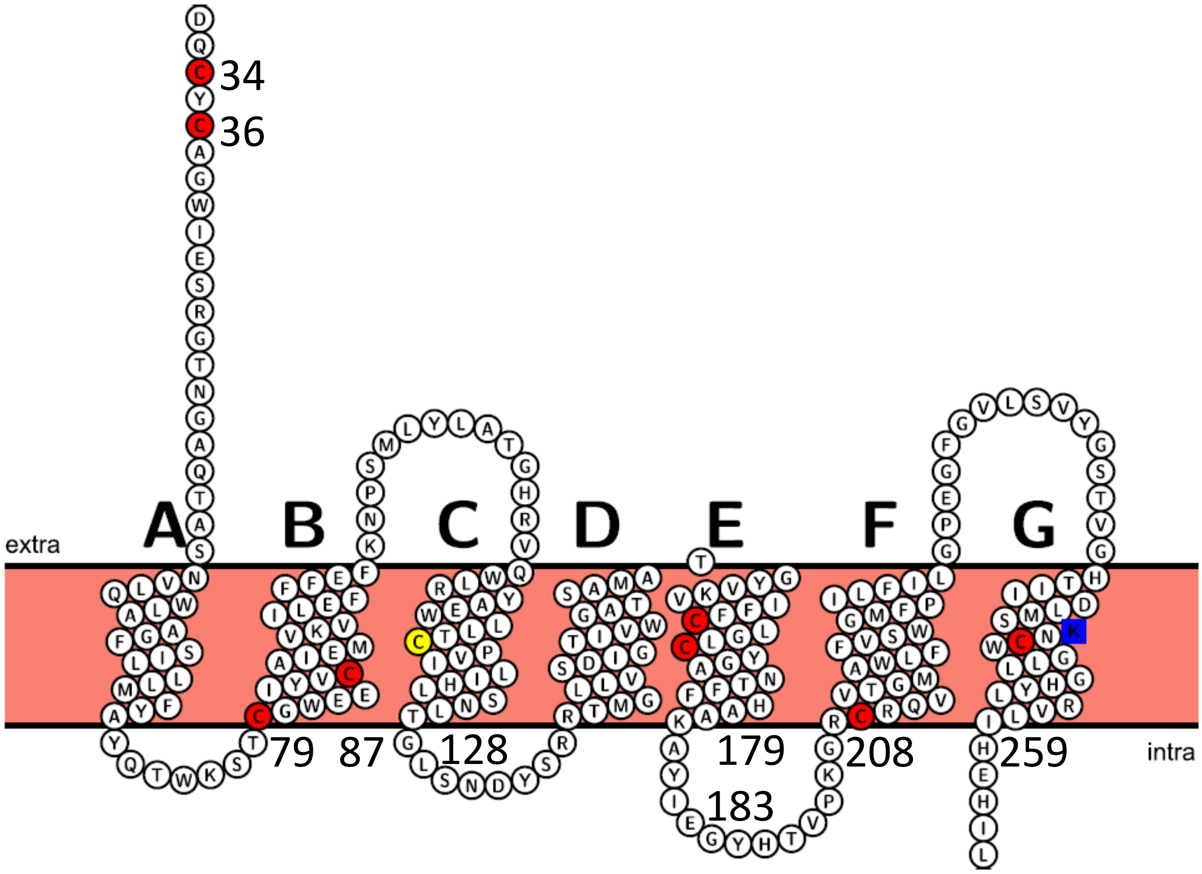

Figure 17: The cysteine positions of ChR2 indicated by red circles in the sequence of our ChR2-WT construct. C128 is marked with a yellow circle and K257, were the retinal is bound by a blue square. The scheme was plotted using Protter (67).

the expression to WT level. Replacing C79 by either serine or alanine abolished expression of functional ChR2.

For the assessment of the general functionality of the cysteine-reduced variants Figure 18A shows FTIR light-dark difference spectra in the region from 1800 to 1000 cm^{-1}. The spectra of ChR2-C128T, -C79/C128T and –C79/C128T/C208 are not shown, they will be discussed in the context of additional data in 3.3.2 (p. 51ff) and 3.4.3 (p. 70ff). The large amide-I difference bands, indicating a helix hydration, have been shown to persist from P_2^{390} to P_4^{480} (9,19). Therefore the experimentally easy accessible FTIR light-dark difference spectrum is in many cases a good measure for an influence of mutations in ChR2. The spectra are scaled to the all-trans retinal absorption band of ground state ChR2 at 1246 cm^{-1}. The difference spectra of ChR2-C34A/C36A/C259A and –C34A/C36A/C79A/C87A closely resemble the one of ChR2-WT, which first of all suggests that P_4^{480} is also in these variants the long lived intermediate, which dominates in the photostationary mixture. Both variants show the large amide I difference band at 1663(-)/1648(+) cm^{-1}, consequently also undergoing significant structural changes. While ChR2-WT and –C34A/C36A/C259A are essentially identical, ChR2-C34A/C36A/C79A/C87A shows altered intensity for the ethylenic stretch vibration of all-trans retinal in ground state at 1552(-) cm^{-1}. Also a band at 1538(-) cm^{-1} varies in intensity between the variants but have not been assigned yet. Additionally in the region between 1000 and 1150 cm^{-1} are some positive bands increased in intensity compared to ChR2-WT (like 1139, 1089 and 1066 cm^{-1}). In this region C-O and C-C stretching vibrations and different hydrogen-in-plane and hydrogen-out-of-plane vibration modes of retinal, tryptophan and histidine are observed (57,68). In consequence the retinal environment of ChR2-C34A/C36A/C79A/C87A in ground state and most likely in P_4^{480} is affected. Figure 18B displays the region characteristic for S-H stretch vibrations. Therefore thiol vibrations of cysteines can be observed. The light-dark difference spectra of ChR2-C128T and –C79/C128T/C208 are shown as well. Please note that the spectra of these two variants are dominated by P_3^{520} and consequently only negative bands originating from ground state are directly comparable. In ChR2-C34A/C36A/C79A/C87A (Figure

18B, orange trace) the band at 2557 cm^{-1} seems to disappear. Due to the poor signal to noise ratio it is not entirely clear if the band disappears or is smaller in intensity. Since C34 and C36 are forming of inter-monomer disulfide bonds, respectively, they cannot be involved in the S-H difference signals. Judged by the C1C2 crystal structure C79 is exposed to the solvent. The extinction coefficient of cysteines in a polar environment is very low (69). ChR2-C79/C128T/C208 (Figure 18B, violet trace) does not show any difference signals, which is in line with the solvent accessibility of C79. Therefore C87 is the most likely candidate constituting most of the intensity of the positive band at 2557 cm^{-1} in ChR2-WT. C87 is located in the middle of the transmembrane region of helix B close to the Schiff base. The appearance or increase in intensity of this band could be explained by a protonation of a C87 deprotonated in ground state or by an increase of the extinction coefficient of the thiol group (e.g. by dehydration). In ChR2-C34A/C36A/C259A (Figure 18B, red trace) the negative band at 2568 cm^{-1} is clearly reduced. The reduced intensity might also explain the apparent shift of the band at 2557 cm^{-1}. C259 is located in the middle of the transmembrane region of helix G, facing outward the protein on the opposite site where lysine 257 binds retinal via the Schiff base. Since C259 is facing outward the protein the environment might be rather nonpolar, helix G is upon illumination moving inward, in consequence C259 might get more exposed to hydrophilic residues. Such a scenario would explain the loss of absorbance intensity.

In conclusion C87 and C259 seem to give difference bands. For the unambiguous assignment it would be necessary to engineer two variants featuring solely C87A and C259A, respectively. If the assignment is verified these residues would be ideal candidates to report on helix B and G dynamics. For the assignment of C128 an illumination protocol for ChR2-C128T accumulating P_4^{480} to get the comparison to the other variants would be valuable.

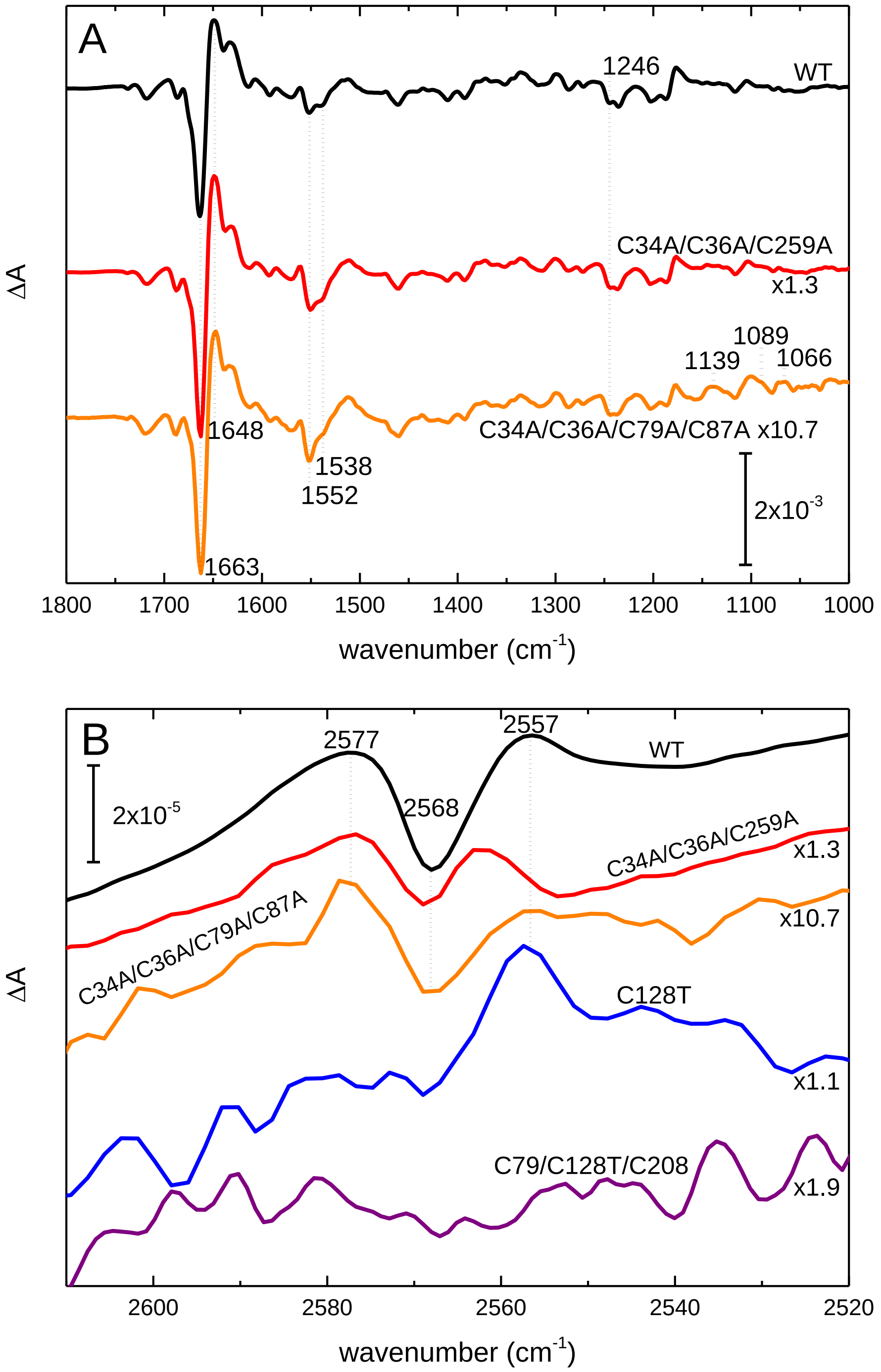

Figure 18: Light-induced FTIR difference spectra of several cysteine variants in comparison to ChR2-WT. The spectra were recorded under photostationary conditions (ChR2-WT, -C34A/C36A/C259A and -C34A/C36A/C79A/C87A at 25°C, pH 7.4, 456 nm illumination; ChR2-C128T and –C79/C128T/C208 at 5°C, pH 6.0, 420 nm illumination) and scaled to the all-trans retinal band at 1246 cm^{-1}.

Table 4: Cysteine mutants tested for expression: left coulmn (AA#) gives the amino acid numbering for the cysteines in the ChR2 sequence. Each row reflects a mutant tested for expression. The DNA constructs provided by R. Schlesinger are underlined. The right column indicates expression yields: A “-“ no expression, numbers give the mg of ChR2 per L of cell culture. The “+” for the yield of ChR2-C79/C128S/C208 refers to the intense red color of a small scale expression, that was not quantified by purification.

AA#	34	36	79	87	128	179	183	208	259	Yield
WT	C	C	C	C	C	C	C	C	C	~0.3
C128T	C	C	C	C	T	C	C	C	C	~4.8
C34A/C36A/C79A/C87A	A	A	A	A	C	C	C	C	C	~0.1
C34A/C36A/C259A	A	A	C	C	C	C	C	C	A	0.2-0.6
C34A/C36A	A	A	C	C	C	C	C	C	C	0.4
C179A/C183A/C259A	C	C	C	C	C	A	A	C	A	-
C79/C208	A	A	C	A	A	A	A	C	A	-
C79/C128/C208	A	A	C	A	C	A	A	C	A	-
C79/C128T/C208	**A**	**A**	**C**	**A**	**T**	**A**	**A**	**C**	**A**	**~1.5**
C208	A	A	A	A	T	A	A	C	A	-
C79/C128T	**A**	**A**	**C**	**A**	**T**	**A**	**A**	**A**	**A**	**0.3**
C128T	A	A	A	A	T	A	A	A	A	~4.8
S79/C128T/C208	A	A	S	A	T	A	A	C	A	-
C79/C128S/C208	A	A	C	A	S	A	A	C	A	+
C128/C208	A	A	A	A	C	A	A	C	A	-
C79/C128	A	A	C	A	C	A	A	A	A	-
C128	A	A	A	A	C	A	A	A	A	-
cysless	A	A	A	A	A	A	A	A	A	-

3.2 Ion conductance of the cysteine-reduced variants

Electrophysiology gives a direct read-out of the channel function. The light dependent conductance of ChR2 can be directly observed and characterized in terms of kinetics and amplitude. The measurement was done with Human Embryonic Kidney 293 (HEK) cells in whole cell recording at voltage clamp mode. Typical traces are displayed in Figure 19. During the measurement of photocurrents the potential over the membrane is set to -60 mV. The flux of cations into the cell is measured as negative currents in this patch clamp setup. In the first ms after the onset of illumination the currents peaks down (τ_{on}, Figure 19 left, Table 5) to a transient current minimum (I_p, Figure 19), which means maximal influx of cations. T_{on} characterizes the opening of the channel. The cysteine-reduced variants C79/C128T and C79/C128T/C208 seem to open slightly faster compared to C128T. I_p quantifies the current amplitude. The amplitude of the recording depends, beside the conductance of the channel itself, also on the expression level and the size of the individual cell. Therefore, as I_{min} tends to have a high variability, a high sample number has to be collected in order to gain significant values. Figure 20 visualizes the

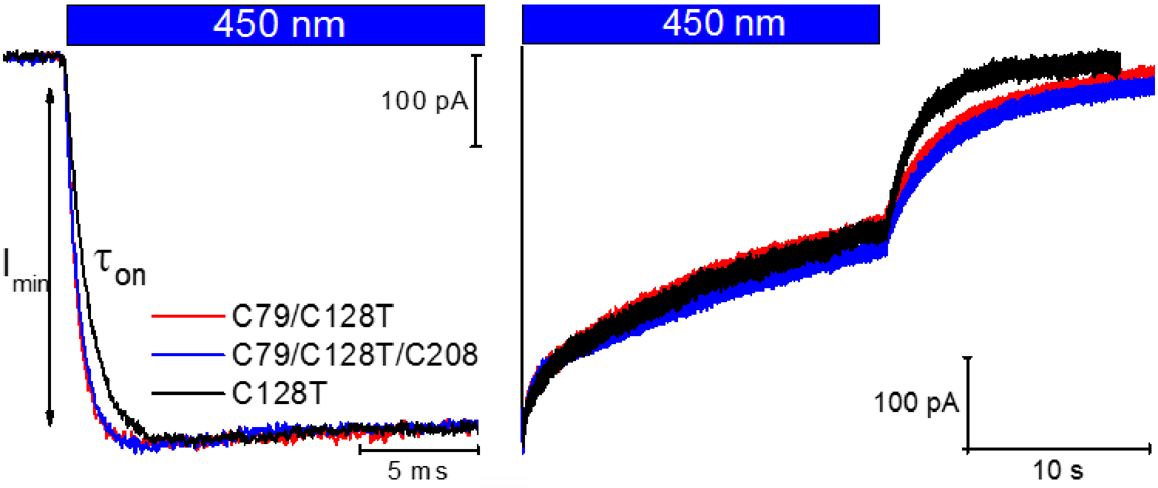

Figure 19: Photocurrents in HEK cells (whole cell recording). The left side shows on the short timescale the onset of the photocurrent (τ_{on}), while the right side shows on the long stimescale desensitization (τ_{des1}, τ_{des2}) and channel closing (τ_{off}). Holding potential -60 mV, illumination with 450 nm for 20 s, pH 7.2.

mean of I_p from individual cells and the according standard error. ChR2-C79/C128T/C208 shows about twice the conductance of ChR2-C128T.

I_p of ChR2-C79/C128T has because of the low sample number a large standard error, but the I_p seems to be rather in the range of ChR2-C79/C128T/C208 than of ChR2-C128T. Compared to ChR2-C128T both cysteine-reduced variants show higher

Table 5: Time constants of the photocurrents in HEK cells (whole cell recording). Time constants for current increase after illumination onset, τ_{on}, the biphasic current decrease during illumination (desensitization), τ_{des} and the decrease after stopping illumination, τ_{off}, as indicated in Figure 19. The data are means with standard error (±), the number of samples (individual cells) is given in brackets. Conditions as described in Figure 19.

ChR2-	τ_{on} (ms)	τ_{des1} (s)	τ_{des2} (s)	τ_{off} (s)
C79/C128T	3.83 ± 0.22 (3)	0.71 ± 0.11; 18%	11.6 ± 1,1; 82% (2)	3.70 (1)
C79/C128T/C208	3.90 ± 0.23 (12)	0.60 ± 0.10; 15%	22.2 ± 3,3; 85% (2)	3.40 ± 0.27 (2)
C128T	5.96 ± 0.29 (5)	0.95 ± 0.14; 19%	22.0 ± 0.9; 81% (2)	1.68 ± 0.08 (3)

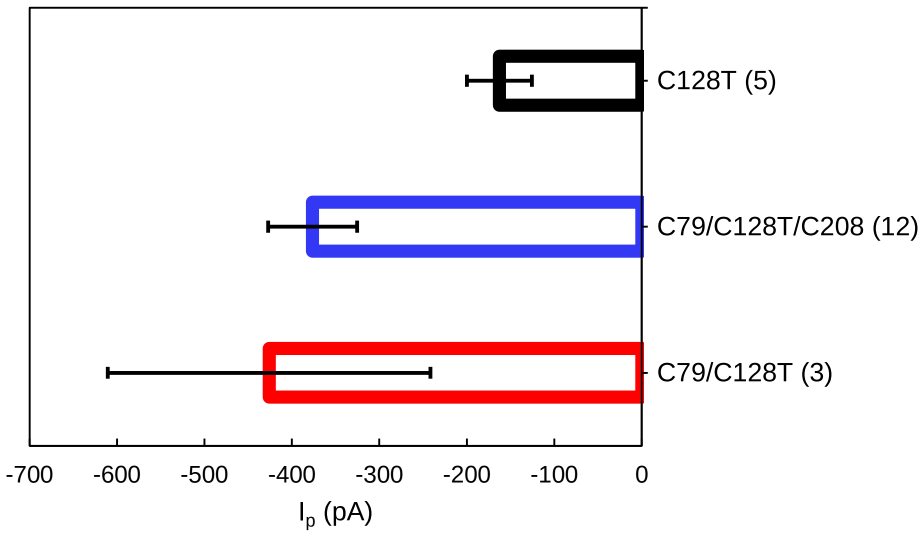

Figure 20: Amplitude (I_p, see Figure 19) of the photocurrents in HEK cells. The data are means with standard error (error bars), the number of samples (individual cells) is given in brackets. Conditions as described in Figure 19.

photocurrents. It remains unclear if the increased photocurrents are due to higher conductance of the channels or to higher expression in HEK cells. Since slightly different constructs were used (ChR2-C128T has a humanized codon set, ChR2-C79/C128T and ChR2-C79/C128T/C208) have the *C. reinhardtii* codon set), it could be attributed also to these differences apart of the differences in protein sequence.

After reaching I_p the current increases already during illumination. This process is called desensitization. The decay is biphasic for all three variants (τ_{des1} and τ_{des2}, Table 5). On the long timescale we experienced frequently baseline instabilities thus only a small subset of the measured traces could be used. Accordingly the standard error might be underestimated using such a small sample set. For all three variants the first phase has a similar time constant and has a smaller amplitude than the second phase (τ_{des1}, Table 5). The second phase seems to be about two times slower for the ChR2-C128T and ChR2-C79/C128T/C208 variants (~22 s) compared to ChR2-C79/C128T (~12 s).

After stopping illumination the channel closes and the current goes back to the initial level with the time constant τ_{off}. The τ_{off} is slightly slower for the ChR2-C79/C128T and ChR2-C79/C128T/C208 variants compared to ChR2-C128T.

3.3 Cysteine-reduced variants in detergent environment

The protein purification includes solubilization in DM (see 2.2.1.4, p. 22ff). The ChR2 samples used in this section are in a DM micelle environment (Figure 21).

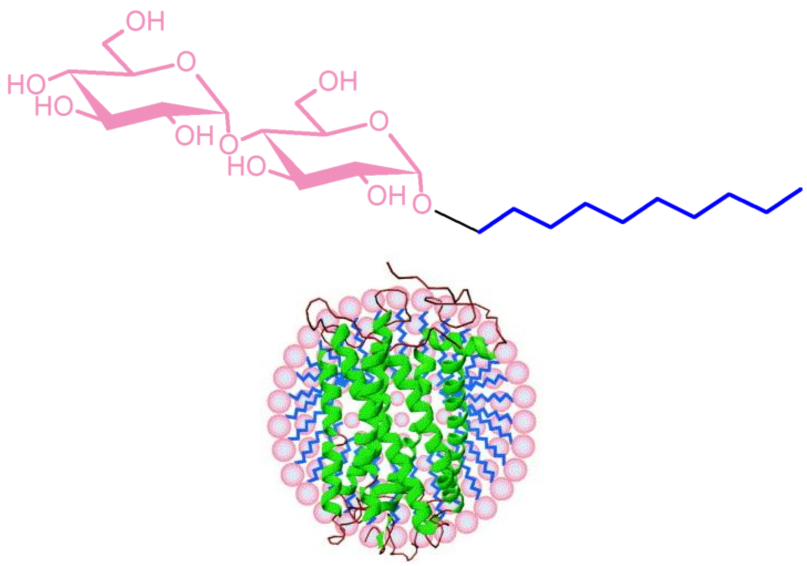

Figure 21: Left: Structure of Decyl-β-D-maltopyranoside (DM): The hydrophilic headgroup (pink), a glucose disaccharide (maltose), is bound via an ether linkage to the hydrophobic tail (blue) of a 10 carbon alkane chain; Right: Schematic representation of a membrane protein in a detergent micelle (reproduced from (70)). The hydrophobic parts of the protein are shielded by the hydrophobic detergent tails (blue), while the hydrophilic headgroups (pink) are at the water/micelle interface.

3.3.1 Photostability

First trials to characterize the photocycle of ChR2-C79/C128T/C208 showed that after continuous illumination a large fraction does not recover ground state but forms a photoproduct with an absorption maximum around 380 nm (Figure 22). Similar observation were made with ChR2-C79/C128T (71). The photoproduct at 380 nm does not recover ground state. The fraction of the 380 nm photoproduct after illumination and the recovery of ground state depends on the pH. At lower pH a larger fraction of ChR2 recovers the ground state. Therefore the following measurements were performed at pH 6.0.

During purification, sample preparation and measurement great care has to be spent to avoid illumination of the protein in order to yield high amounts of active ChR2.

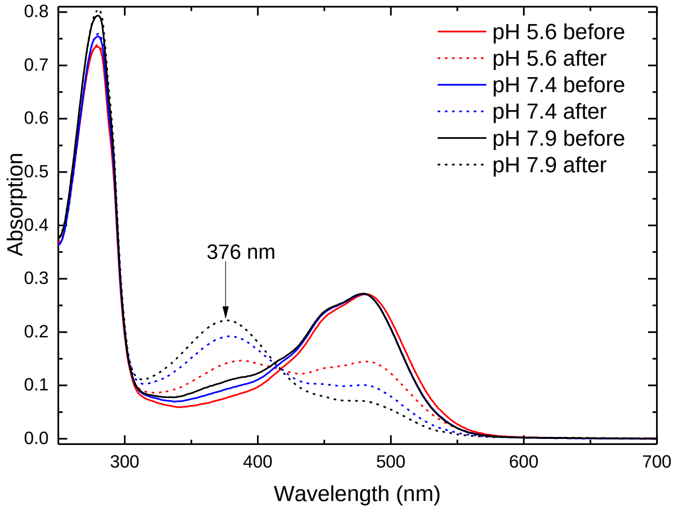

Figure 22: ChR2-C79/C128T/C208 UV/vis absorbance spectra at different pH, before and after 1 min (pH 7.4 and 7.9) and 2.5 min illumination (pH 5.6) with 456 nm at 27°C.

3.3.2 Accumulation of the open channel (P_3^{530})

Continues illumination leads in the ChR2-C128T variant to the accumulation of P_3^{530} (31,33), which was assigned to be a conductive state in WT ChR2 (31). In the following the time course of the spectral changes during and after illumination are studied. UV/Vis spectroscopy was used to study the kinetics of the relaxation process after P_3^{530} accumulation. Identical conditions were used as for the freeze quenching of the PELDOR samples (including 50% (V/V) glycerol). In the UV/Vis setup the spectral changes during illumination could not be resolved because of perturbing scattered excitation light. The FTIR difference spectra characterize the P_3^{530} intermediate of the cysteine-reduced variants and the influence of spin label as already published (72) (the FTIR part will be partly cited from this publication). The measurements were performed at 5°C, at pH 6.0 and at an excitation wavelength of 456 nm.

Figure 23A shows the ChR2-C79/C128T/C208 retinal UV/Vis band before (dotted line) and after illumination (solid lines). 12 s after illumination (Figure 23B) the main feature is a Gaussian shaped peak with a maximum at 490 nm, indicating the predominance of P_3^{530}. Figure 23C shows the time course of the absorbance differences at 390 nm (blue, P_2^{390}), 480 nm (black, Ground state) and 520 nm (red, P_3^{530}) with respect to the absorbance before illumination. All three kinetics are well described by two timeconstants as a global fit reveals (Table 6). The fine-structured P_2^{353} is clearly visible in the first spectra after stopping illumination (Figure 23 B, maxima at 356 and 377 nm). P_2^{353} was characterized ChR2-C128T at RT to have a τ~100 s (33). Consequently at 390 nm the decrease of absorption with τ_1~80 s can be most likely be assigned to the decay of P_2^{390}. 520 nm shows the monoexponential decay (τ_2~38 min) of P_3^{530}. At 480 nm the recovery of P_4^{480} or ground state from P_2^{390} (τ_1~80 s) and P_3^{530} (τ_2~38 min) is observed as two phases of absorption increase. P_4^{480} or ground state have in ChR2-C128T similar absorption patterns (31) and are in this measurement indistinguishable. At 390 nm the absorption increases with τ_2~38 min beyond the initial absorption level, indicating the formation of another photoproduct (as already observed in 3.3.1), which forms after the decay of P_3^{530} with absorption at 390 nm. Also 21 h after illumination the absorption is still increased at 390 nm, 520 nm and decreased at 480 nm. Therefore the photocycle seems to branch into an irreversible reaction leading to a photoproduct with absorption at 390 nm. Frequently for these “bleached” samples a baseline upshift was observed, which is typical for light scattered by larger aggregates. Thus indicating that the bleached protein might aggregate. About 87% of ground state absorption are here recovered at 5°C, which is far more compared to illumination at 27°C (Figure 22). The decay of P_3^{530} is slow enough (τ_2~38 min) to allow efficient freeze quenching.

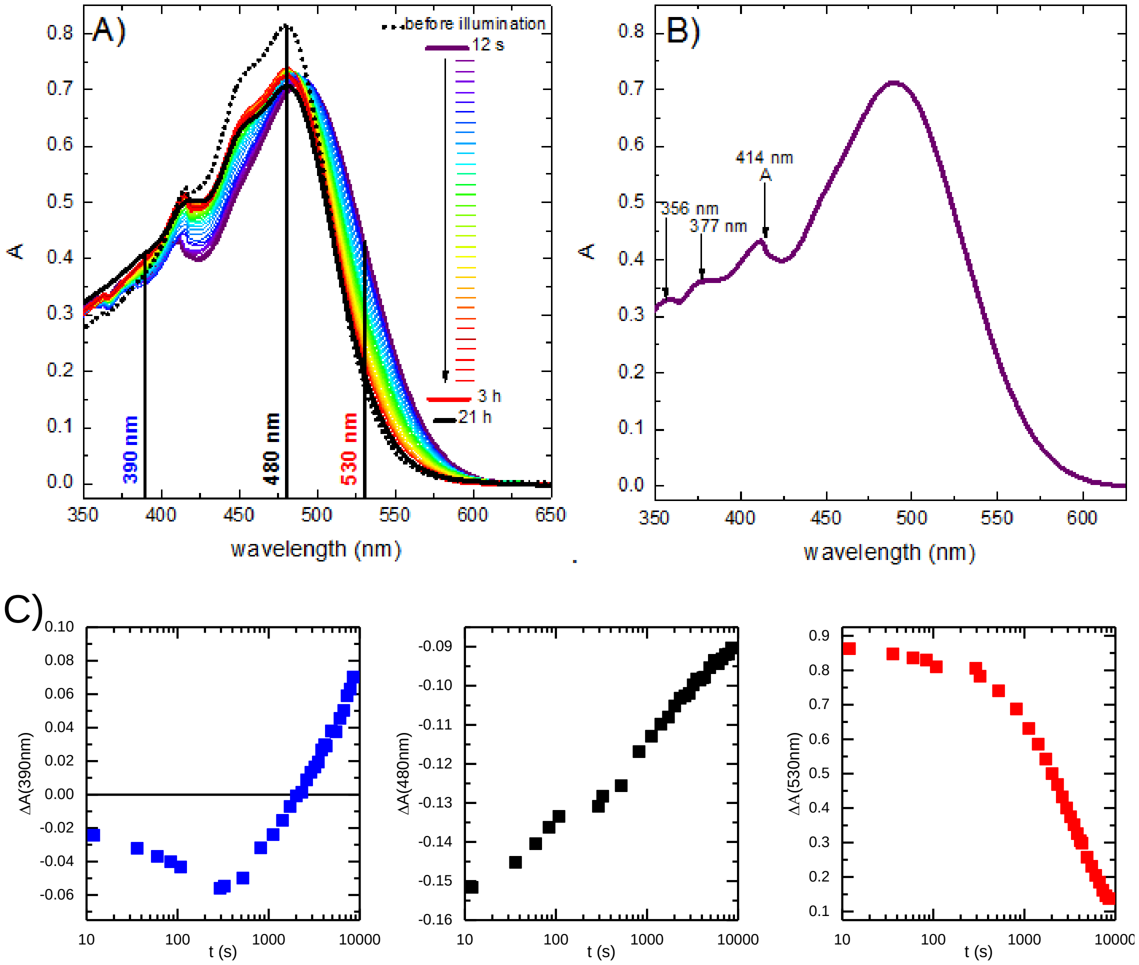

Figure 23: ChR2-C79/C128T/C208 UV/vis absorbance spectra: Relaxation after 3 min of illumination (end of illumination t=0 s); A: Spectra recorded before illumination (dotted line) and after 12 s to 21 h (solid lines, see legend for color coding) after illumination; B: Spectrum 12 s after illumination, P_3^{530} is predominant with minor contributions of P^{353} (λ_{max}=356 nm, 377 nm, 414 nm) and Ground state/P_4^{480} (shoulder at ~450 nm), an artifact from the spectrometer is marked with “A”; C: Time course of the absorbance changes after illumination at 390 nm (blue, P^{353} and P_2^{390}), 480 nm (black, P_4^{480} and Ground state) and 520 nm (red, P_3^{530}) with respect to the absorbance before illumination (ΔA before illumination=0); conditions: 5°C, pH 6.0, 50% (V/V) glycerol, illumination for 3 min at 456 nm excitation wavelength maximum.

Table 6: Time constants for the kinetics at 390 nm (P2390), 480 nm (Ground state) and 520 nm (P3530), as shown in Figure 23.

	τ_1	τ_2
390 nm	80 s; 25%	38 min; 75%
480 nm	80 s; 39%	38 min; 61%
520 nm		38 min

To check for the potential influence of the mutations and the attached spin label on the structural changes FTIR spectroscopy was performed. IR difference spectra of both variants (unlabeled and MTSL labeled) were recorded in the dark state and under photostationary conditions after 3 min illumination (456 nm) at 5°C. These conditions are identical to the EPR experiments presented below. Positive bands indicate vibrations in the intermediate state after illumination which are not present in the dark state whereas negative bands are due to vibrations in the dark state which are not observed in the intermediate state. The difference spectra of the ChR2-C79/C128T and ChR2-C79/C128T/C208 variants share the same prominent features as observed in the C128T variant (9) (Figure 24). Large amide I difference bands at 1662(-)/1648(+) cm^{-1} point to substantial alterations in the protein backbone conformation. The negative band at 1554 cm^{-1} was assigned to the C=C double bond stretching vibration of the retinal chromophore in the ground state that shifts to 1533 cm^{-1} in the accumulated P_3^{520} state. The fingerprint region shows a positive band at 1180 cm^{-1} that indicates the presence of 13-cis retinal with protonated Schiff base. These retinal vibrations suggest predominant accumulation of P_3^{520}. In conclusion, the strong similarity of the light-induced IR difference spectra of the ChR2-C79/C128T and ChR2-C79/C128T/C208 variants in comparison to the C128T variant suggests identical functionality. There is a small additional shoulder in the amide I region at 1637 cm^{-1} for the MTSL labeled variants. MTSL does not have any amide groups and the nitroxide group absorbs around 1435 cm^{-1} (73,74). 1637 cm^{-1} is a typical position for the amide I band of β-sheet structures. The band is observed in ChR2-C79/C128T/C208 and –C79/C128T in the same intensity. Thus the band might indicate different dynamics of the loop connecting helices A and B in the open state.

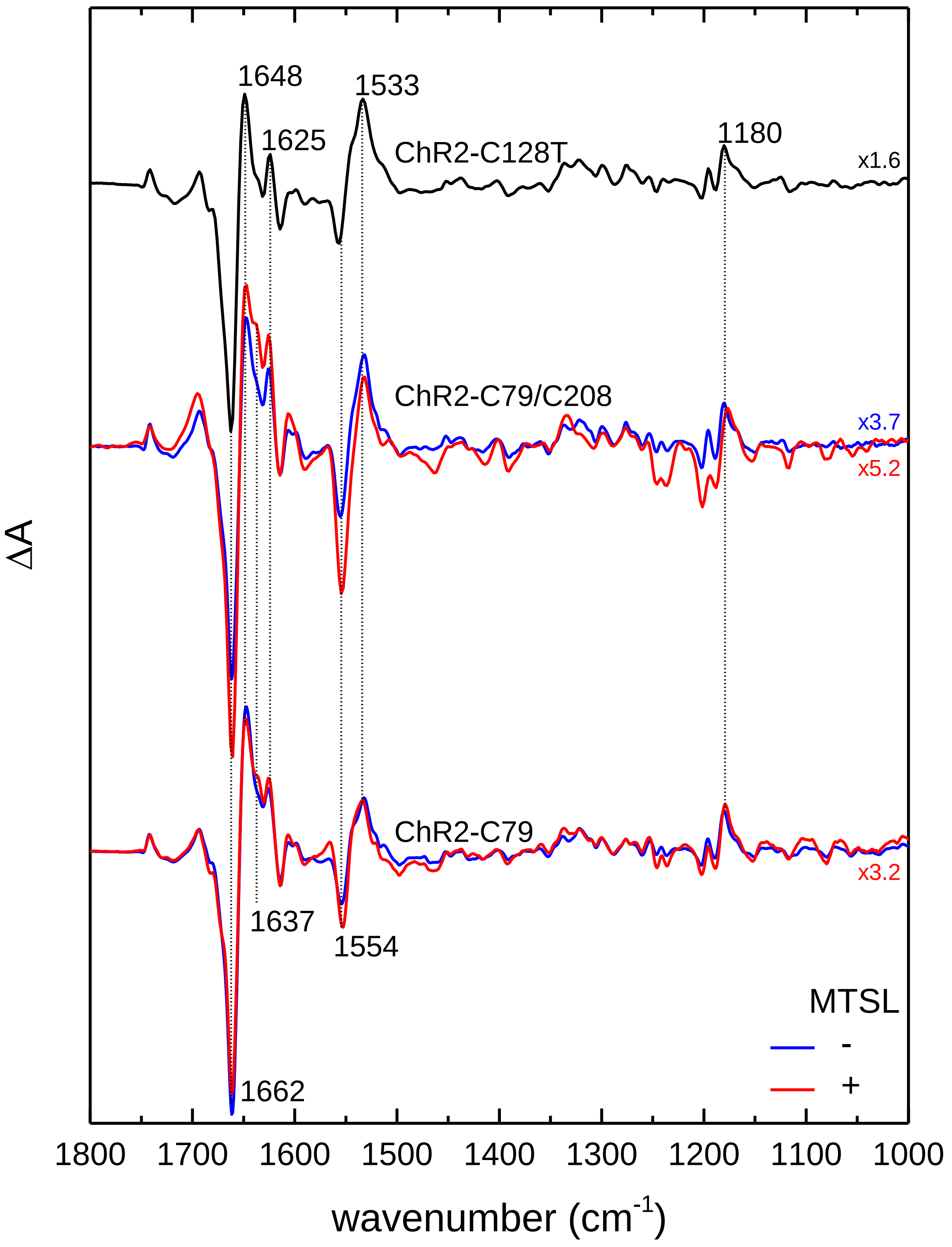

Figure 24: Light-induced FTIR difference spectra of ChR2 variants C128T (black), ChR2-C79/C128T/C208 and ChR2-C79/C128T unlabeled (blue) and MTSL labeled (red). The spectra were recorded under photostationary conditions (after 3 min illumination, 456 nm) at 278 K. The spectra are scaled to the 13-cis retinal band at 1180 cm^{-1}.

3.3.3 Helical movements

To track helical movements upon channel opening, spin-spin distances were measured of the dark-equilibrated protein (closed state) and the light-equilibrated protein (open state). The data presented in this section was measured by Christopher Engelhard (AG Bittl, FU Berlin) and published in (72). For these initial distance measurements a temperature of 5°C and 456 nm illumination for 3 min were chosen. As demonstrated in the previous section these conditions are well suited to trap the

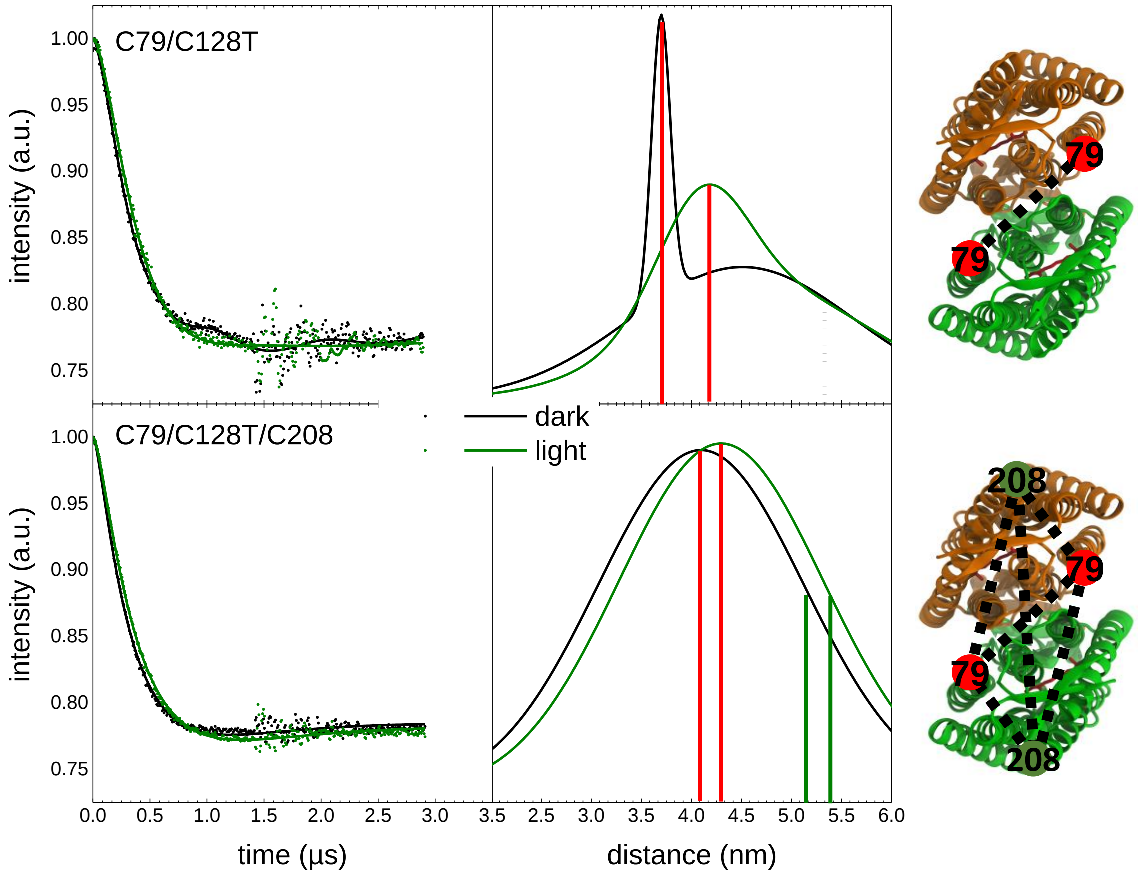

Figure 25: Background-corrected PELDOR measurements of spin labeled ChR2-C79/C128T (upper left quarter) and ChR2-C79/C128T/C208 (lower left quarter) in dark (black trace) and light state (green trace). Distance distributions of ChR2-C79/C128T (upper right quarter) and ChR2-C79/C128T/C208-labeled (lower right quarter

P_3^{530} state. For each of the light and dark time traces, a short low-noise time trace (1.5 µs) and a long time trace with higher noise (3 µs) were recorded and combined (Figure 25). Because of the high noise content of the long time trace a hamming window was applied to stabilize the fit of the distance distribution on the long timescale. The distance distributions derived by Tikhonov Regularization tend to over-interpret time traces with high noise level in terms of the distance distribution's fine structure. Therefore the background-corrected time traces were fitted with two Gaussians, each.

In the variants ChR2-C79/C128T and –C79/C128T/C208 the cysteine 34 and 36, which link ChR2-WT covalently are substituted by alanine. Consequently it was not clear at this point if the ChR2 variants still form a stable dimer. The distance distribution of the dark-equilibrated ChR2-C79/C128T in (Figure 25: upper half, black trace) shows a narrow maximum at 3.7 nm. The well-defined short distance indicates a large fraction of dimeric ChR2. Monomeric ChR2 would only contribute to the high distance background signal and no defined modulation. Consequently the dimer is also stable without bridging cysteines. The second Gaussian spreads over a broad distance region mainly at higher distance. The broad distribution could arise from a fraction of aggregated protein. In the open state the narrower peak shifts by 5 Å towards a larger distances (Figure 25: upper half, green trace). Thus the B-helices in the dimer are moving apart.

The ChR2-C79/C128T/C208 variant features at least 4 different spin-spin distances between the labels. Hence a broader distance distribution is expected. The distance distribution in the closed state indeed covers a broad range of distances and peaks at 3.9 nm (Figure 25: lower half, black trace). Therefore the distance distribution should be considered as the average of the distances between the four spin labels. Upon channel opening the distance distribution maximum again shifts by 5 Å (Figure 25: lower half, green trace), similar to the observed changes between the B-helices in the ChR2-C79/C128T variant. In contrast to the ChR2-C79 variant the distance distribution shows also at larger distances a shift to about 6 Å. This strongly indicates an outward movement of helix F.

3.4 *Cysteine-reduced variants in membrane environment*

3.4.1 Nanodisc Reconstitution

Nanodiscs are composed of lipids and genetically engineered membrane scaffold proteins (MSP). The scaffold protein used in this study (MSP1D1) originates from the human apolipoprotein AI (ApoA-I). ApoA-I is produced by the liver constituting a discoidal complex consisting of cholesterol and phospholipids, called high density lipoprotein particles (HDL). The discoidal HDL particles collect free cholesterol, adopt a heterogeneous spherical shape and transport the cholesterol back to the liver, thereby help to reduce fatty deposits in the arteries (anti-atherogenic function) (75). Nanodiscs were characterized by various biophysical techniques including atomic force microscopy (AFM) (52), small angle x-ray scattering (SAXS) (76) and solid state NMR (77). In summary they provide a picture of a circular, homogeneously sized complex, in which two alpha helical MSP molecules wrap around a membrane patch, as shown in Figure 26. The size of the MSP construct used in our studies (MSP1D1) is 9-10 nm (76,79).

Membrane proteins can be incorporated into nanodiscs, which offer a lipid environment (Figure 27) that is closer to native conditions. In contrast to other lipid environments used to study integral membrane proteins in biophysics (e.g.

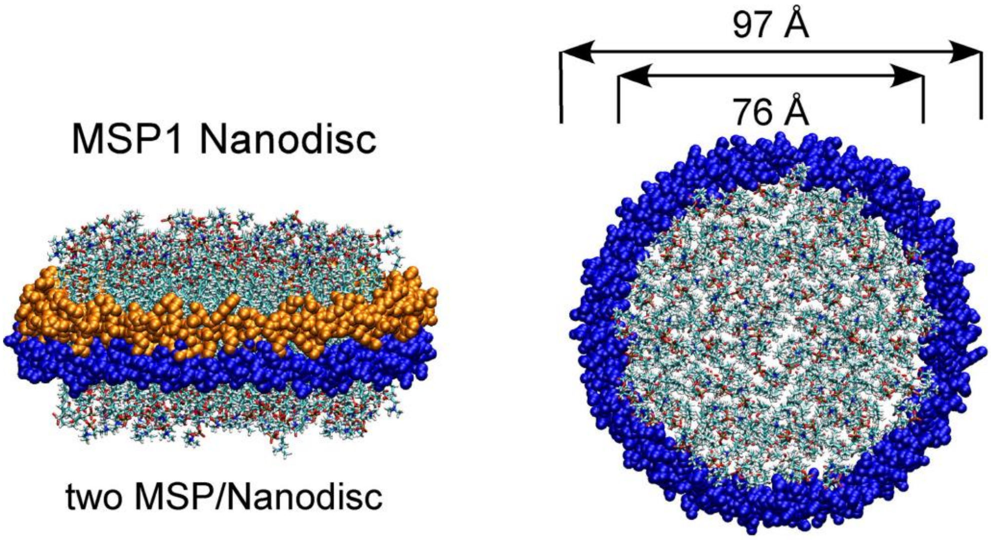

Figure 26: Schematic depiction of a nanodisc consisting of phospholipids and MSP1 protein. Picture is taken from (78).

1,2-dimyristoyl-*sn*-glycero-3-phosphocholine (DMPC)

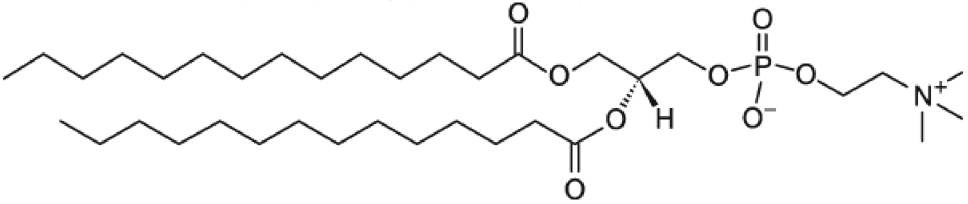

1-palmitoyl-2-oleoyl-sn-glycero-3-phosphocholine (POPC)

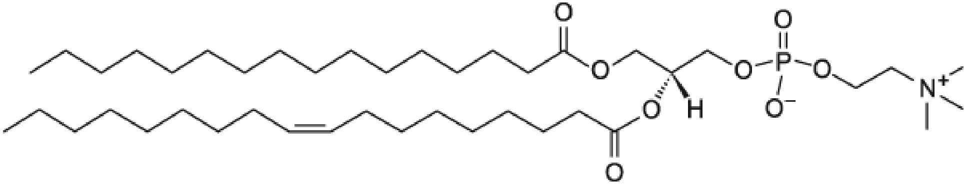

Figure 27: Structure of the lipids used for nanodisc reconstitution. Both phospholipids have no net charge. DMPC has a saturated 14-carbon-atom long fatty acid tail, while the tail of POPC consists of a saturated 16C and an unsaturated 18C fatty acid.

liposomes) nanodiscs provide a well-defined environment that allows to control the oligomeric state. Furthermore they ease spectroscopic measurements because of the small size that minimizes light scattering.

The reconstitution of an integral membrane protein in nanodisc is done in 3 steps:

1. The solubilized membrane protein is mixed with MSP and lipids solubilized in cholate at a certain ratio.
2. The detergent (of the membrane protein and the cholate) can be removed by biobeads or dialysis (dependent on the cmc of the detergent and the requirements of the protein).
3. The reconstituted membrane protein in the nanodisc is purified from small amounts of aggregate and the residual components by size exclusion chromatography. At the same time this step enables to validate the dispersity and yield of the final nanodiscs.

3.4.1.1 Optimization of the reconstitution procedure

3.4.1.1.1 ***MSP1D1:lipid ratio***

First the nanodisc reconstitution procedure was tested for 1,2-dimyristoyl-*sn*-glycero-3-phosphocholine (DMPC, Figure 27) without incorporating ChR2. DMPC is a phospholipid with a saturated 14-carbon-atom long fatty acid tail. Due to the

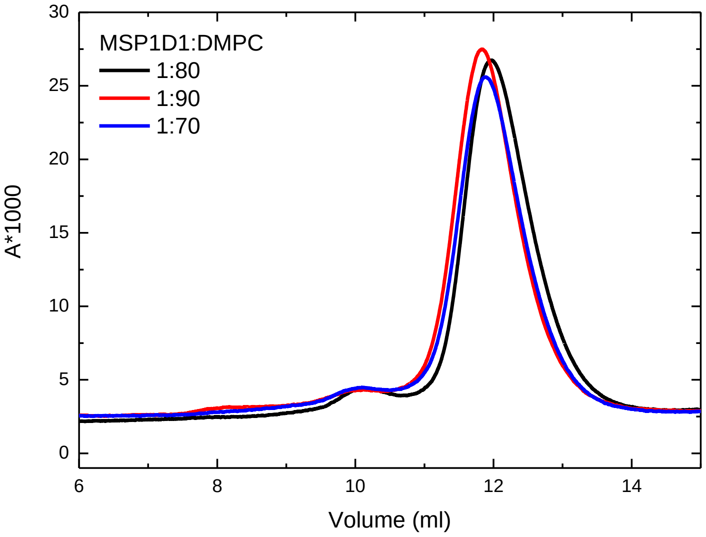

Figure 28: Chromatogram of reconstitution product of MSP1D1 and DMPC at different mixing ratios. Conditions: pH 7.4, incubation: 1 h before biobeads addition, 2 h after adding biobeads.

saturated tail it is very stable, while having a moderate melting point of 23°C (80). Typically protocols in literature (53) recommend the incubation and detergent removal at a temperature close to the melting point of the lipid (53,81). The MSP1D1:DMPC ratio suggested in literature is 1:80. In a first trial the 1:80 ratio and ratios deviating about 10% from this ratio using otherwise standard conditions (pH 7.4) were tested. The chromatogram shows very similar size distribution for all three reconstitution products (Figure 28). Size and width of the DMPC nanodiscs elution peak at 12 mL is in line with published results (53).

3.4.1.1.2 *POPC nanodiscs*

In order to have a lipid environment with a melting point less close to room temperature and a longer hydrophobic tail probably suiting the length of the hydrophobic transmembrane region of ChR2 better, 1-palmitoyl-2-oleoyl-sn-glycero-3-phosphocholine (POPC, Figure 27) was tested for reconstitution. POPC has a tail consisting of a saturated 16C and an unsaturated 18C fatty acid. The melting point is at -2°C and literature (53) suggests a temperature of 4°C for the reconstitution and a MSP1D1:POPC ratio of 1:65. Again the MSP1D1:lipid ratio was varied to find optimal conditions (Figure 29). The narrowest size distribution showed the mixing ratio of 1:75. All ratios showed an approximately 2-fold reduced recovery of POPC-nanodiscs in comparison to DMPC-nanodiscs. Because of the limited ChR2 supply it seems advisable to use DMPC for the reconstitution of ChR2.

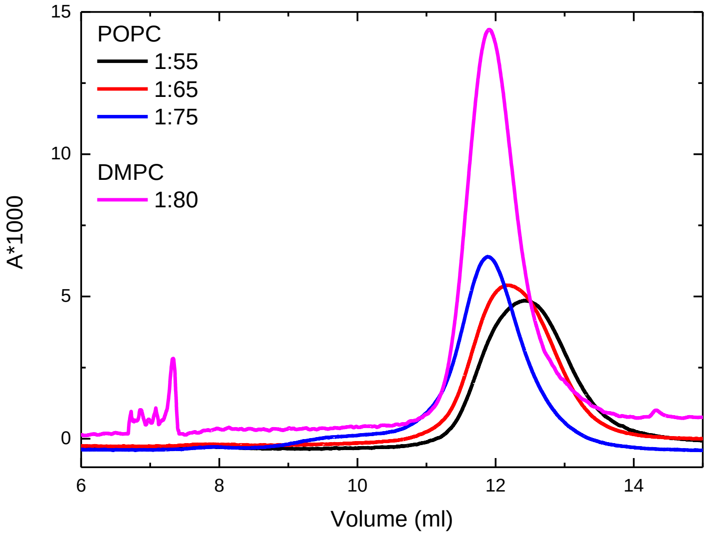

Figure 29: Chromatogram of reconstitution product of MSP1D1/DMPC and MSP1D1/POPC at different mixing ratios. The Chromatogram of the DMPC-nanodiscs shows an artefact between 6 and 8 mL due to pressure fluctuation during the measurement. Conditions: pH 7.4, incubation: 1 h before biobeads addition, 2 h after adding biobeads.

3.4.1.1.3 *Effect of pH*

Since the cysteine-reduced ChR2 variants are more photostable at pH 6.0 than pH 7.4 the effect of pH on the reconstitution process itself was investigated at a MSP1D1:DMPC ratio of 1:80. The chromatogram shows that the yield of nanodiscs is about 3 times lower for pH 6.0 in comparison to pH 7.4 (Figure 30). These findings advocated to use a pH of 7.4 also in the following reconstitutions of ChR2 in nanodiscs.

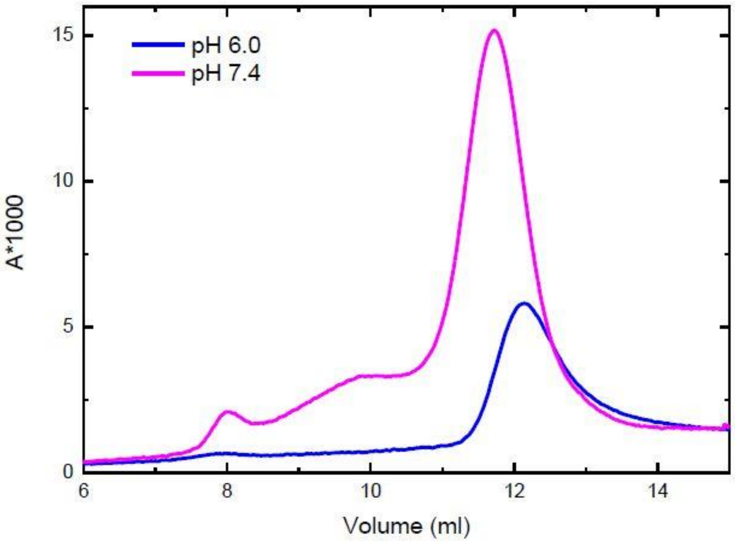

Figure 30: Chromatogram of reconstitution product of MSP1D1 and DMPC at different pH. Conditions: MSP1D1:DMPC=1:80, incubation: 1 h before biobeads addition, 2 h after adding

3.4.1.2 Optimization of ChR2 reconstitution

The preliminary tests suggested reconstitution of ChR2 into nanodiscs containing DMPC at pH 7.4. In order to get optimal yields the reconstitution conditions had to be optimized with respect to ChR2. For these studies ChR2-C79/C128T/C208 was used, as this variant is available in high amounts due to its good expression yields. From literature it is known that DMPC-MSP1D1 nanodiscs with incorporated bacteriorhodopsin trimers elute from the Superdex 200 HR 10/30 column as a single peak after about 12 mL (79). At about 8 mL a fraction elutes that is too large to penetrate the porous beads of the column, which is called void volume. Additional peaks between 8 and 12 mL can be attributed to larger aggregates (79). Thus the self-assembly of a membrane protein in nanodiscs is imperfect and yield also, depending on the degree of optimization, residual amounts of aggregates.

The rationale behind the following experiments was to find conditions, which optimize the monodispersity of the nanodiscs and the recovery of ChR2. Therefore to find conditions which give a single elution peak at a volume slightly smaller than the empty DMPC nanodiscs (12 mL) with a maximal amplitude at a given ChR2 concentration.

3.4.1.2.1 ***MSP1D1:lipid ratio***

For the reconstitution of a membrane protein into nanodiscs fewer lipids are needed, since the membrane protein occupies some part in the final lipid bilayer. Accordingly the scaffold protein to lipid ratio has to be optimized for the individual membrane protein. Different MSP1D1:DMPC ratios were tested while having a constant MSP1D1:ChR2 ratio of 1:1, consequently having one ChR2 dimer per nanodisc. The chromatogram in Figure 31 shows, that the reconstitution seems to work in a range

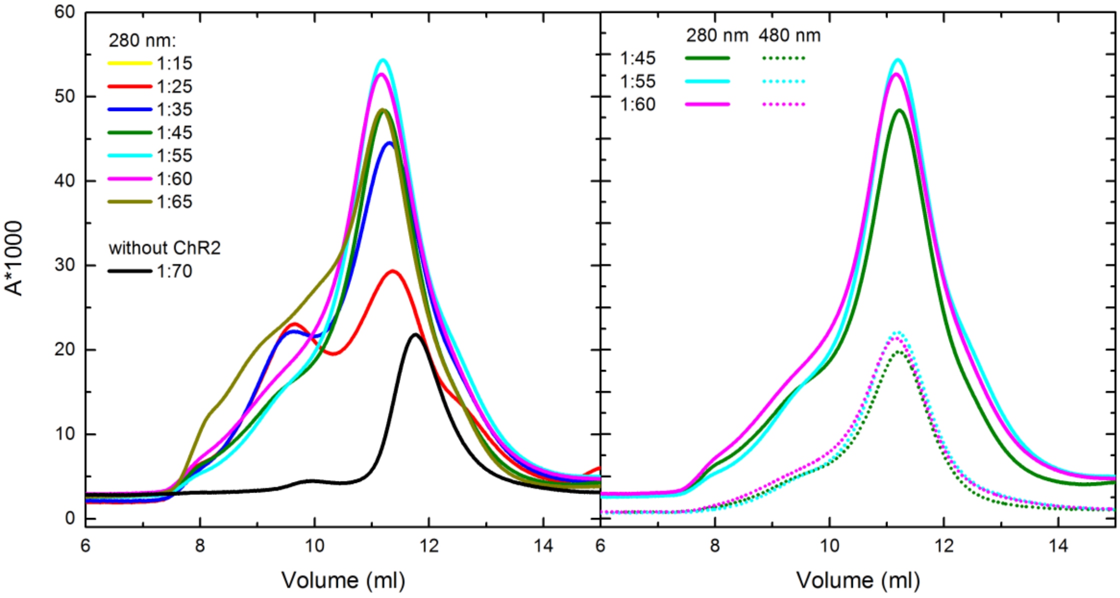

Figure 31: Chromatogram of reconstitution of ChR2 in DMPC nanodiscs at different MSP1D1:DMPC ratios. Conditions: pH 7.4, MSP1D1:ChR2=1:1, incubation: 1 h before biobeads addition, 2 h after adding biobeads.

of 1:45 to 65 MSP1D1:DMPC, although the best ChR2 recovery and narrowest size distribution is found using a ratio of 1:55. In comparison to empty DMPC nanodisc (~12 mL, see Figure 28) the elution peak of the ChR2 nanodiscs is clearly shifted to lower volume (~11 mL) and accordingly of higher hydrodynamic radius. Thus significant amounts of nanodiscs not occupied by ChR2 can be identified by a peak/shoulder at ~12 mL. The right side of Figure 31 illustrates that the elution peak at 480 nm follows nicely the absorption at 280 nm indicating that there are no larger populations of empty nanodiscs.

3.4.1.2.2 *Biobeads incubation time*

After mixing scaffold protein, ChR2 and lipids the reconstitution mixture is incubated before the detergent is removed by addition of biobeads. In the literature the incubation time varies between 15 min to 2 h (53,79,81). The effect of different incubation times was tested on identical samples. While the incubation time has only minor effects on the width and position of the nanodisc elution peak (Figure 32), it

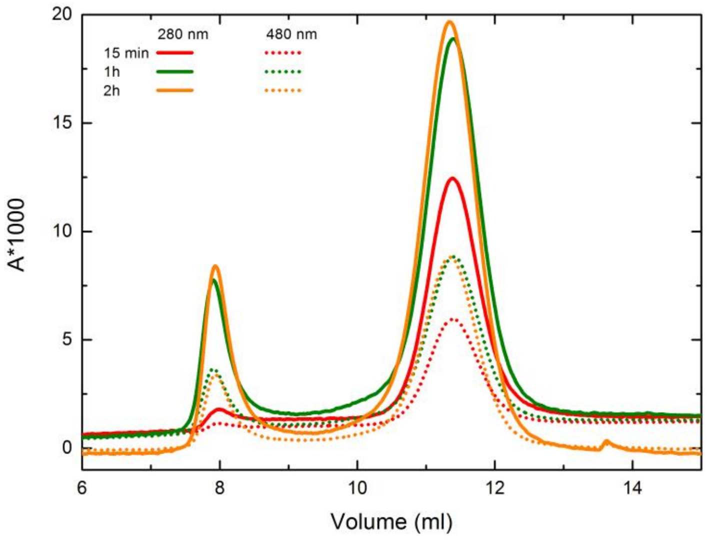

Figure 32: Chromatogram of reconstitution product of ChR2/MSP1D1/DMPC with different incubation times for the reconstitution mixture before the biobeads are added. Conditions: pH 7.4, ratio ChR2:MSP1D1:DMPC=1:1:55, incubation: 2 h after adding biobeads.

has a significant effect on the peak amplitude. Depending on the sample volume injected the exact peak position can vary by few 0.1 mL. Thus the assembled nanodiscs seem to have a similar size and monodispersity at short incubation times. The recovery of ChR2 improves upon prolonged incubation (Table 7).

Table 7: Nanodisc reconstitution with different incubation time of the mixture before biobeads addition. Conditions: pH 7.4, ratio ChR2:MSP1D1:DMPC=1:1:55, incubation: 2 h after adding biobeads.

Incubation time	15 min	1 h	2 h
recovery (ChR2)	22%	36%	50%

3.4.1.2.3 ***MSP1D1:ChR2 ratio***

The experiments above were done at a ratio of 1 MSP1D1 per ChR2. In the centrifugation step after detergent removal a pellet was visible for all these preparations. The precipitate consists of ChR2 and MSP1D1 (SDS gel, data not shown) that was thereby removed before the size exclusion chromatography. This

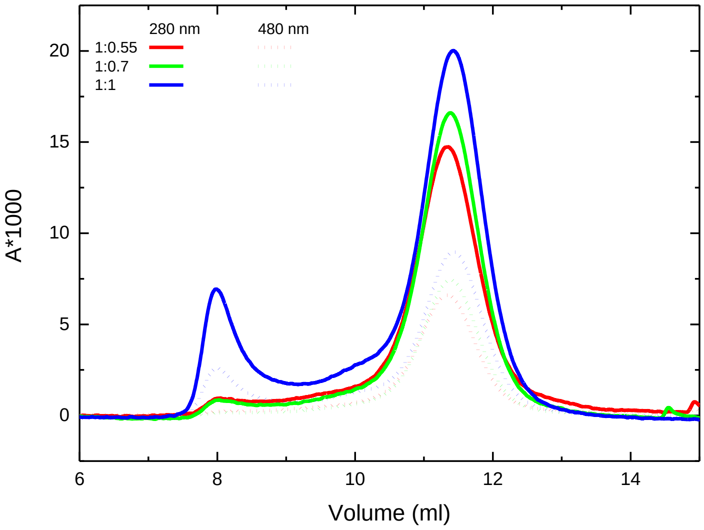

Figure 33: Chromatogram of reconstitution product of ChR2/MSP1D1/DMPC at different ratio of MSP1D1:ChR2. Conditions: pH 7.4, ratio MSP1D1:DMPC=1:55, incubation: 1 h before biobeads addition, 2 h after adding biobeads.

precipitation suggested an excess of ChR2. For that reason the effect of lower amount ChR2 per MSP1D1 was investigated, while keeping the concentration of MSP1D1 constant. Table 8 gives the ChR2 relative recovery (percentage recovered of total ChR2 used in the reconstitution) for the different ratios. The ChR2 recovery is best at a ratio of 0.55 ChR2 per MSP1D1. Figure 33 shows that the ratio does not have significant effect on the nanodiscs peak shape, thus does not lead to a population of empty nanodiscs. One might expect that a ratio of approximately 1 ChR2 per nanodisc as in case of the 1:0.55 ratio might result in a population of monomeric ChR2 nanodiscs. The chromatogram does not support this hypothesis since the peak position shifts for higher MSP1D1 to ChR2 ratios slightly to lower volume, thus to larger size. The shift is very small and thus might be an insignificant variation.

Table 8: Nanodisc reconstitution at different MSP1D1:ChR2 ratios. MSP1D1:DMPC ration was 1:50 and the MSP1D1 concentration was the same for all reconstitutions. Conditions: pH 7.4, ratio MSP1D1:DMPC=1:55, incubation: 1 h before biobeads addition, 2 h after adding biobeads.

MSP1D1:ChR2	1:0.55	1:0.70	1:1
recovery (ChR2)	63%	47%	47%

3.4.1.3 ChR2 nanodiscs characterization

A typical chromatogram of a reconstitution of empty DMPC nanodiscs and ChR2 reconstituted in DMPC nanodiscs is shown in Figure 34. The Gaussian shape of the elution peaks suggests a homogeneous size distribution of the nanodiscs. Empty nanodiscs are clearly separated from ChR2 containing nanodiscs during the size exclusion chromatography (Figure 34, black vs. blue line). The fact that the absorption at 480 nm (Figure 34, red dotted line) matches perfectly the absorption at 280 nm (Figure 34, black line) shows that at the final reconstitution conditions all nanodiscs are occupied with ChR2. In order to characterize the reconstituted nanodiscs further UV/Vis-, FTIR-spectroscopy, dynamic light scattering and PELDOR measurements were employed.

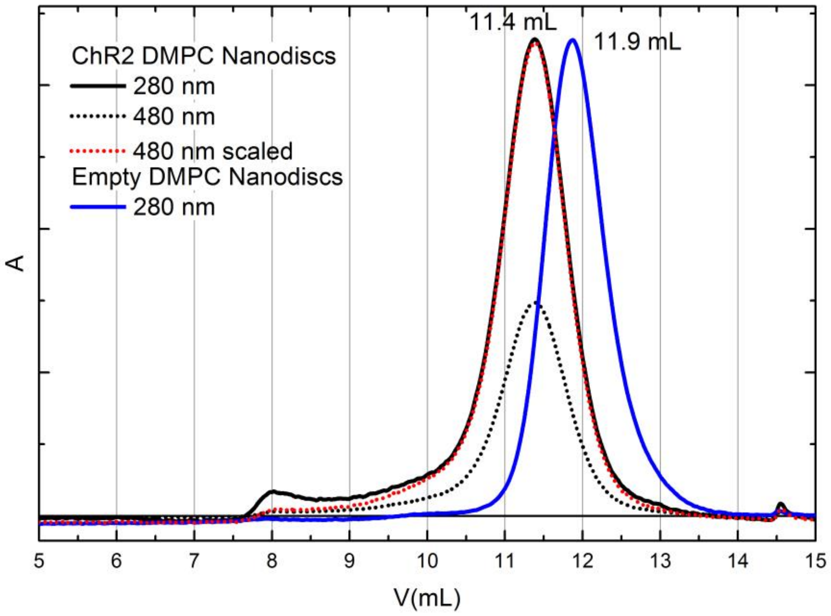

Figure 34: Size exclusion chromatogram after nanodisc reconstitution of ChR2 (black, red). For comparison empty DMPC nanodiscs (DMPC).

3.4.1.3.1 ***UV/Vis-spectroscopy***

Figure 35 shows a typical absorption spectrum of ChR2-C79/C128T/C208 reconstituted in DMPC nanodiscs. The specific absorption of the retinal cofactor has a maximum at 480 nm. The aromatic amino acid sidechains have their absorption maximum at 280 nm (see 2.3.1.1.1, p. 26ff). Since the MSP1D1 and the ChR2 protein do both feature aromatic residues, the absorption of ChR2 and scaffold protein overlay at this wavelength. The extinction coefficient for ChR2 at 280 nm is not known. Calculating the extinction coefficient from the protein sequence (using ProtParam (82)) gives a value of 77350 $M^{-1}cm^{-1}M$. The variation from these calculations for proteins which absorbance arises mostly from tryptophan is typically <10% (83). Our ChR2 construct features 10 tryptophan (ε_{280}=5540 $cm^{-1}M^{-1}$) and 14 tyrosine (ε_{280}=1480 $cm^{-1}M^{-1}$) (83). The ChR2 used for the reconstitution had typically a ratio of 280nm/480nm of 2.1. This would correspond to 20% of bleached ChR2. Assuming the same fraction of bleached ChR2 after reconstitution, using the published extinction coefficient of MSP1D1 at 280 nm (53) and of ChR2 at 480 nm,

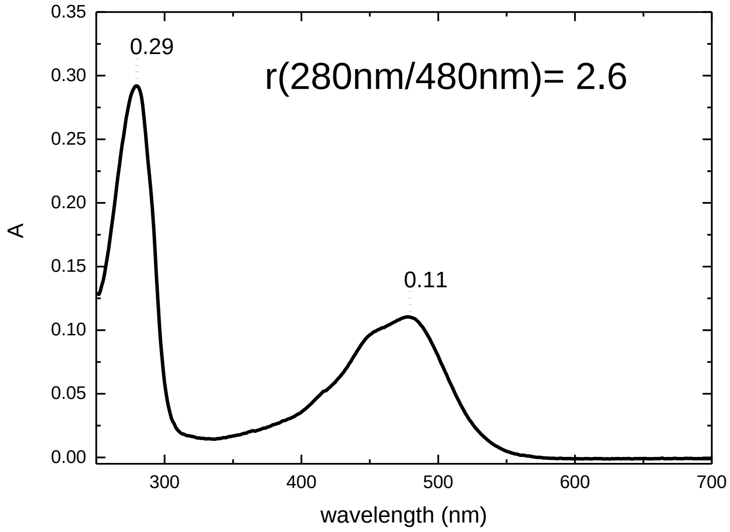

Figure 35: Absorption spectrum of ChR2-C79/C128T/C208 in DMPC nanodiscs at pH 7.4. The ratio of the absorbance at 280 and 480 nm is a measure for the purity of the ChR2 sample.

the number of ChR2 per nanodisc can be calculated. Thus 1.7 ChR2 are on average reconstituted to one nanodisc, which indicates that most likely single ChR2 dimers were reconstituted in the nanodiscs.

3.4.1.3.2 ***Summary***

Combining the results of the experiments above the optimal conditions were a molecular ratio of 0.55:1:55 (ChR2:MSP1D1:DMPC) at a pH of 7.4 throughout the whole reconstitution procedure. An incubation time of 2 h before biobeads addition and 2 h after biobeads addition gives the highest ChR2 recovery of 50-60%. But the self-assembly system seems also to tolerate ratios of ChR2 to MSP1D1 up to 1:1 and biobeads incubation times down to 15 min. Judged from the UV/Vis characterization the nanodiscs harbor most likely ChR2 dimers. Thus stochiometrically the input of reconstitution components is not necessarily the same as the output that constitutes the nanodiscs.

3.4.2 Photostability

In order to compare the photostability of ChR2-C79/C128T/C208 in detergent and membrane environment, the depletion and recovery of ground state and P_3^{530} during and after illumination was measured and is plotted in Figure 36. The reduced illumination intensity allowed to measure the absorbance during illumination. The intensities are scaled to the depletion of ground state at the onset of illumination. The detergent sample shows a continuous decay at 480 nm and 530 nm. The nanodisc sample shows a similar decay at both wavelength but with lower amplitude. The relaxation back to ground state after illumination is more than 5 times faster in

Table 9: Time constants for relaxation at 480 nm (ground state) and 530 nm (P_3^{530}) after illumination of ChR2-C79/C128T/C208 in DM detergent micelles (DM) and DMPC nanodiscs (ND)

	ND		DM	
	τ_{off1}	τ_{off2}	τ_{off1}	τ_{off2}
480 nm	35 s, 85%	181 s, 15%	12 s, 30%	220 s, 70%
530 nm	25 s	-	300 s	-

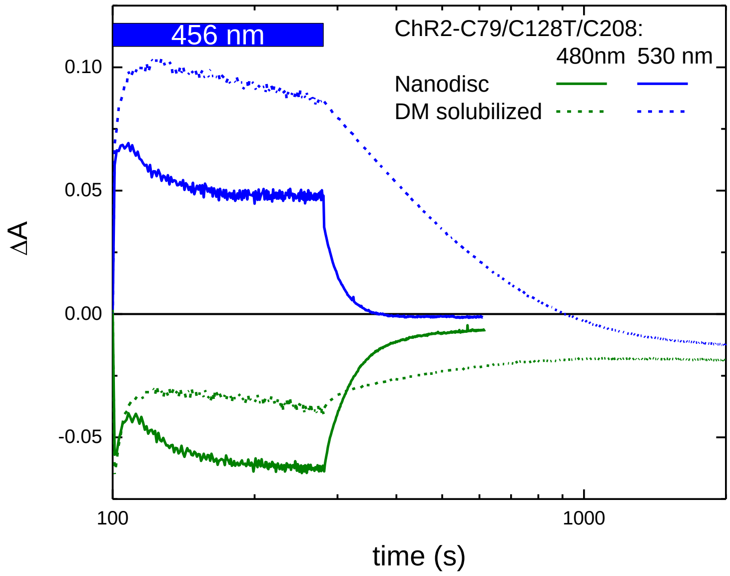

Figure 36: Kinetik of absorption differences at 480 nm (ground state) and 530 nm (P_3^{530}) during and after illumination with 456 nm of ChR2-C79/C128T/C208 in DM detergent micelles (dashed lines) DMPC nanodiscs (solid line). Conditions: 25°C, pH 6.0.

nanodiscs than in detergent (Table 9). Additionally a higher fraction of the protein recovers ground state as the absorption at 480 nm relaxes closer back to the initial level.

3.4.3 Accumulation of the open channel (P_3^{530})

The increased photostability allows to perform measurements that need to be averaged several times in order to get a sufficient signal to noise ratio, like flash-photolysis measurements. Figure 37 shows the traces of the transient absorption changes after excitation by an ns laser flash of a flash-photolysis measurement. The decay of P_2^{380} and P_3^{530} is well described by a single exponential function, while the recovery of ground state is ruled by a two exponential function with the decay constants of P_2^{380} and P_3^{530}. The co-occurrence indicates an equilibrium between P_2^{380} and P_3^{530}. The monoexponential decay reveals a direct transition from both intermediate states to ground state, which was as well observed for ChR2-C128T (31). Also since the single turnover is clearly dominated by these transitions, the photocycle seems to be well approximated for the single turnover by a simple model

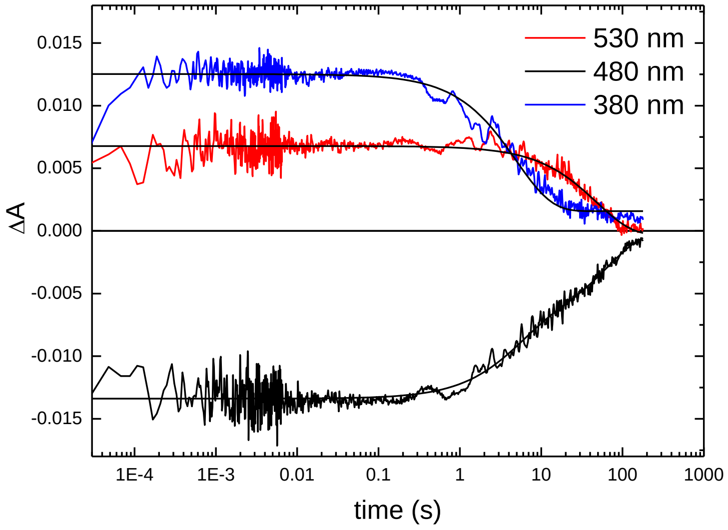

Figure 37: Transient absorption changes after ns laser excitation (450 nm) of ChR2-C79/C128T/C208 in DMPC nanodiscs. Conditions: 25°C, pH 7.4

featuring solely these transition and neglecting the branch that lead to the sustained hydrolysis of the Schiff base (as described in 3.3.2, p. 51ff). P_3^{530} decays 10 times slower than P_2^{380} and will thus accumulate at constant illumination.

Table 10: Time constants for global fit of transient absorption changes after ns laser excitation of ChR2-C79/C128T/C208 in DMPC nanodiscs in Figure 39. Values for ChR2-C128T are taken from (31)

ChR2-	P_2^{380} → Ground state	P_3^{530} → Ground state
C79/C128T/C208	5 s	65 s
C128T	2.2 s	29 s

Before the PELDOR measurements of the nanodisc samples the illumination conditions were optimized for the purpose of getting a homogenous open state sample by accumulating as much P_3^{530} as possible. pH 6.0 and 7.4 and different excitation wavelength (λ_{max}=405, 420, and 456 nm; see Figure 38 A/B) were compared at 5°C. In FTIR it was shown, that the first excitation cycle yields higher excitation efficiencies than the following excitation cycles (35). Therefore the comparison was done with a fresh sample of the same batch of protein for every

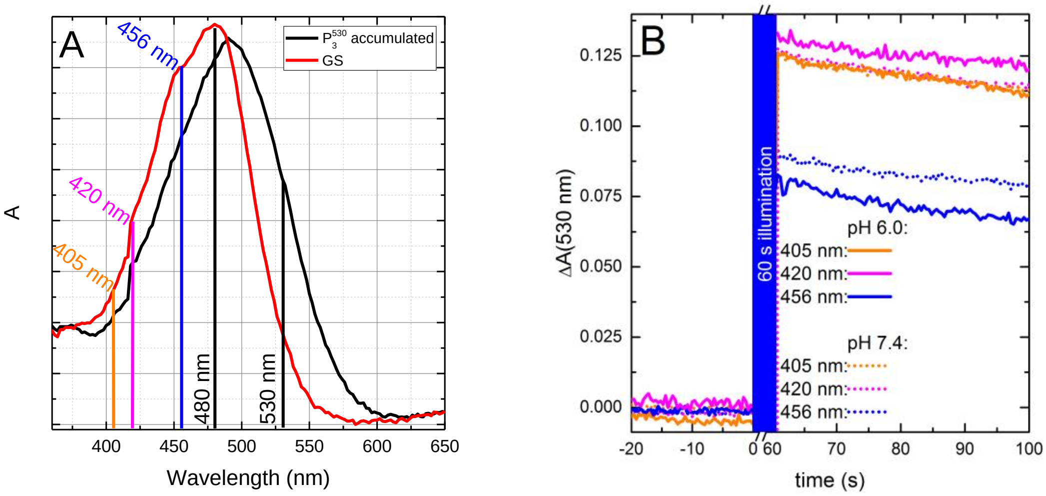

Figure 38: ChR2-C79/C128T/C208 UV/vis absorbance spectra/kinetics: Relaxation after 1 min of illumination (start of illumination t=0 s); A: Spectra recorded before illumination (red line) and 80 s (black line) after illumination; B: Amplitude of the absorbance changes after illumination at 405 nm (orange lines), 420 nm (magenta lines) and 456 nm (blue lines) at pH 6.0 (solid lines) and pH 7.4 (dotted lines). Conditions: 5°C, pH 6.0, 50% (V/V) glycerol, illumination for 1 min.

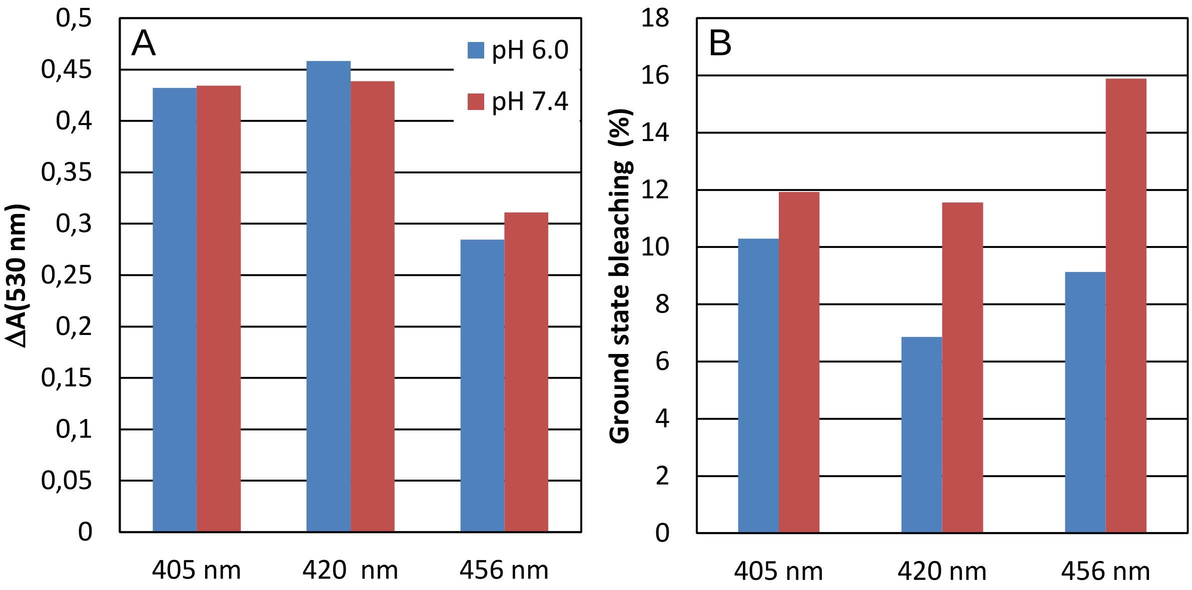

Figure 39: ChR2-C79/C128T/C208 UV/vis absorbance changes after 60s of illumination at different pH wavelength (Figure 38): A: Absorbance at 530 nm after 1 min illumination at pH 6.0 (blue) and pH 7.4 (red); B: Percentage of absorbance decrease at 480 nm after 1 min illumination and complete relaxation. Conditions: 5°C, pH 6.0, 50% (V/V) glycerol, illumination for 1 min.

illumination condition. The protein was purified, MTSL labeled and reconstituted in dim-light/red-light. Each illumination condition in Figure 38 represents a first illumination cycle for the respective sample. pH 6.0 (solid lines) and 7.4 (dotted lines) give after 60 s excitation at 405 nm (orange lines) or 420 nm (magenta lines) virtually the same amount of P_3^{530} as judged by the absorption increase at 530 nm. When excited at 456 nm (blue lines) about one third less P_3^{530} accumulates, that is consistent with the results in detergent at the same illumination conditions (see 3.3.2, p. 51ff). The results are summarized in Figure 39 A. The decay of P_3^{530} advances with a τ in the range of several minutes. Thus also after illumination P_3^{530} is predominantly in the sample for several minutes and can be spectroscopically characterized.

Looking at the decrease of the ground state absorption after complete relaxation, differences between both pH conditions become evident (Figure 39 B). Higher pH favors the bleaching of ground state, as already observed in the detergent solubilized samples (Figure 22). 420 nm excitation at pH 6.0 leads only to ~7% bleaching, so about 93% of ground state is recovered, which is slightly more compared to the other wavelengths.

Using excitation wavelengths more distant to the probing wavelength enabled us to efficiently block scattered light with a cutoff filter and to resolve the time course of P_3^{530} absorption during illumination (Figure 40). The most promising illumination conditions from Figure 39 were reinvestigated focusing on the duration of illumination. Consistent with the previous results the time course of P_3^{530} accumulation is very similar for pH 6.0 (magenta bold line) and pH 7.4 (magenta dotted line) illuminating at 420 nm. 405 nm at pH 7.4 (orange dotted line) give a slightly lower yield of P_3^{530}. The rise of P_3^{530} is at maximum after 7 s. Taking into account that the illumination conditions might somewhat vary in temperature and light intensity, it is advisable to choose a slightly longer time period for illumination.

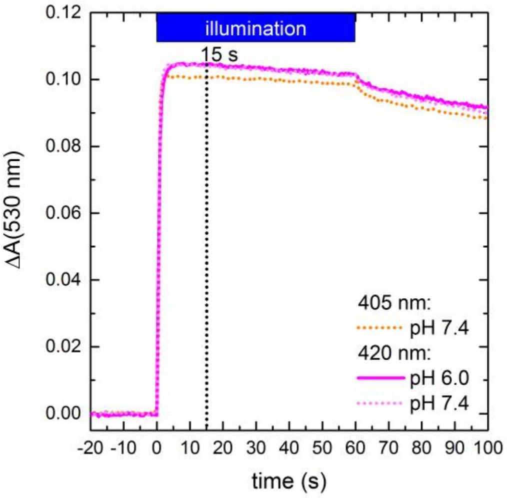

Figure 40: ChR2-C79/C128T/C208 UV/vis absorbance kinetics: Amplitude of the absorbance changes after illumination at 405 nm (orange lines) and 420 nm (magenta lines) at pH 6.0 (solid lines) and pH 7.4 (dotted lines). Conditions: 5°C, pH 6.0, 50% (V/V) glycerol, illumination for 1 min.

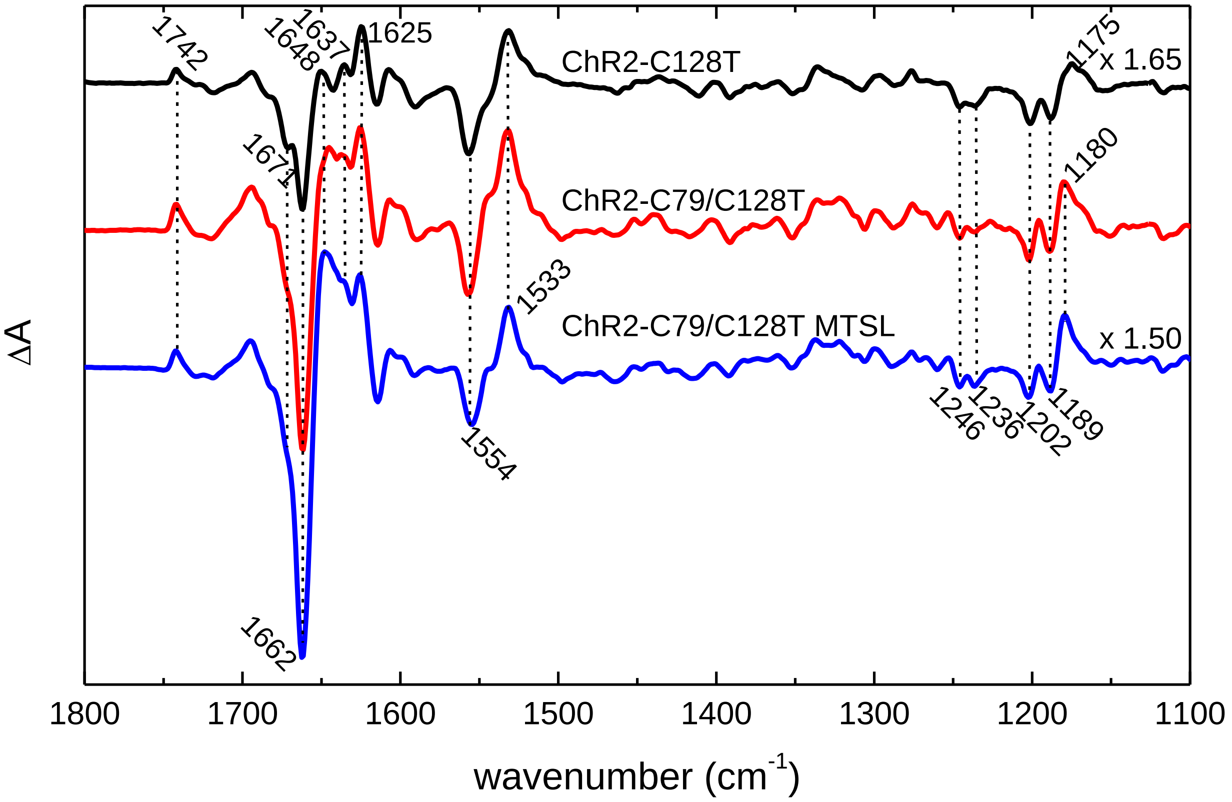

Figure 41: A: FTIR-absorption spectrum before illumination, and B: Light-induced FTIR difference spectra of ChR2 variants C128T (black), ChR2-C79/C128T unlabeled (red), and ChR2-C79/C128T unlabeled (blue). The spectra were recorded under photostationary conditions (after 20 s illumination at 420 nm, averaged 80 s) at 278 K. The spectra are scaled to the all-trans retinal band at 1246 cm^{-1}.

For the following measurements 15 s were chosen as illumination duration at 420 nm.

To have a detailed comparison between unlabeled and labeled protein in nanodiscs, FTIR difference spectra were recorded for ChR2-C79/C128T (Figure 41). The spectra were recorded during illuminating. After 20 s of illumination with 420 nm at 5°C a steady state was reached. In the following 80 s of illumination the absorbance was stable. During this 80 s period the spectra were recorded. Therefore the temperature and illumination conditions closely resemble the conditions of the PELDOR measurements. Often the spectra are scaled to the C-C-stretching vibrations of all-trans retinal in the ground state (1246, 1237, 1202 cm^{-1}). These bands represent different coupled vibrational modes (23). In the three spectra these bands have different intensities, which might indicate slightly different retinal environments in ground state. Because the difference band for the 13-cis retinal in P_3^{530} has a different maximum for ChR2-C128T the spectra were scaled to all-trans retinal in ground state at 1246 cm^{-1} (Figure 41). As already described for ChR2-C79/C128T in detergent (3.3.2, p. 51 ff.) the spectra share main features. There are substantial difference bands in the amide I region, 1662 cm^{-1}(-)/1625 cm^{-1}(+), indicating large structural changes. The difference pattern at ~1554 cm^{-1}(-)/1533 cm^{-1}(+) is assigned to the C=C double bond stretching vibration of the retinal chromophore, which is absorbing at 1554 cm^{-1} in ground state and at 1533 cm^{-1} in P_3^{530}. In conclusion both together indicates predominant accumulation of P_3^{530} and substantial structural alterations for ChR2-C79/C128T and ChR2-C128T in membrane.

Apart from these general findings there are subtle differences in the position and amplitude of several bands. The band at 1180 cm^{-1} is assigned to 13-cis retinal with a reprotonated Schiff base (ChR2-wt: 1177 cm^{-1}, ChR2-E123T: 1179 cm^{-1}) (9,19,23). The amplitude between labeled and unlabeled ChR2-C79/C128T is virtually the same, but reduced for ChR2-C128T. Also the band position is red shifted to 1175 cm^{-1} in ChR2-C128T. For ChR2-E123T the ~1175 cm^{-1} the band was suggested to arise from all-trans intermediates of a 13-cis photocycle (23). Therefore a photostationary intermediate mixture of ChR2-C128T in DMPC nanodisc with a significant contribution of nonconductive states could be possible.

The amplitude of the amide I difference bands is smaller in ChR2-C128T compared to ChR2-C79. Especially the bands around 1662 (-) and ~1650 cm^{-1} (+) are clearly larger in the cysteine-reduced variants. These bands have been assigned to α-helix hydration and correlate with channel opening (8). The shift arises from the amide C=O groups which absorption is downshifted from 1662 to 1650 cm^{-1} due to the interaction with water hydrogen. Thus the amplitude of these bands increases with the hydrated area of helices. This implies that at least some of the cysteines in ChR2-C128T prevent water to penetrate fractions of the protein upon channel opening. Since this effect was not observed in the detergent environment (see Figure 24) the DMPC nanodisc environment seems to restrict the water influx as well. The comparison of detergent solubilized ChR2-C128T with egg-PC reconstituted protein

(33) showed the same tendency. On the other hand the reduced hydration could be also a result of an increased fraction of intermediates from a 13-cis photocycle in the photostationary mixture.

In ChR2-C128T a band at 1671 cm^{-1} (-) manifests. This amide I region is assigned to the absorption of turns (57) and to have a high correlation to channel opening in several ChR2 variants (8). Also the labeled and unlabeled ChR2-C79/C128T show a shoulder at this position. The rearrangement of a turn might be a crucial event for channel opening. The bands at 1637 and 1625 cm^{-1} (+) could be related to the elongation of β-strands (57).

3.4.4 Helical movements upon channel opening

3.4.4.1 Helix B movements

The reconstituted samples have a monodisperse size distribution (Figure 34, p. 67) and on average ~2 ChR2 per nanodisc (see 3.4.1.3.1, p. 67ff). With improved illumination conditions the accumulation of P_3^{530} is enhanced (Figure 39 and Figure 40). Since pH 7.4 and 6.0 are equally suitable for P_3^{530} accumulation, both pH values were tested. The background-corrected time traces in Figure 42 (left) show clear modulations indicating a narrower distance distribution compared to the detergent samples. Thus the Tikhonov Regularization implemented in Deer Analysis (63) could be applied to resolve the distance distribution (Figure 42, right). At pH 7.4, the ground state (black line) shows a heterogeneous distance distribution consisting mainly of

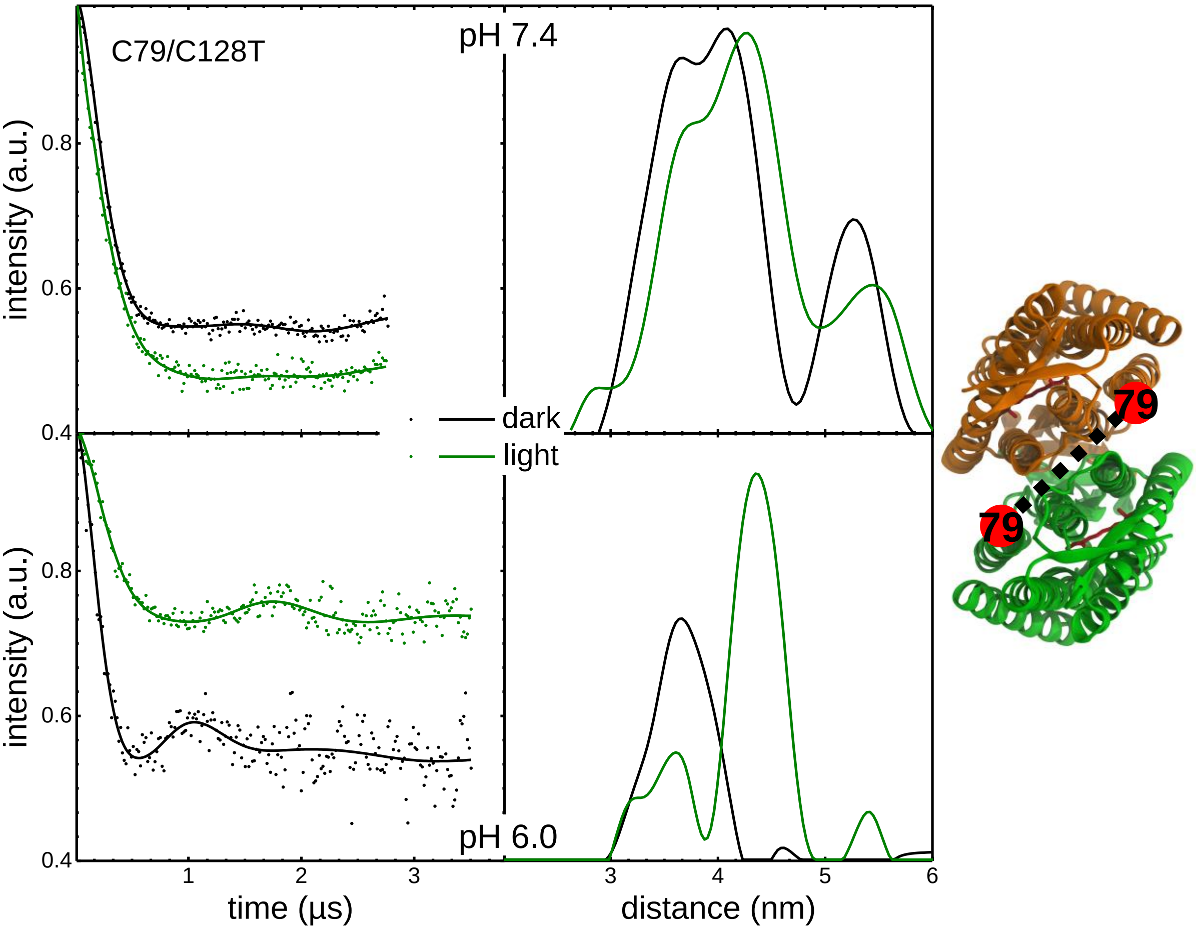

Figure 42: ChR2-C79/C128T DMPC nanodisc reconstituted, background-corrected pELDOR time trace (left) and the corresponding distance distributions (right) in dark and light state at pH 7.4 and pH 6.0.

two Gaussian curves with maxima at 3.60 nm and 4.18 nm (Table 11). From the distance distribution the cause for the heterogeneity cannot be concluded. The broad distance range between the labels might be due to the rotamer distribution of the labels or/and to different protein conformations. Rotation of two fixed MTSL molecules can increase or reduce the distance between each other by up to 1.9 nm (84). C79 is on the edge between the A-B helix loop and helix B. The A-B-loop showed to be rather flexible in the C1C2 crystal structure (7). Also combinations of a small conformational change that allows the label to explore another set of rotational angles could be possible. Thus the distance change is quantitatively difficult to interpret.

Table 11: Comparison of distance distributions in Figure 42 in dark and light state at pH 6.0 and 7.4: Two Gaussian were fitted to the distance distributions in order to compare the contribution and exact position of the main distance populations.

	pH	Center	rel. Area
Dark	7.4	3.60 nm	58%
		4.18 nm	42%
	6.0	3.65 nm	100%
Light	7.4	3.62 nm	30%
		4.28 nm	70%
	6.0	3.60 nm	20%
		4.36 nm	80%

After channel opening (green line) the second Gaussian shifts by 0.2 nm to 4.28 nm and increases in width and intensity, while the first maximum stays at the same distance but is reduced in intensity. Thus intensity shifts also from the first maximum to higher distance by ~7 Å.

The distance distribution in the ground state at pH 6.0 (Figure 42: bottom, black line) is for the main part described by one Gaussian centered at 3.65 nm, the second Gaussian at 4.18 nm is absent. The distribution after illumination (green line) still features a part of the protein population (~20%) with a label distance of 3.66 nm, while 80% are shifted by 7 Å to 4.36 nm. The population residing at 3.66 nm could be a ground state fraction of the photostationary mixture. On the other hand our ChR2 preparations seem always to contain a fraction of protein without retinal. The apoprotein might have a C79-C79 distance similar to the holoenzyme. The sample used for the pH 6.0 measurement in Figure 42 had a ratio of 280 nm to 480 nm of 2.6, which is a typical value for the ChR2 nanodiscs preparations in this work. Approximate the fraction of bleached ChR2 (see 3.4.1.3.1) gives a value of ~17%. Therefore the bleached ChR2 fraction could explain the population at 3.66 nm. The close match of the bleached fraction and the fraction at 3.66 nm also could suggest that ChR2 dimer binds/loses retinal cooperatively, similar as it was described for bacteriorhodopsin (85), and a B-B helix distance in the apoprotein similar to the holoprotein. To validate these hypotheses serial measurement investigating samples with ChR2 bleached to different degrees would be necessary.

3.4.4.1.1 ***Movement in P_1^{500}***

The almost complete conversion from one single distance maximum to another one up shifted by 7 Å sets ideal conditions to have a detailed look on the B helix movement. Spectra of early P_1^{500} measured by femtosecond IR (~100 ps) or cryo-FTIR (80 K) resemble each other in the main features (24). Substantial difference bands in the amid I region insensitive to H/D exchange (24) indicate structural rearrangements of helices like kinking. Difference bands in the carbonyl region were assigned to hydrogen bonding changes of D156 (32) and E90 (19,86). However the nature of these early changes is not clarified so far. Since the changes in the amide I do not supply any spatial information which part of the α-helical structures moves/rearranges, PELDOR spectroscopy was employed to clarify an involvement of helix B in the structural changes in early P_1^{500}. ChR2-C79/C128T was shock frozen and measured at 80 K. The sample was illuminated at 80 K, measured again, the temperature increased to 120 K, illuminated and measured again. Figure 43 B shows

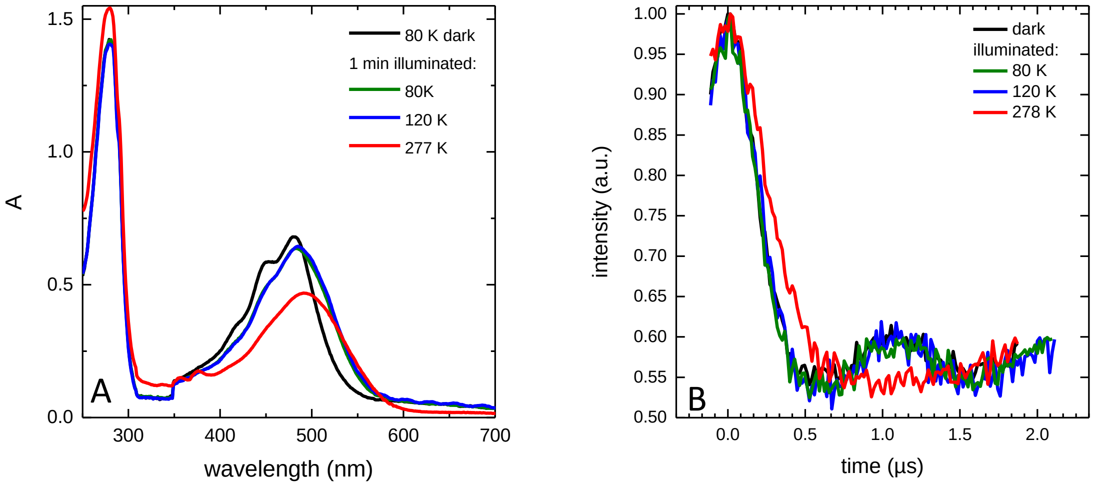

Figure 43: DMPC nanodisc reconstituted ChR2-C79/C128T measured at different cryogenic temperatures, A: UV/vis spectra before and after illumination, B: Background-corrected PELDOR time traces. Conditions: pH 6.0.

the comparison of these time traces in comparison to ChR2-C79/C128T in P_3^{520} (illuminated at RT and shock frozen). Figure 43 A shows a measurement in the UV/Vis using the identical freezing/illumination protocol with the exception that the measurement at 277 K was conducted after illumination without shock freezing. The time traces for the dark-adapted ChR2-C79/C128T and the ChR2-C79/C128T illuminated at 80 K and 120 K are identical. Therefore the intracellular part of helix B does not move in early P_1^{500}.

3.4.4.1.2 ***Movement beyond P_3^{530}***

Ground state and P_3^{530} have been characterized in terms of the helix B-B distance in the previous sections. In this section the intermediates following P_3^{530}, thus mainly P_4^{480}, are qualitatively characterized. Light conditions were optimized to accumulate about 50% (relating to the absorbance difference at 530 nm at optimized illumination conditions, ΔA(530nm), as 100%) in P_3^{530}. The sample was illuminated at the optimized condition until the maximum amplitude of ΔA(530nm) was reached, the illumination was stopped, the sample was incubated until ChR2-C79/C128T had relaxed to 50% of ΔA(530nm) and subsequently shock frozen (Figure 44 green trace). In this way ChR2, which is not accumulated in P_3^{530}, is trapped in the intermediates later than P_3^{530}, thus mainly P_4^{480}. The sample is denoted as “50% relaxed”.

Sample with half decayed P_3^{530} (50% relaxed) was compared to the samples prior to any illumination (dark) and illuminated at optimized conditions (light). All samples were from the same batch of ChR2 purification and nanodiscs reconstitution, consequently only different in the composition of the photocycle intermediates. Figure 45 shows the result of the PELDOR measurements. In the time traces the ground state sample clearly differs from the illuminated samples. The time traces of the illuminated samples show only minor differences among each other. Crucially, the resulting distance distributions of “50% relaxed” and the fully illuminated samples are almost superimposable. The close similarity between the “illuminated” and “50% relaxed” indicates a similar position of helix B in P_3^{530} and P_4^{480}.

The “illuminated” sample shows a larger ChR2 fraction residing at the ground state distance than in previous measurements (see Figure 42). The integral for the distances smaller than 3.86 nm is about 35% of the overall integral, which is 15% more as in for the pH 6.0 sample above (Figure 42, p. 77). The sample in this measurement had an absorbance ratio at 280nm/480nm of 2.8 which is 0.2 higher than usually used for the PELDOR sample and corresponds (assuming two ChR2 per nanodisc) to 23% of bleached ChR2. The discrepancy of 12% to the fraction with a distance <3.86 nm might be partly explained by the uncertainty of the integral of the overlapping distance peaks.

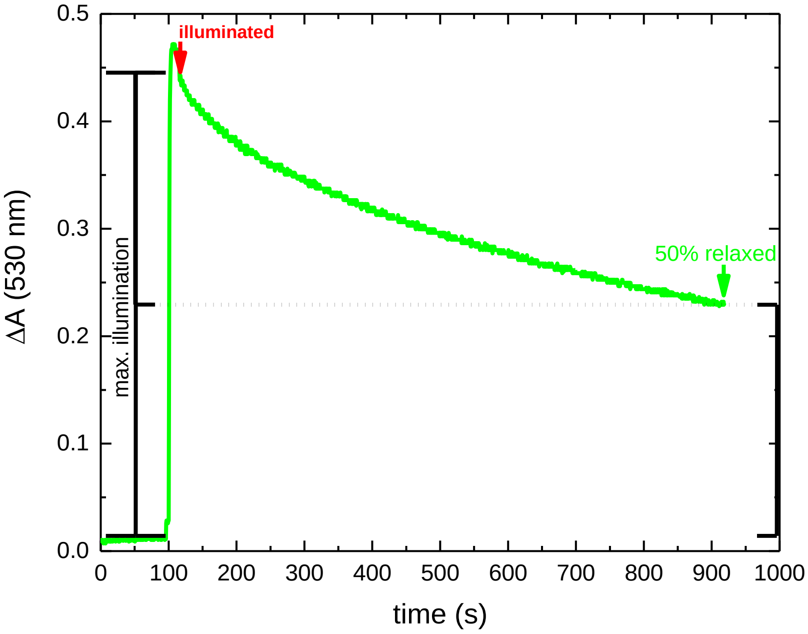

Figure 44: UV/vis kinetic at 530 nm of illumination and relaxation of ChR2-C79/C128T PELDOR sample "50 relaxed": Illumination start at 100 s, stop at 120 s. An identical protein sample was shock frozen after 20 s illumination, "illuminated". The "50% relaxed" sample was further incubated at 5°C and shock frozen when 50% of the ΔA(530 nm) were decayed.

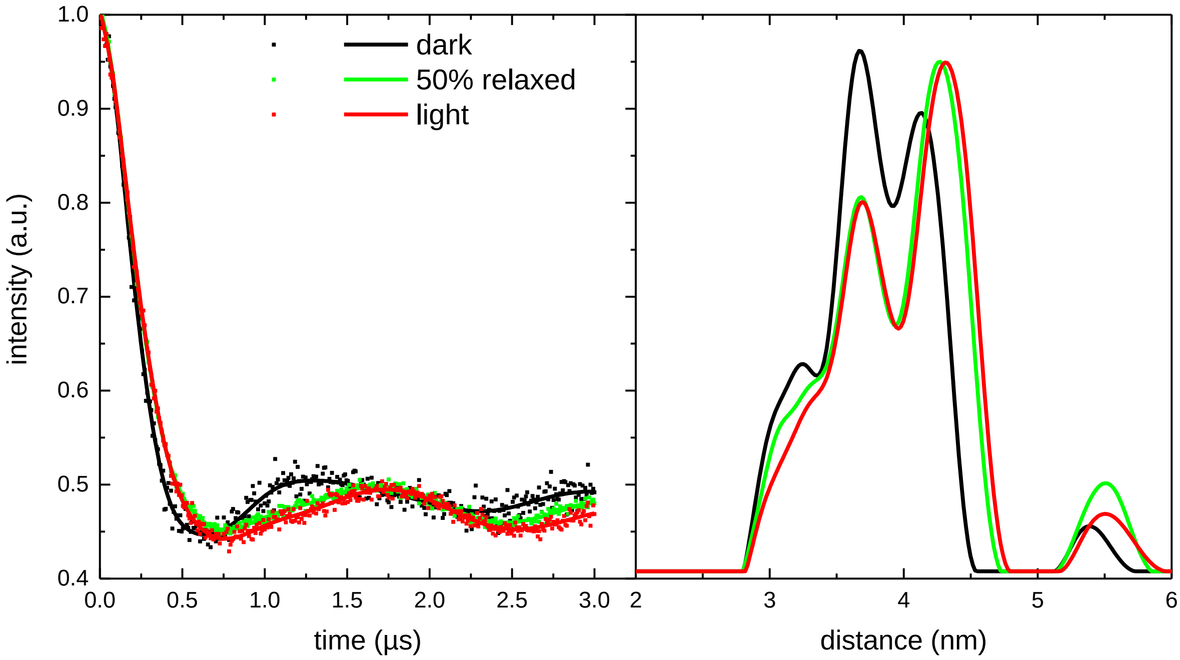

Figure 45: Background-corrected PELDOR time traces (left) of ChR2-C79/C128T sample treated with different illumination conditions (as described in the text and in Figure 46) and the corresponding distance distributions (right).

3.4.4.2 Helix F movements

The measurements in detergent showed qualitatively a movement of helix F (see 3.3.3, p. 56ff). In order to get quantitative results the ChR2-C79/C128T/C208 in nanodiscs was investigated. Having two label present per monomer results in four distances if we assume a perfectly symmetric dimer with completely homogenous monomers. Additionally the four interacting spins introduce artifacts that are broadening the distance distribution in the end. In consequence it is challenging to track a single distance in a four spin system like the helix F to helix F distance (C208 to C208) in ChR2-C79/C128T/C208. The spin-spin distance between C208 with MTSL bound was a priori estimated applying the MMM routine (87) to a ChR2 homology model. The homology model (88) was further refined by adding an explicit water/POPC membrane environment, minimization and equilibration to room temperature by Christian Spakowski (AG Bondar, 2014, pers. Comm. 2015). The results are shown in Table 12:

Table 12: MMM predictions for distances of MTSL attached to C79 and C208 in the refined ChR2 homology model (see text above). The ± value gives the relative RMSD distance deviation as calculated from MMM.

Distance (nm) in between		intra	Monomer B	
			C79	C208
	intra		2.63 ± 7.4%	
Monomer A	C79	2.63 ± 7.4%	3.65 ± 12.4%	3.72 ± 10.3%
	C208		3.71 ± 10.3%	5.05 ± 2.5%

Accordingly the helix F-F distance (~5.0 nm) is clearly distinguishable from all distances in which helix B is involved (~3.7 nm). Judged from the C1C2 x-ray crystallographic structure and the ChR2 homology model C79 is perfectly solvent accessible, while C208 is less accessible and partly buried in the protein. Recent fluorescence labeling studies indicated as well lower accessibility of C208 compared to C79 (89). This is also reflected by the lower RMSD of the C208-C208 distance compared to the distances in which C79 is involved (Table 12). To make use of the different accessibilities we reduced the 50% of the nitroxide radicals of the fully MTSL

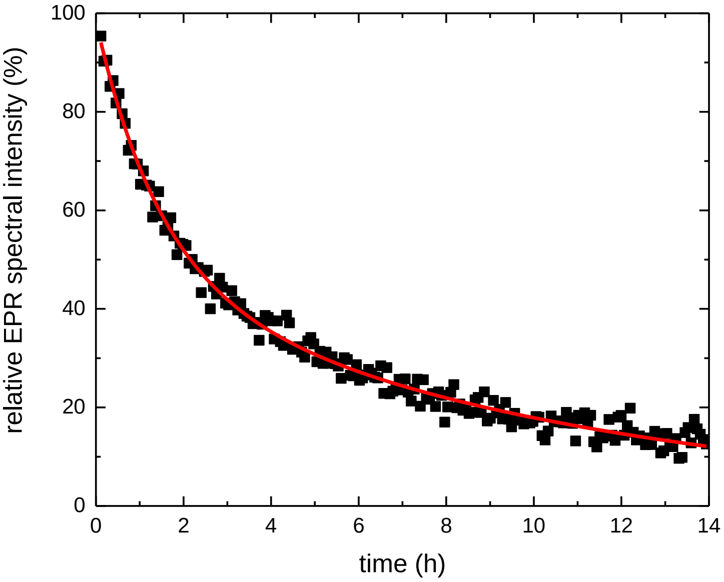

Figure 46: Reduction kinetics of MTSL label bound to ChR2-C79/C128T/C208. Conditions: 40-fold ascorbate excess relative to bound MTSL (c(MTSL)~150 µM), pH 6.0, 5°C.

labeled ChR2-C79/C128T/C208 (2.1 ±15% MTSL/ChR2) with ascorbate. On one hand we hoped to yield a relative enrichment of spins on the C208 site due to the lower accessibility. On the other hand reducing 50% of the spins in our ChR2 population turns the four spin system more towards a two spin system, which reduces the impact of artefacts on the final distance distribution. The reduction kinetics of MTSL bound to ChR2-C79/C128T/C208 are shown in Figure 46. The decay of EPR spectral intensity arising from the reduction of MTSL is clearly biphasic. The faster phase has a τ_1 of 1 h and the slower phase a τ_2 of 7 h. Both phases have the same amplitude. For the PELDOR sample ChR2-C79/C128T/C208 was incubated for 2.5 h. Thus about 82% of the fast and 25% of the slow decaying spin component are reduced. In case that the two phases originate from the different accessibilities of C79 and C208 the long C208-C208 distance should be much more pronounced than in the detergent measurements before. From the same batch of MTSL labeled ChR2-C79/C128T/C208 one part was reduced as described before. The other half was shock frozen without prior reduction in order to be able to clearly resolve the differences arising from the reduction. Figure 47 shows the non-reduced sample. The distance distribution shows

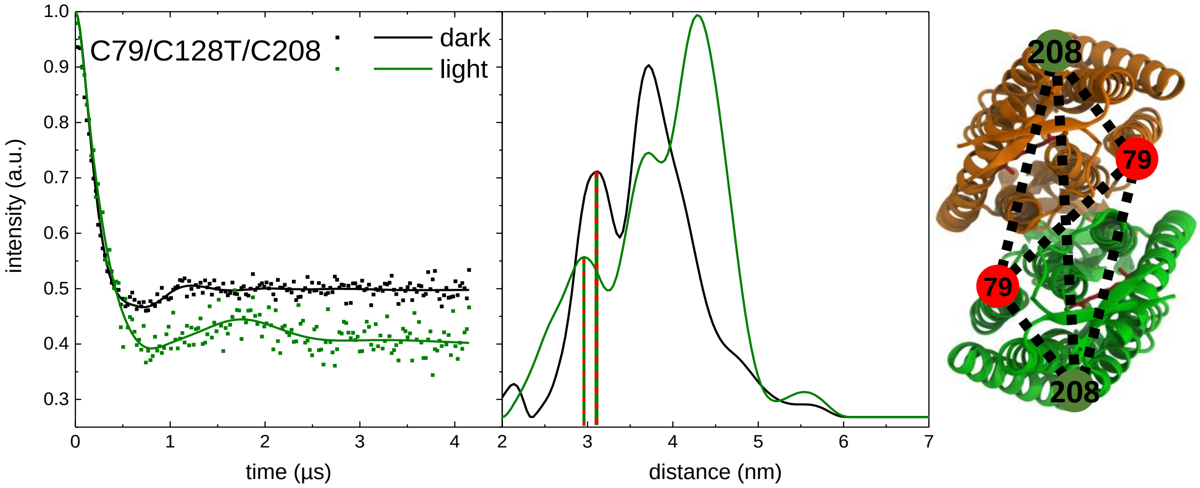

Figure 47: Background-corrected PELDOR time traces (left) of MTSL-labeled ChR2-C79/C128T/C208 and the corresponding distance distributions (right).

in ground state a maximum at ~3.7 nm as suggested from the homology model (Table 12), but also another maximum at 3.2 nm which was not predicted. Since the later distance was not observed in ChR2-C79/C128T (Figure 45, p. 82) it must be a distance in which C208 is involved – most likely the shortest predicted distance (2.63 nm) thus the intra-monomer C79-C208 distance. Other than expected from Table 12 there is no defined peak in the region around 5 nm. At ~4.8 nm and ~5.5 nm are small bands. For distances >5.5 nm the time trace length might not be sufficient, which might be the reason why the C208-C208 distance could be not resolved. In conclusion the predictions from the homology model agree well with the distance measurements for C79 but they fail for C208.

After illumination the maximum at ~4.3 nm agrees very well with the light distance distribution of ChR2-C79/C128T observed in Figure 45. The maximum in dark at 3.2 nm shifts to lower distance to ≤3.0 nm. This maximum might be assigned to the intra-monomer C79-C208 distance, thus helix B or F seem to have a movement component towards each other.

The recording of a longer time trace of the non-reduced and reduced ChR2-C79/C128T/C208 is currently underway and will help to elicit the helix F movement.

3.4.4.3 Tracing distances beyond helix B and F: Introducing additional cysteines

Yielding a rather narrow distance distribution with the optimized accumulation conditions set the stage to introduce additional cysteines in order to track additional distances. The remaining C79 puts several constraints on the location of an additional labeling site. Ideally the inter-monomer distance of the additional introduced cysteine should not overlap with the C79 inter-monomer distance. Furthermore the distance to the C79 labeling site should not overlap with the inter-monomer distance of the newly introduced label. In the dark sample the C79-C79 distance occupies the region between 3 to 4 nm and after illumination the region between 4 to 5 nm. Consequently a large inter-monomer distance of at least >4 nm or a very short distance <3 nm would be desirable. The inter-monomer distance of the putative labeling sites was evaluated by simulating the MTSL label attached to a cysteine at the respective positions using the software MMM (87). Based on these criteria 3 residues (Q117, S222 and Y196) were chosen.

In the case of Q117 the single mutation Q117C was already electrophysiologically characterized and showed photocurrents similar to wild type (90). This information promised also decent expression for a variant having the Q117C substitution introduced in the ChR-C79 background. Indeed ChR2-C79/C128T/Q117C showed expression yields comparable to ChR2-C79/C128T and both cysteines could be labeled to more than 90%.

S222 was chosen to clarify the nature of the helix F movement. Tracking the helix at two points could clarify the degree of tilting involved in the rearrangement. Additionally making use of a position in the putative ion channel and W-band measurements sensitive to H-bonding via the polarization of the nitroxide N-O bond could give direct information about the pore formation in this area. The ChR2-C79/S222C variant was successfully expressed. Unfortunately the C222 position could not be labeled. Destabilizing the protein structure by adding defolding additives (urea, DMSO) did not increase the yield of labeled holoenzyme (Figure 48). The

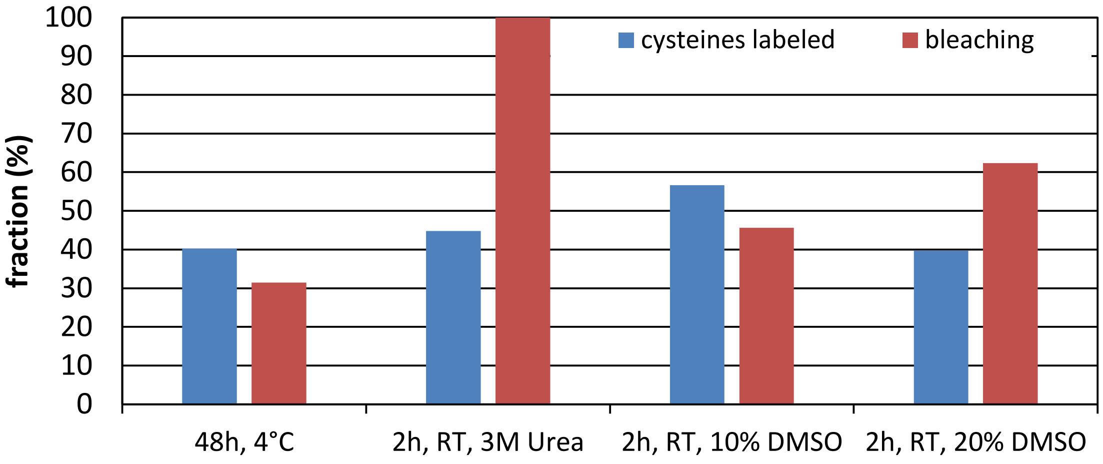

Figure 48: MTSL labeling of ChR2-C79/S222C at different conditions.

fraction of cysteines labeled per ChR2 was about 50%, i.e. one label per ChR2. With the known high labeling efficiency of C79, this means that S222C was not quantitatively labeled.

Based on molecular dynamics simulation of the C1C2 chimera in the ground state (AG Bondar), tyrosine 196 (helix D, Y196) was suggested to have an unusual stable hydrogen bond to tryptophan 223 (helix E, W223). The investigation on a variant (Y196F) with disrupted hydrogen bond at this position is described in section 3.5 (page 89 ff.). A variant having Y196 substituted by a cysteine was genetically engineered as well but did not express.

Table 13: MMM predictions for distances of MTSL attached to additionally introduced cysteines tested for expression and site specific spin labeling: “helix” indicates the helix of the “cysteine substitution”. Since in the C1C2 ChR2 structure the monomers within the dimer are complety symmetrical a newly introduced cysteine to ChR2-C79/C128T creates three new distances: The intra- and inter-molecular distance between the introduced labeling site and C79, as well as the distance between the introduced labeling side between the monomers of the dimer.

Helix	cysteine substitution	distance (nm)			expression/ label-accessible
		C79 intra-molecular	C79 inter-molecular	introduced amino acid inter-molecular	
C	Q117C	3.0	3.8	2.7	yes/yes
F	S222C	3.1	3.6	5.3	yes/no
E	Y196C	3.1	2.6	4.6	no/-

3.4.4.3.1 *The helix C-C distance: A solid dimer interface*

The C-C helix distance is well suited to test the integrity of the dimer interface. In the cysteine-reduced variants the cysteines that bridge the dimer by two disulfide bonds were removed as well. Thus the above observed distance changes could be due to a reorientation of the monomers with respect to each other, rather than a movement of a domain within the monomers. The sequence position 117 is at the extracellular end of helix C. The software MMM approximates an intermonomer distance of 2.7 nm between two MTSL labels bound to position 117 in a dimer (Table 13). Thus the distance should be clearly separated from the distances arising from the labeled C79 (Figure 45, p. 82). Indeed the distance distribution for ChR2-C79/C128T/Q117C in the ground state shows a distance peak at 2.75 nm (Figure 49 blue line) that does not move upon channel opening. This suggests a strong interaction between the monomers, which is supported by the fact that on a reducing SDS page residual ChR2 running at the dimer size is observed.

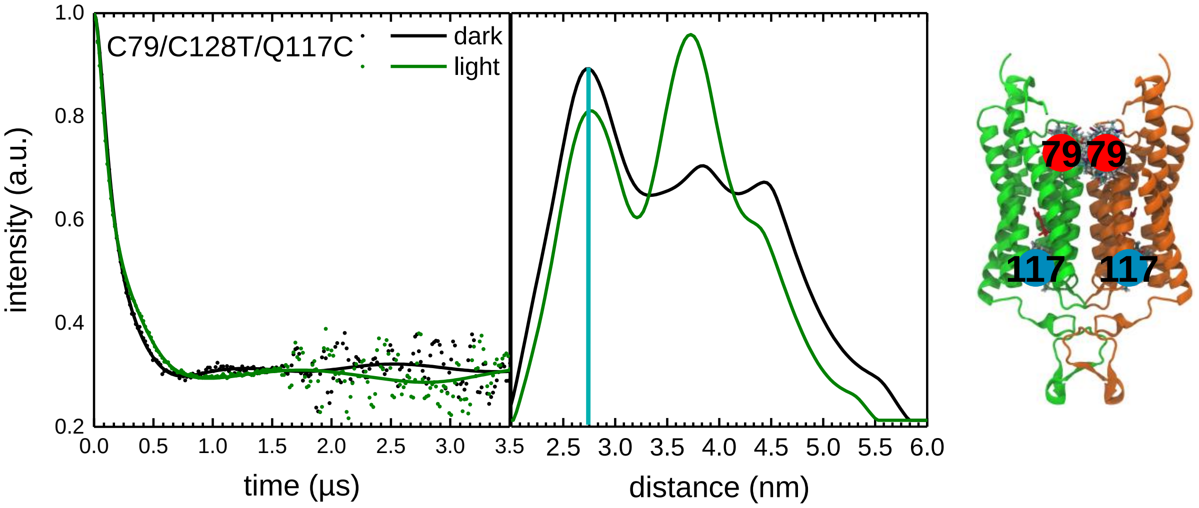

Figure 49: Background-corrected PELDOR time trace (left) of DMPC nanodisc reconstituted ChR2-C79/C128T/Q117C and the corresponding distance distributions (right). The blue line indicates the C117 inter-monomer distance in the distance distribution.

3.5 The Y196F variant: Localizing a dangling water

The H-bond between Y196 and W260 (see Figure 50) was identified in MD simulations of the ground state of C1C2-chimera as one of the strongest in the protein (C. Mielack, A.N. Bondar 2014, pers. Comm.). This helix E-G connection was abolished by eliminating the OH of Y196, thus exchanging tyrosine 196 with a phenylalanine. The kinetics of ChR2-Y196F were compared to WT and a steady state FTIR spectrum of P_4^{480} was recorded to clarify the functional significance of this strong H-bond. Later simulations suggested that a weakly hydrogen bonded water molecule which existence was shown by FTIR (91,92), a so called "dangling water", is located next to W260. Thus the water region of the P_4^{480} FTIR spectrum was analyzed with respect to differences to ChR2-WT.

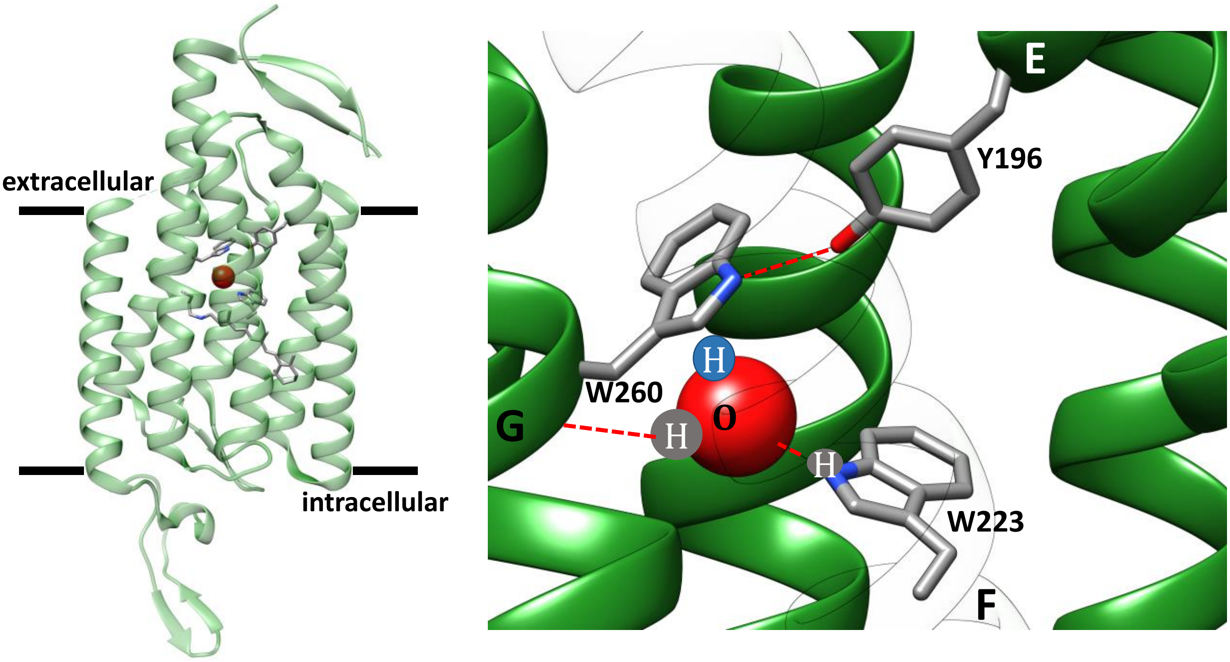

Figure 50: Hydrogen bonding network of Y196 in C1C2 chimera structure (PDB: 3UG9). The residues shown are conserved in ChR1 and ChR2. The water hydrogen close to W260 is supposed to interact weakly with the π–system of the tryptophan and the respective O-H stretching vibration (the respective hydrogen atom is depicted in blue) to give rise to the "dangling water" vibration. The other water hydrogen interacts with the backbone of helix G, while the oxygen is hydrogen bonding with W223.

3.5.1 Results

Figure 51 shows a flash-photolysis measurement comparing characteristic wavelength of ChR2-Y196F with ChR2-WT. In Table 14 the time constants fitted to traces recorded in 20 nm steps from 320 nm to 600 nm using 5 exponential functions are shown. τ_1 characterizes the decay of P_1^{500} and the rise of P_2^{390}, τ_2 a second phase of P_2^{390} formation with lower amplitude, τ_3 the decay of P_2^{390} and rise of P_3^{530}, τ_4 the decay of P_3^{530} and τ_5 the decay of P_4^{480} to ground state. ChR2-Y196F shows slightly delayed kinetics of all intermediates apart from the decay P_4^{480}. Because of the ChR2-Y196F time trace length of 0.9 s the τ_5 is most likely underestimated by the fit. Over all the kinetics diverge by less than a factor of 2 and are very similar, thus they give no indication for a crucial functional role of the Y196-W260 hydrogen bond.

Table 14 shows that P_4^{480} decays at least three orders of magnitude slower than any other intermediate state. In consequence under continuous illumination P_4^{480} is accumulated and the P_4^{480} state is characterized by the FTIR difference spectrum in Figure 52. The large amide-I difference bands, indicating a helix hydration, have been shown to persist from P_2^{390} to P_4^{480} (9,19). Therefore the experimentally easy accessible FTIR light-dark difference spectrum is in many cases a good measure for an influence of mutations in ChR2. Figure 52 shows the comparison between the FTIR light-dark difference spectra of ChR2-Y196F and –WT. The spectra are scaled to the all-trans retinal absorption band of ground state ChR2 at 1246 cm^{-1}. The region from 1100 to 1800 cm^{-1}, which features absorption bands of vibrational modes of carboxylic acids, of the amide backbone as well as retinal specific bands, is essentially superimposable. In conclusion the FTIR difference spectra as well as the kinetic traces in the UV/Vis do not indicate any functional relevance of the Y196-W260 hydrogen bond.

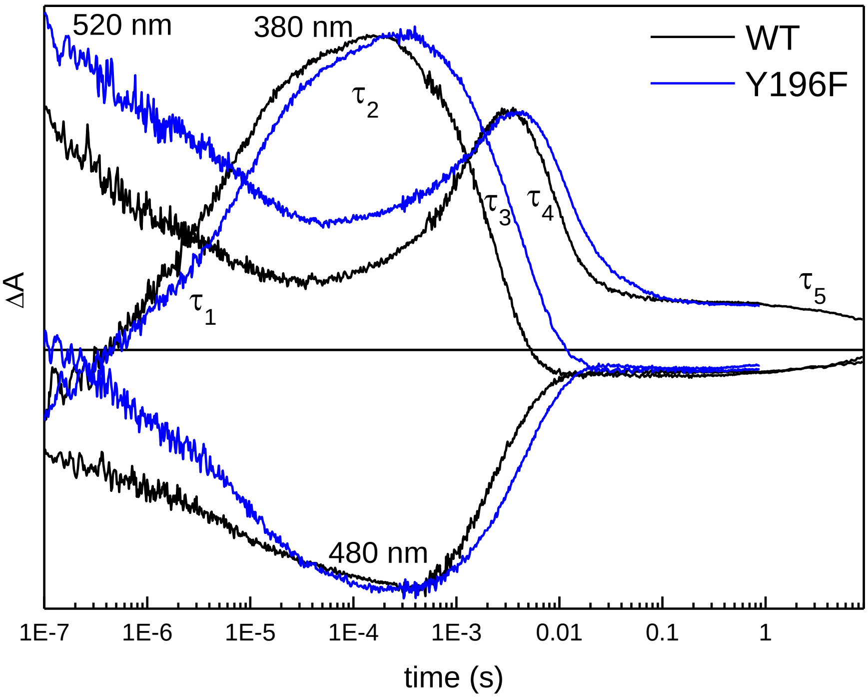

Figure 51: Transient absorption changes after ns laser excitation (450 nm) of ChR2-Y196F (blue) in comparison to ChR2-WT (black), both solubilized in DM. The three traces are characteristic for the four intermediates of the photocycle: At 520 nm P_1^{500} (decay) and P_3^{520} are observed. The trace at 480 nm reports on the P_4^{480} and ground state. 380 nm shows the formation and decay of P_2^{390}. Conditions: 25°C, pH 7.4

Table 14: Time constants of the decay of the different intermediates from global fit of transient absorption changes after ns laser excitation of ChR2-Y196F solubilized in DM. Kinetic traces were recorded between 320 nm and 600 nm and fitted by 5 exponentials. Conditions as in Figure 51.

ChR2-	τ_1 P_1^{500} (µs)	τ_2 P_{2a}^{390} (µs)	τ_3 P_{2b}^{390} (µs)	τ_4 P_3^{530} (ms)	τ_5 P_4^{480} (s)
WT	7.2	156	1.9	6.5	7.4
Y196F	9.9	191	3.3	8.3	(1.4)

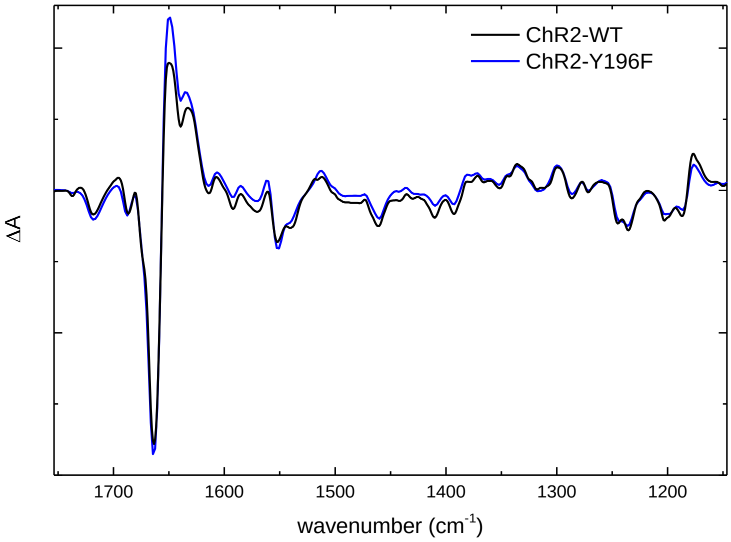

Figure 52: Light-induced FTIR difference spectra of ChR2-Y196F (blue) and –WT (black). The spectra were recorded under photostationary conditions (456 nm illumination) at 25°C and scaled to the all-trans retinal band at 1246 cm^{-1}. At these conditions P_4^{480} is dominant in the photostationary mixture.

Although the major functional features seem to be preserved in ChR2-Y196F there are subtle differences in a single O-H stretching vibrations of a weakly hydrogen bonded internal water molecule, a so called “dangling water” (Figure 53). Liquid water has a very broad absorption band in the infrared from ~2800 to ~3700 cm^{-1}. In order to minimize the influence of the broad water background on the band position and to ease the comparison of both spectra, the second derivative is plotted in Figure 53. The dangling water is a structural water molecule that lacks a strong hydrogen acceptor for one of the hydrogens. Already minor changes in the hydrogen bonding strength of the weakly hydrogen bonded H can lead to a significant spectral shift. Rozenberg et al. analyzed the dangling water hydrogen bond length in various hydrates, organic acid salts and carbohydrate crystals with respect to the respective vibrational band position and came up with an empirical correlation (93). The correlation allows to estimate the structural displacement that is necessary to explain the spectral shifts (Table 15). Accordingly the shift of ~14 cm^{-1} between the ground state OH-bands in ChR2-Y196F (3640 cm^{-1}) and WT (3626 cm^{-1}) corresponds to an increase of 0.24 Å of the weak hydrogen bond of the dangling water. The respective shift in P_4^{480} of ~12 cm^{-1} matches an increase of 0.14 Å. The effect of the Y196F mutation on the ground state structure was further investigated *in silico* employing molecular dynamics simulations. The calculated distance changes between W260 are too small to be tracked in the molecular dynamics simulations, but the simulations show a destabilized orientation of W260 due to the lacking hydrogen bond with Y196 (C. Mielack, A.N. Bondar 2015, pers. Comm., publication in preparation). W260 in ChR2-Y196F is in comparison to ChR2-WT slightly more rotated towards the protein backbone of helix F, which might be responsible for the observed small increase in the hydrogen bonding distance between W260 and the dangling water (see Figure 50). The assignment of water next to W223 as the dangling water is fortified by the observation, that ChR2-C128T shows a clear band position shift in the dangling water region since C128 is in close proximity of W223. The difference spectra of ChR2-C128T and –C79/C128T/C208 were recorded at 5°C and pH 6.0, thus at different conditions as the other difference spectra (20°C, pH 7.4) in Figure 54. However FTIR studies of the dangling water in bacteriorhodopsin did not show an influence of moderate pH and temperature changes on the dangling absorption pattern (94). Because of the poor quality of the ChR2-C128T spectrum it is hard to identify minor shifts in comparison to ChR2-C79/C128T/C208. But nevertheless ChR2-C128T and –C79/C128T/C208 show very similar dangling water band positions. ChR2-T159C has as well an unaltered absorption pattern in the water region. The comparison proofs that the substitution of C34, C36, C87, C179, C183 and C256 by alanine as well as T159 by cysteine do not have any effect on the dangling water (Figure 54). Coherent with this finding all these positions are remote to the dangling water position hypothesized by us. Already at 80 K dangling water difference bands are observed (92). In 3.4.4.1.1 (p. 79ff) it was shown that at these cryogenic temperatures no movements of helix B are observed. Most likely structural changes occur only in the direct environment of the isomerized 13-cis retinal. Indeed W223 was suggested on the basis of molecular dynamics simulations to have a steric conflict with the 13-methyl group of retinal after isomerization (5).

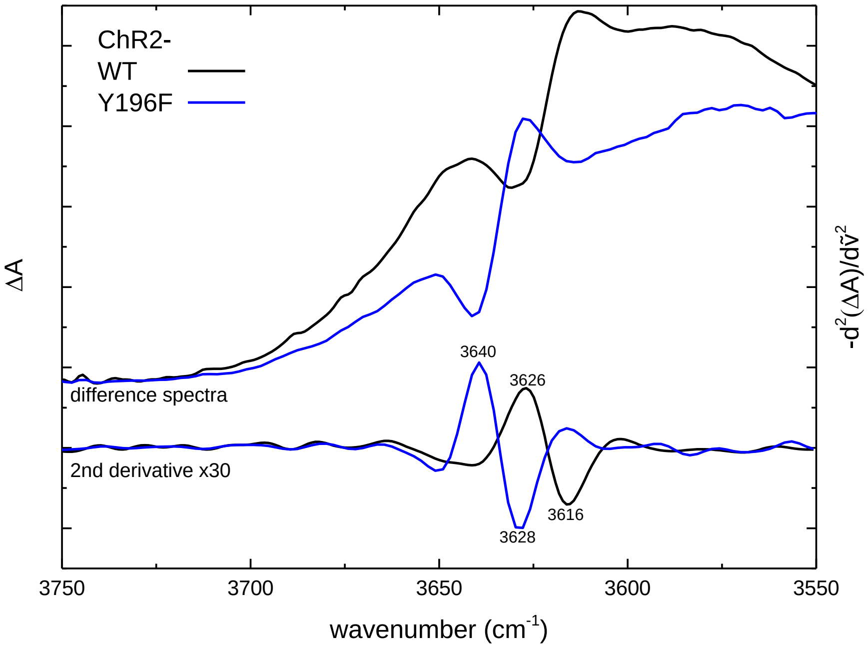

Figure 53: Light-induced FTIR difference spectra (upper part) and the respective second derivative (lower part) of ChR2-Y196F (blue) and –WT (black). The O-H stretching region is compared. For a precise band position the second derivative of the difference spectrum (resolution reduced to 8 cm^{-1}) is displayed. The spectra were recorded under photostationary conditions (456 nm illumination) at 25°C and scaled to the all-trans retinal band at 1246 cm^{-1}:

Table 15: Qunatification of the dangling water difference bands: Band positions in ground state (ChR2^{480}) and (P$_4$^{480}), full width at half maximum (FWHM), area and the weak hydrogen bond length calculated from the band position according to (93). The band parameter are determined by the fit of the second derivative (Figure 53) with the second derivative of lorentzians. The standart deviation was calculated from the noise between 3680 and 3750 cm^{-1}. The “±” value are two standart deviations, thus the 96% confidence interval for each parameter.

	ChR2-	ṽ (cm^{-1})	FWHM	Area (cm^{-1}x1000)	r(H…O) (Å)
ChR2^{48} c	WT	3625.5 ± 0.7	18.7 ± 2.5	-5.4 ± 1.5	2.66
	Y196F	3639.7 ± 0.2	11.1 ± 1.1	-2.8 ± 0.4	2.90
P$_4$^{480}	WT	3615.7 ± 0.8	16.1 ± 3.0	3.2 ± 1.2	2.55
	Y196F	3628.2 ± 0.3	12.9 ± 1.2	3.2 ± 0.5	2.70

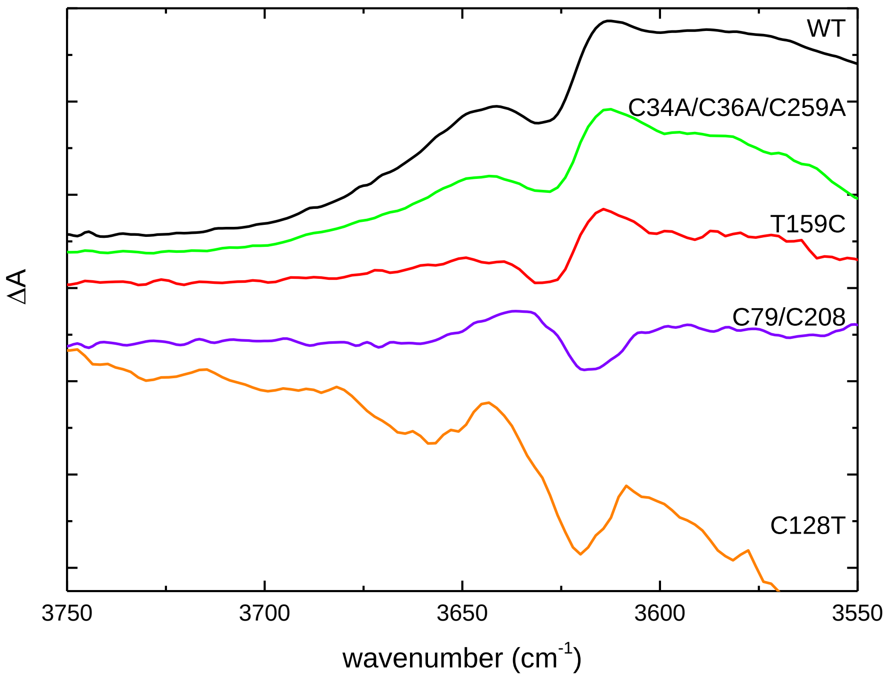

Figure 54: Light-induced FTIR difference spectra of several cysteine variants in comparison to ChR2-WT. The O-H stretching region is compared. The spectra were recorded under photostationary conditions (ChR2-WT, -C34A/C36A/C259A and –T159C at 25°C, pH 7.4, 456 nm illumination; ChR2-C128T and –C79/C128T/C208 at 273 K, pH 6.0, 420 nm illumination) and scaled to the all-trans retinal band at 1246 cm^{-1}.

3.6 The T159C variant: A functional variant with improved expression

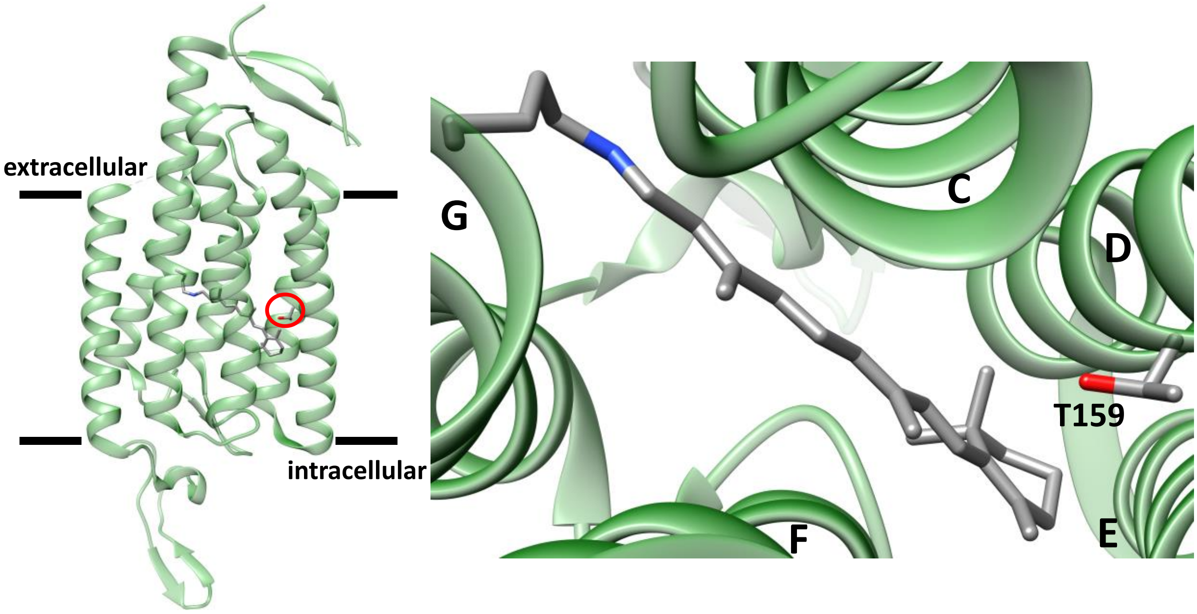

Figure 55: T159 in the C1C2 chimera structure (PDB: 3UG9): T159 is located next to the β-ionone of the retinal chromophore.

Several of the alanine substitutions seem to decrease the expression of functional ChR2, while the C128T substitution enhances expression levels (see 3.1, p. 46, Table 4). It was shown that the T159C substitution can improve the expression of ChR2 in *Xenopus laevis* oocytes, hippocampal pyramidal neurons, and HEK cells (95-97). The enhanced expression was up to now not verified in *Pichia pastoris* and the isolated protein was not biophysically characterized. The preparation of a suitable PELDOR sample consumes large amounts of highly purified ChR2. Thus the available amount of ChR2 is limiting the experimental approach in some cases. For instance DMPC was chosen for the nanodiscs reconstitution instead of POPC because of the much better nanodiscs reconstitution efficiency with DMPC (see 3.4.1.1.2, p. 61). In order to enhance ChR2 expression yields the T159C mutation was expressed, purified and biophysically characterized.

3.6.1 Results

The expression yield in comparison to ChR2-WT could be improved by a factor of 2, thus yielding ~0.6 mg ChR2-T159 per L of cell culture.

Figure 56 shows a flash-photolysis measurement comparing characteristic wavelengths of ChR2-T159C with ChR2-WT. In Table 16 the time constants, fitted to traces recorded in 20 nm steps from 320 nm to 600 nm using 5 exponential functions, are shown. The biphasic formation of P_2^{390} in ChR2-T159C is overall slightly slower than in ChR2-WT: The amplitude of the first fast phase of P_{2a}^{390} (~7 µs) is drastically reduced, while the time constant of the second slow phase (P_{2b}^{390}) is now dominant and slightly faster than in ChR2-WT. The decay of P_3^{530} is slightly delayed, which is in line with photocurrent measurements showing a slower closing of the channel (96).

Figure 57 shows the comparison between the FTIR light-dark difference spectra of ChR2-T159C and –WT dominated by the P_4^{480} intermediate. The spectra are scaled to the C-C all-trans retinal absorption band of ground state ChR2 at 1246 cm^{-1}. The region from 1100 to 1800 cm^{-1}, which features absorption bands of carboxylic acids, of vibrational modes of the amide backbone as well as retinal specific bands, are for the most part superimposable. The only clear difference is the altered intensity of the ethylenic stretch vibrations of all-trans retinal at 1552 cm^{-1} and 1538 cm^{-1}. In ChR2-T159C the vibration mode at 1538 cm^{-1} is more pronounced than in ChR2-WT, indicating the different retinal environment in ground state. The C-C stretch vibrations (~1000 to 1250 cm^{-1}) are not affected. Both argues for a local effect of the T159C substitution on the retinal in the ground state and if any only minor effects on retinal in P_4^{480}. An additional difference is observed in the S-H stretch vibration region (Figure 58). The positive band in ChR2-WT at 2557 cm^{-1} is blue shifted in ChR2-T159C by ~2 cm^{-1} and appears to be more intense. A straight forward explanation might be that an additional band is arising from C159 due to the movement of the retinal. The time resolved UV/Vis measurement shows slightly delayed kinetics for the formation of P_2^{390} and the decay of P_3^{530}. In conclusion also considering the large photocurrents (95,96), ChR2-T159C has comparable functionality as ChR2-WT and is, due to its two-fold expression, well suited to be employed for biophysical studies instead of ChR2-

WT. Additionally the T159C substitution should be tested in the background of the cysteine-reduced variants. Judged from the C1C2 x-ray crystallographic structure T159 is not solvent accessible and thus C159 will most likely not interfere with the labeling of other cysteines.

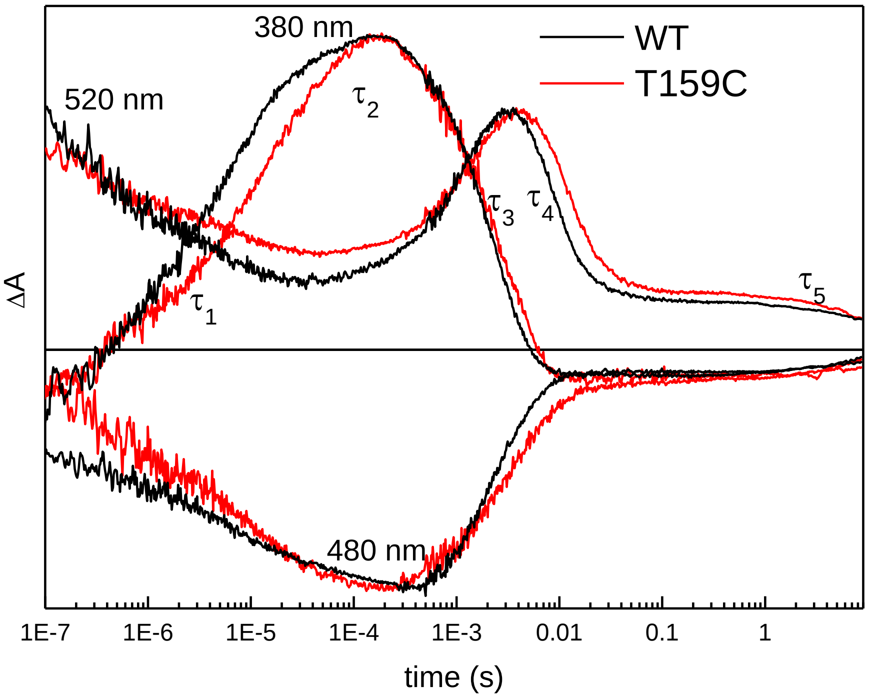

Figure 56: Transient absorption changes after ns laser excitation (450 nm) of ChR2-T159C (red) in comparison to ChR2-WT (black), both variants solubilized in DM. The three traces are characteristic for the four intermediates of the photocycle: At 520 nm P_1^{500} (decay) and P_3^{520} are observed. The trace at 480 nm reports on the P_4^{480} and ground state. 380 nm shows the formation and decay of P_2^{390}. Conditions: 25°C, pH 7.4.

Table 16: Time constants of the decay of the different intermediates from global fit of transient absorption changes after ns laser excitation of ChR2-T159C solubilized in DM. Kinetic traces were recorded between 320 nm and 600 nm and fitted by 5 exponentials. Conditions as in Figure 56.

ChR2-	τ1 P_1^{500} (µs)	τ2 P_{2a}^{390} (µs)	τ3 P_{2b}^{390} (µs)	τ4 P_3^{530} (ms)	τ5 P_4^{480} (s)
WT	7.2	156	1.9	6.5	7.4
T159C	7.4	52	2.3	9.4	11.5

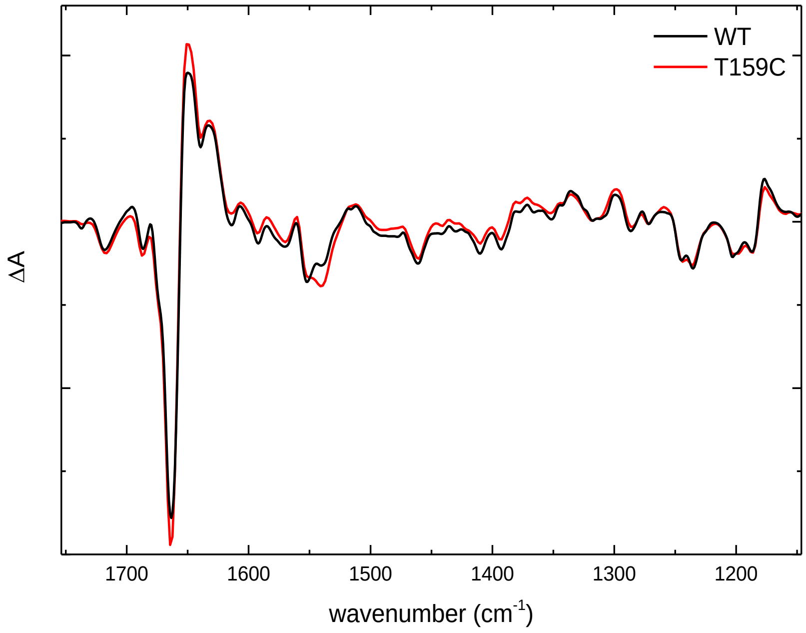

Figure 57: Light-induced FTIR difference spectra of ChR2-T159C (red) and –WT (black). The spectra were recorded under photostationary conditions (456 nm illumination) at 25°C and scaled to the all-trans retinal band at 1246 cm^{-1}. At these conditions P_4^{480} is dominant in the photostationary mixture.

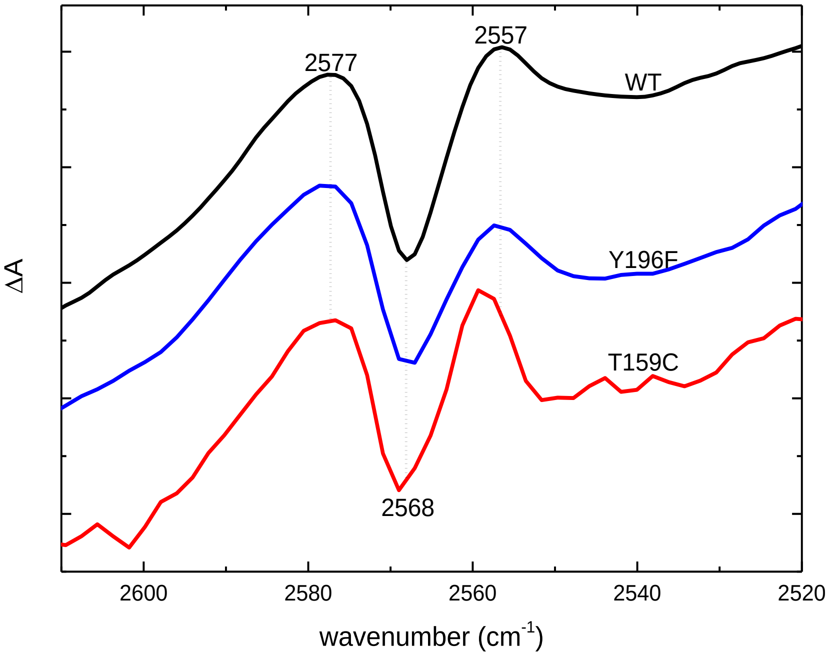

Figure 58: Light-induced FTIR difference spectra of ChR2–WT (black), -Y196F (blue) and –T159C (red). The spectra were recorded under photostationary conditions (456 nm illumination) at 25°C and scaled to the all-trans retinal band at 1246 cm^{-1}.

4 Discussion

4.1 *New cysteine-reduced variants for side directed spin labeling*

The prerequisite for the spin-spin distance studies are cysteine-reduced variants, which are able to accumulate the open state. All accessible cysteines in these variants must be removed apart from the labeling sides. We were successful in substituting all cysteines except of C79, which could not be substituted without abolishing the protein expression. Three variants were produced in sufficient yields and with accessible labeling sides: ChR2-C79/C128T, -C79/C128T/C208 and –C79/C128T/Q117C. In these variants all WT-cysteines aside from the ones stated are substituted by alanine. In consequence 7 to 9 amino acids were substituted in each variant. The C128T substitution that was introduced in each of the variant is known to prolong the conducting state, thus to enable the accumulation of P_3^{530} under continuous illumination (31,33). The variants were characterized by UV/Vis-, FTIR-spectroscopy and electrophysiology. In order to evaluate the functionality the results were compared to ChR2-C128T, which has been investigated in depth with various methods (17,31-33,35,98) and has also been applied in optogenetic studies (34). In the following the functionality will be discussed, first in detergent environment, then in DMPC nanodisc environment, before both environments are compared and related to the potential functional role of the cysteines.

4.1.1.1 Functionality in detergent environment

In detergent the most striking difference between the kinetics of the cysteine-reduced variants and ChR2-C128T (31,33) is the irreversible formation of a photoproduct with absorption around 380 nm in the cysteine reduced variants. Nevertheless the photo stationary state during illumination (Figure 24, p. 55) is virtually identical for MTSL labeled/unlabeled ChR2-C79/C128T and -C79/C128T/C208 when compared to ChR2-C128T. These finding is in line with the electrophysiology measurements. In ChR2-C79/C128T/C208 and ChR2-C79/C128T the photocurrents are not impaired in comparison to ChR2-C128T (section 3.2, p. 47ff). In contrast the cysteine-reduced variants give higher currents compared to ChR2-C128T. Without further studies it cannot be concluded if the increased photocurrents are due to an increased single channel conductance or result from higher expression levels. Consequently, there are no indications for an influence of the cysteine substitutions in the variants nor of the MTSL labeling in the P_3^{530} intermediate.

Some fraction of ChR2-C79/C128T/C208 (Figure 23, p. 53) decays from P_2^{390} directly to the ground state (τ~80 s), which is observed for ChR2-C128T as well (31). Another fraction decays (τ~38 min) on a longer timescale to a photoproduct with an absorption maximum around 380 nm (Figure 22) that does not recover the ground state. ChR2-C128T has two long lived blue-shifted intermediates (P^{380} and P^{353}) (33). Both intermediates represent a branch of the ChR2-C128T photocycle under continuous illumination and were shown by resonance Raman spectroscopy to feature a retinal chromophore with hydrolyzed Schiff base still located in the binding pocket (98). In ChR2-C128T the hydrolysis of the Schiff base is reversible since P^{380} and P^{353} decay to the ground state. In the cysteine-reduced variants somehow this process seems to be irreversible at least for some fraction of the protein population. This fraction increases with increasing pH (Figure 22, p. 51). The spin-spin distance measurements showed a disposition of these variants to form aggregates. Since it was shown that bacteriorhodopsin has an improved thermodynamic stability of 17 kcal/mol with all-trans retinal bound (99), it might well be that the readiness to aggregate originates from the loss of the retinal cofactor. The slow relaxation at 5°C and the low ground state recovery at RT hamper time resolved single turnover measurements that rely on averaging numerous recordings. The impaired photostability also complicates the handling of these variants by posing the necessity to work in darkness or red light. Nevertheless the variants in detergent environment are well suited to characterize P_3^{530} in illuminated, freeze-quenched samples, as in the PELDOR measurements (3.3.3, p. 56ff). Another possibility is to measure during illumination at 5°C on a minute timescale, as in the FTIR-measurements (Figure 24, p. 55).

4.1.1.2 Membrane environment

The handicaps of these variants could be partly overcome by the reconstitution in nanodiscs environment. The reconstitution of ChR2 in DMPC nanodiscs was optimized yielding monodisperse samples (0, p. 66ff) with ChR2 recoveries of up to 63% (0, p. 65ff). In order to be closer to native conditions reconstituting into lipids with longer chains and lower melting point would be desirable. The reconstitution in POPC was tested and gave in our hands drastically reduced yields (3.4.1.1.2, p. 61). This is in line with observations made with nanodisc reconstitution of proteorhodopsin (100). Consequently without having variants that give higher expression yields employing POPC lipids is not feasible. The DMPC nanodisc environment speeds up the ground state recovery and drastically reduces bleaching of ChR2-C79/C128T/C208 compared to the detergent (DM) environment (Figure 36, p. 69). The nanodisc environment enabled to record time resolved single turnover UV/Vis-kinetics (Figure 37, p. 70). The decay kinetics of the different intermediates are similar to ChR2-C128T in detergent environment (Table 10, p. 71).

The FTIR light-dark difference spectra of ChR2-C79/C128T in Figure 59 give a comparison of P_3^{530} in DM solubilized and DMPC nanodisc reconstituted samples. The helix hydration bands (1662 cm^{-1}(-)/1648 cm^{-1}(+)) are clearly larger in detergent environment. After channel opening a smaller helix surface is exposed to water in DMPC nanodisc environment compared to DM. Detergents in general are considered to expose less lateral pressure on the transmembrane region than lipids. Furthermore the acyl chains of DMPC incorporated in nanodiscs have a higher order than liposomes (100). Accordingly nanodiscs have an enhanced lateral pressure compared to liposomes and could allow less conformational freedom to embedded membrane proteins. As a result ChR2 might undergo smaller conformational changes that lead to decrease of the hydrated helix surface (the conformational changes will be discussed in 4.2, p. 106ff). The lower photostability of the cysteine-reduced variants could be a result of the increased helix hydration that replaces helix-helix hydrogen bonds and thereby potentially decreases the structural stability of the open state. Also an increased solvent accessibility of the Schiff base, that favors hydrolysis of the retinal or lowers the retinal affinity, might be a consequence.

4.1.1.3 Cysteine functionality

In nanodiscs ChR2-C128T shows smaller hydration bands than ChR2-C79/C128T (Figure 59, p. 104). In conclusion substituting the majority of cysteines by alanines leads to an open state in which the helices are more solvent exposed. The position of the cysteines C179, C183 and C259 are facing the hydrophobic lipid environment of the transmembrane region. They are surrounded by hydrophobic residues and are not conserved in many channelrhodopsins (88). Thus these residues might not fulfill a specific functional role in the photocycle, but rather have less specific importance on the level of translation, folding or membrane insertion. In line with this assumption C259 can be substituted by other bulky residues like methionine, leucine or threonine without any effect on the amplitude of photocurrents, while the substitution with alanine yielded only 20% of the photocurrents ((101) referring to mutations in the background of a WT-behaving C34S/C36S-variant). Figure 18A (p. 45) shows that C259 has basically no influence on the vibrational bands of P_4^{480} and therefore no major impact on P_4^{480}. Nevertheless C259 has an impact on the difference bands in the S-H stretching region (2568 cm^{-1}(-), Figure 18B), indicating that it experiences alterations, like different hydrogen bonding, in P_4^{480} compared to ground state. C179/C183 could be substituted by other hydrophobic residues like alanine or leucine retaining 65 or 80% of photocurrent amplitudes (101).

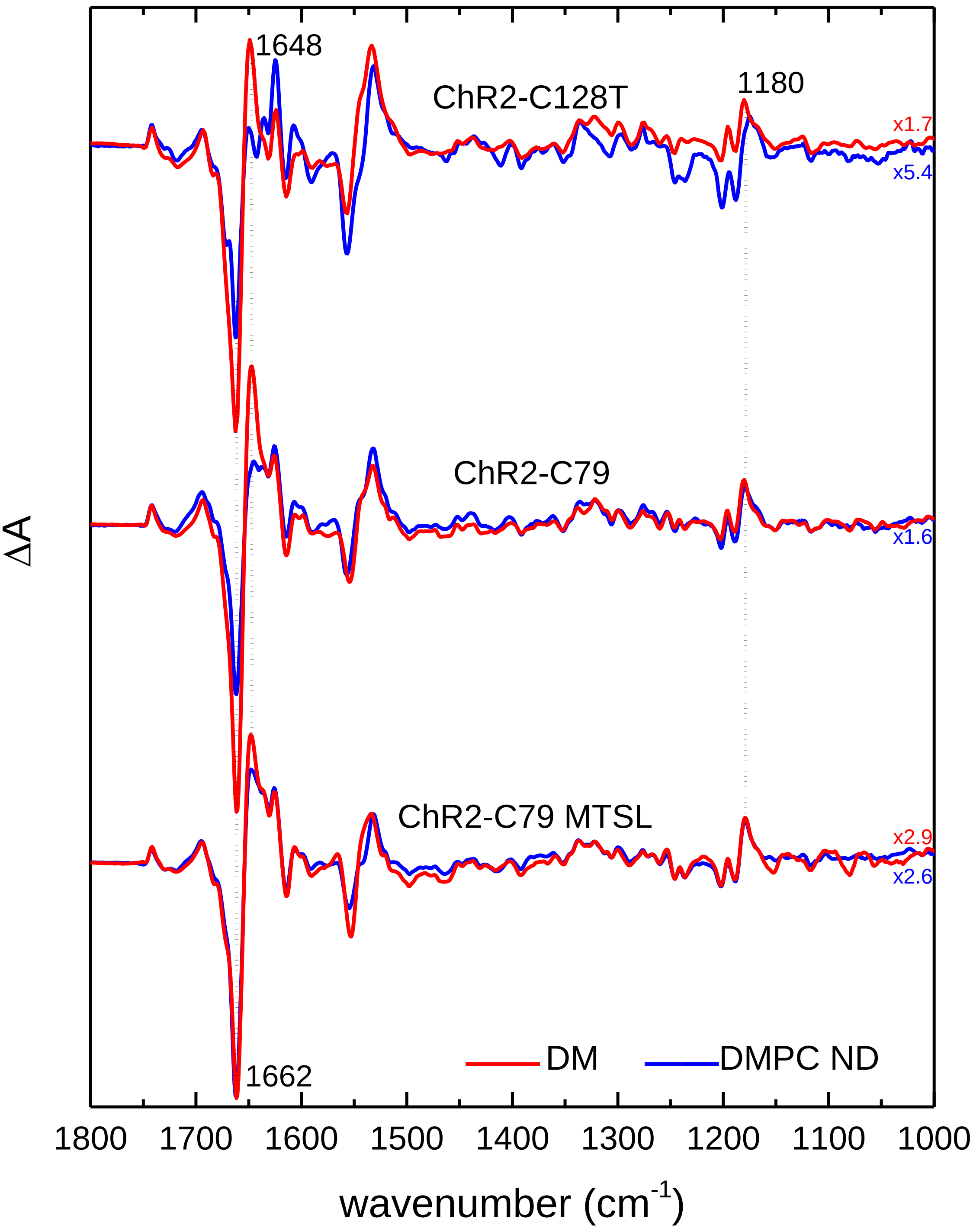

Figure 59: Light-induced FTIR difference spectra of ChR2 variants C128T (top), ChR2-C79/C128T unlabeled (middle), and ChR2-C79/C128T unlabeled (bottom) in detergent (DM, red lines) and reconstituted to DMPC ND (blue lines), respectively. The spectra were recorded under photostationary conditions (after 20 s illumination at 420 nm, averaged 80 s) at 278 K. The spectra are scaled to the all-trans retinal band at 1180 cm^{-1}.

C34 and C36 are located in a soluble N-terminal β-sheet domain and were shown in the x-ray crystal structure to bridge the monomers within the dimer (7). The substitution by alanine gives about the same stationary photocurrents in oocytes as WT (90) in contrast the substitution by serine gives a 2.5 fold increase (102). The functional role of the disulfide bridges in ChR2-WT dimer seems not to be crucial, especially since the spin-spin distance measurements show a dimeric protein (3.4.4.1, p. 77ff). Indeed also a study employing circular dichroism (CD)-spectroscopy and electrophysiology proved that ChR2 is also without the N-terminus still dimeric and shows photocurrents similar to the construct including the N-terminus (103).

C87 is located on helix B facing in between helices A and G, a region where the prolongation of the pore towards the intracellular side is expected. The substitution by serine lowers stationary photocurrents in oocytes to about one third of ChR2-WT, reduces the permeability for larger cations, but does not alter the kinetics of channel opening and closing (104). In Figure 18B (p. 45) it seems to contribute solely to a positive band at 2557 cm^{-1} therefore experiences hydrogen bonding or electrostatic changes between P_4^{480} and ground state. To assign the 2557 cm^{-1} in the single mutation variant and subsequently trace the kinetics of this band might give interesting insights the hydration dynamics during channel opening. C87 is probably the most likely candidate to have substantial impact on the helix hydration in P_3^{530}.

C79 and C208 are conserved in many ChRs. Substituting C79 or C208 reduces the expression yields and photocurrents (Table 4, p. 46 and (101,102)). Again it is not clear on which level (e.g. translation, folding, membrane insertion or thermodynamic protein stability) the substitution of these cysteines reduces the expression yields. Comparing ChR2-C79/C128T/C208 and –C79/C128T, the substitution of C208 to alanine does not have any severe impact on the FTIR difference spectra (P_3^{530}). As well the photocurrents show similar kinetics and amplitudes (3.2, p. 47ff). Therefore a crucial functional role of both residues seems to be unlikely.

Probably the reduced expression of these variants can be compensated by introducing mutations that are known to enhance expression, like substituting C34 and C36 by serine, T159 by cysteine or C259 by leucine. Additionally the T159C substitution was shown to improve the retinal affinity in the ChR2-WT background and photocurrents in various mutational backgrounds (96,97). Improving the retinal affinity might also have beneficial effects on the photostability.

4.2 Helical movements

In detergent environment qualitatively an outward movement of helices B and F could be shown (Figure 25, p. 56). In ChR2-C79/C128T the helix B-B distance is overlain by a broad background (Figure 25, p. 56, top row), which we attribute to aggregated protein as discussed above. Apart from the distance background, the illuminated ChR2-C79/C128T sample (Figure 25, p. 56, top row, green trace) shows a much less defined distance than the dark-equilibrated sample (black trace). This suggests a more heterogeneous distance between the B-helices in the illuminated sample. Figure 23 B) shows in addition to the predominant P_3^{530} also minor contributions of P_2^{390} and ground state/P_4^{480}. Consequently a fraction of intermediates other than P_3^{530} is sampled as well and might contribute with different helix B-B distances. Therefore the distance changes are not straight forward to quantify. To get a more quantitative picture of the distances the dimers were trapped in their oligomerization state in nanodiscs and the illumination conditions were optimized towards maximal accumulation of P_3^{530}. Thereby the background could be eliminated and a narrower distance distributions for the illuminated samples was yielded.

Another uncertainty of interpretation arises from the distance measurement between the monomers. The cysteines C34 and C36 that covalently link the monomers within the dimer in ChR2-WT are replaced in the cysteine-reduced variants. Therefore the ChR2-Q117C/C128T variant was designed. The label at Q117C located in helix C is part of the dimer-interface close to the extracellular side. The PELDOR measurements of ChR2-Q117C/C128T show that upon illumination the C-C helix distance stays exactly the same (Figure 49, p. 88). This suggests a solid dimer-interface also upon channel opening. Consequently the observed distance changes of the other labeling sides can be interpreted in terms of local or helix displacements. The PELDOR measurements of ChR2-C79/C128T exhibit pH dependent different label distances at helix B in ground state (Figure 42, p. 77). At pH 7.4 the distance distribution is more heterogeneous than at pH 6.0. Since cysteine bound MTSL has a pKa out of the physiological range (105) the altered distribution is most likely the result of a pH dependent conformational change of the protein. Recently time-resolved fluorescence anisotropy measurements were conducted by AG Alexiev on the ChR2-C79/C128T/C208 variant selectively labeled with a fluorescence dye at C79 (89). The measurements showed at pH 6.0 lower conformational space of the cytoplasmic part of helix B compared to pH 7.4. In consequence the pH dependence of the PELDOR distance distribution arises indeed from conformational alterations of the protein and not only dynamics of the spin label itself. The two C1C2 crystal structures published can give a hint for the cause of the pH dependence of the conformational space. One x-ray crystal structure of the C1C2 chimera was solved at pH 6.0 (7). A blue shifted C1C2-variant with two amino acid substitutions (corresponding amino acids in ChR2: T159G/G163A) in close proximity to the β-ionone ring of the retinal was crystalized at pH 7.0 and the structure was solved (30). The C1C2 ChR structures at pH 6.0 and 7.0 resolve different protonation states for 4 amino acids of which 3 are located in the N-terminus. The only structural difference observed in the transmembrane part (apart from the amino acid substitutions) is glutamate 83 (E83), which is located on the intracellular part of helix C close to C79. E83 is in the protonated state at pH 6.0 hydrogen bonded to H134 (helix F), while deprotonated it forms a salt bridge with R268 (helix G). PROPKA approximates for E83 a pKa of 5.4 in the C1C2 structure (30), which might be higher for ChR2. Thus protonation of E83 at pH 6.0 in ChR2 and consequently hydrogen bonding to H134 might lead to the homogenous loop/helix conformation observed in the PELDOR measurements. The functional relevance of this pH dependence of the inner gate needs to be clarified in future studies.

In early P_1^{500} (at 80 and 120 K) helix B does not move (see 3.4.4.1.1, p. 79ff.). Although already on the ps timescale and at 80 K substantial amide-I difference bands were observed (24) and recent MD studies suggest the prolongation of the hydrophilic funnel to the cytosolic side during P_1^{500} (5,6). Both studies agree on the hydrogen bond between glutamate 90 (E90) and asparagine 258 (N258) and a salt bridge between glutamate 83 (E83) and arginine 268 (R268) as major constriction sides that prevent a pore prolongation to the intracellular side in ground state (Figure 4). The authors substituted the all-trans retinal in the respective structure by 13-cis isomerized retinal. One of the two studies used a ChR2 homology model based on the C1C2 x-ray structure (6). The simulation shows a strain on the lysine (K257) to which the 13-cis retinal is bound via the Schiff base. The strain is propagated to R268 and causes a weakening of the hydrogen bond to E90. The deprotonated E90 forms a salt bridge to arginine 93 and the cytosolic part of helix B tilts outwards. However, E90 is most likely only deprotonated during P_4^{480} (19), the first larger hydration events of the protein interior take place in P_2^{390} (8) and in this work it was shown that helix B does not move at cryogenic temperature up to 120 K (3.4.4.1.1, p. 79ff) thus in early P_1^{500}. The second simulation on the C1C2 x-ray structure (5) identified a steric conflict of the 13 methyl group of the isomerized retinal with tryptophan 223 (W223), that leads to the movement of the cytoplasmic half of helix F. The suggested distortion of the W223 side chain in early P_1^{500} would be in line with the observed dangling water difference bands at cryogenic temperature (92) and our hypothesized location of the dangling water being hydrogen bonded to W223 (3.5, p. 89ff). Therefore kinetics of the dangling water difference band might yield valuable information on the dynamics of early helix F movements. The movement of helix B and thereby the pore formation between helices A, B, C and G suggested in both works is strongly supported by the large helix B outward movement shown in this work.

Our measurements investigating different illumination conditions suggest an identical helix B-B distance in P_3^{530} and P_4^{480} (3.4.4.1.2, p. 80ff.). The latter finding is in line with the PELDOR data published by Sattig at al. (102) using a variant accumulating P_4^{480} (Table 17). Figure 60 shows a comparison of our distance

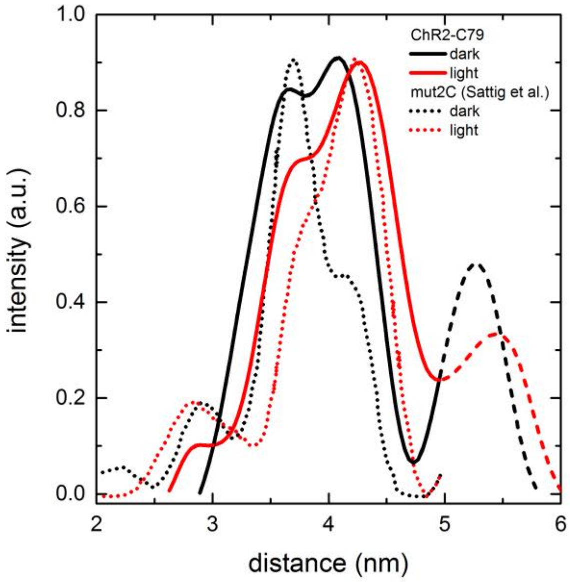

Figure 60: PELDOR distance distribution for the ChR2-C79/C128T in DMPC nanodiscs (solid lines) and "Mut-2C"-variant solubilized in DM (dotted lines) from Sattig at al. (102) labeled as well at C79. The distance distribution for the dark-equilibrated (black lines) ChR2 and the illuminated ChR2 (red lines). ChR2-C79/C128T is accumulating P_3^{530} while the "mut2C"-variant accumulates P_4^{480} under continuous illumination.

Table 17: Amino acid substitutions in ChR2-C79/C128T and "Mut-2C"-variant from Sattig at al. (102) in comparison to ChR2-WT. First row indicates the sequence position (#AA), the following rows indicate the amino acid (C: cysteine, S: serine, L: leucine, A: alanine, T: threonine) at the respective sequence position in the different variant.

AA#	34	36	79	87	**128**	179	183	208	259
ChR2-WT	C	C	C	C	**C**	C	C	C	C
Mut-2C	S	S	C	S	**C**	L	L	A	L
ChR2-C79	A	A	C	A	**T**	A	A	A	A

distribution data (ChR2-C79/C128T in DMPC nanodiscs, pH 7.4) and the data of Sattig at al. recorded at pH 7.4 with a DM solubilized sample. In their publication Sattig at al. investigated a variant featuring C128. For most other cysteines different substitutions (Table 17) were used. The variant showed ChR2-WT like kinetics, therefore it can be assumed that P_4^{480} is accumulated under continuous illumination. In the ground state (Figure 60, "dark" black traces) as well as in P_3^{530}/P_4^{480} ("light", red traces), the maxima of the distributions are virtually the same. This finding is interesting not only because the illuminated samples represent different intermediates, but also because the nanodisc membrane and detergent environment give the same helix B movement. This suggests a very robust mode of movement for helix B, which displacement persists also during P_4^{480}. It also strengthens the idea of gating consisting of two steps: 1. the major conformational changes prolonging the pore to the intracellular side between helices A, B, C and G 2. the opening of a last constriction site within the pore that enables cation flow.

A helix B movement was suggested also from electron microscopy studies of 2D-crystals of bacteriorhodopsin (106,107) and ChR2-C128T (108). In ChR2-C128T the EM data does not reveal a direction of movement of helix B and was interpreted as loss of helical order. A helix B movement was not observed in visual rhodopsin (109,110), where the helix F movement seems to be the functional relevant event (111). In this work the movement of helix F of ChR2-C79/C128T/C208 was qualitatively shown in detergent environment. The long F-F helix distance is difficult to resolve (long modulation frequencies) and could not be determined in nanodiscs up to now (Figure 47, p. 85), but is still ongoing work. Nevertheless differences in the region of the B-F helix distance were observed, where a subpopulation moves to smaller distance upon channel opening. A cryo electron microscopy study of illuminated ChR2-C128T 2D crystals (108) showed an outward movement of helix F away from helix B. An outward movement of the cytoplasmic side of helix F was as well observed for bacteriorhodopsin (112), sensory rhodopsin II (66,113) and visual rhodopsin (109,110). Therefore an inward movement of helix F seems unlikely and the distance change might rather correspond to certain label and loop conformational dynamics in a subpopulation.

The helix F movement seems to be a general feature of rhodopsins. The mechanism of the helix F displacement still needs to be elucidated.

5 Conclusion

In this work three functional ChR2 cysteine-variants were engineered to enable the site specific labeling end of helix B and additionally helix F or C. The labeling positions can be investigated in the ground state and in the accumulated open state, P_3^{530}. The variants were spin-labeled and subjected to pulsed electron double resonance (PELDOR) measurements. Thereby an outward displacement of the cytosolic side of helix B and F in the open state could be observed. The helix B displacement persist also in the desensitized state, P_4^{480}. These results strengthen the hypothesis of a prolongation of the pore between helices A, B, C and G (5-7) by the observed outward movement of helix B in the open state. However, as suggested earlier (8,9), the major structural changes are to some extent decoupled from the on-gating, since the outward displacement of helix B persists in the desensitized state. Furthermore we set the stage for the quantitative determination of the helix F movement, which is currently underway.

The results of this thesis will help to guide the development and benchmark future open state models.

6 Outlook

The narrow distance distributions in the PELDOR measurements of ChR-C79/C128T could allow to systematically investigate the cooperativity of retinal loss and helix B movement. Concerning the elucidation of a potential cooperativity of retinal loss one approach could be the following. First one batch of nanodisc reconstituted ChR2-C79/C128T (typically ~20% of bleached protein molecules (3.4.1.3.1, p. 70ff)) is divided into several samples and subjected to continuous illumination of different time intervals. The different illumination duration will result in different fractions of bleached ChR2 in the sample. After recovery of the ground state of the remaining intact ChR2 the identical optimized illumination protocol (as applied to the nanodisc samples in 3.4.4, p. 77ff) will be applied to each sample in order to get maximal P_3^{530} accumulation. The interrelationship between the fraction of bleached ChR2 and the intensity of the distance population residing at ground state distance (~3.8 nm) can clarify potential cooperativity of retinal binding within the monomers. For bacteriorhodopsin cooperative retinal binding was shown (85).

The cooperativity of the helix B movement could be clarified by using different illumination conditions for the freeze quenching protocol. Exposing ChR2-C79/C128T to different light intensities and illumination durations will yield different fractions of P_3^{530} in the freeze quenched samples. For example at 50% ground state and 50% P_3^{530} in case of a strong positive cooperativity the distance distribution should show only the ground state distance (~3.8 nm) and the 7 Å shifted illuminated peak both of same intensity. In case of no cooperativity helix B in both monomers would be statistically displaced after illumination therefore having in 25% of the dimers both helices B displaced, in 25% no helical movement and in 50% one helix per dimer moved. Consequently both scenarios should be clearly distinguishable. Positive cooperativity of opening was shown for other homodimeric channels, that feature one pore per monomer, as CLC (e.g. (114)) or the voltage gated H^+-channel Hv1 (115). Cooperativity could be also important for the desensitization and light adaption of ChR2, thus cooperative effects on the thermal relaxation could play a role. Knowledge about the level of cooperativity will make clear if we can consider the monomers within the dimer as completely symmetrical or if we have to take a mixture of different states into account. Therefore it will help to interpret the distance shifts upon channel opening more precisely. The same holds true for the pH induced structural heterogeneity (3.4.4.1, p. 77ff). Experiments on the functional relevance of the observed differences between pH 6.0 and 7.4 might also shed light on E83 as major constriction side (see 4.2).

The measurements on ChR2-C79/C128T/C208 are still ongoing in order to quantify the helix F-F distance changes upon channel opening. The results will help to guide and benchmark *in-silico* simulations of the channel opening.

The same variants employed for spin labeling can be also subjected to complementary methods. Fluorescence labeling, anisotropy and label accessibility measurements have already been performed to some extent (89). The results show different fluorescence label accessibility at C79 between ground state and the illuminated sample. Therefore also stark probes attached to C79 might give difference signals.

The FTIR band of the dangling water was assigned to a water in the crystal structure of C1C2. As well C87 was assigned to a FTIR difference band in P_4^{500} (+2557 cm^{-1}). The assignments are tentatively but might give the framework for FTIR spectroscopic studies of helix F (dangling water) and B (C87).

The approach to introduce cysteines in ChR2-C79/C128T in order to determine additional distances has several limitations. First of all the inter-monomer distance of the additional introduced label needs to be >4 nm or a very short distance <3 nm to be distinguishable from the C79-C79 distance. Further on the labeling position needs to be label accessible and the engineered variant needs to express in sufficient amounts. Therefore the expression should be improved. Most promising is the T159C substitution to improve expression yields and photostability. Also substituting C259 by leucine, C34/C36 by serine instead of alanines seems to be promising (as discussed in 4.1.1.3, p. 103ff). The improvement of expression might also enable to reintroduce

C128 in order to yield a ChR2-WT like photocycle, which would ease time resolved studies tremendously.

References

1. Hou, S. Y., Govorunova, E. G., Ntefidou, M., Lane, C. E., Spudich, E. N., Sineshchekov, O. A., and Spudich, J. L. (2012) Diversity of Chlamydomonas channelrhodopsins. *Photochemistry and photobiology* **88**, 119-128
2. Zhang, F., Vierock, J., Yizhar, O., Fenno, L. E., Tsunoda, S., Kianianmomeni, A., Prigge, M., Berndt, A., Cushman, J., Polle, J., Magnuson, J., Hegemann, P., and Deisseroth, K. (2011) The microbial opsin family of optogenetic tools. *Cell* **147**, 1446-1457
3. Nagel, G., Ollig, D., Fuhrmann, M., Kateriya, S., Musti, A. M., Bamberg, E., and Hegemann, P. (2002) Channelrhodopsin-1: a light-gated proton channel in green algae. *Science* **296**, 2395-2398
4. Fenno, L., Yizhar, O., and Deisseroth, K. (2011) The development and application of optogenetics. *Annual review of neuroscience* **34**, 389-412
5. Takemoto, M., Kato, H. E., Koyama, M., Ito, J., Kamiya, M., Hayashi, S., Maturana, A. D., Deisseroth, K., Ishitani, R., and Nureki, O. (2015) Molecular Dynamics of Channelrhodopsin at the Early Stages of Channel Opening. *PloS one* **10**, e0131094
6. Kuhne, J., Eisenhauer, K., Ritter, E., Hegemann, P., Gerwert, K., and Bartl, F. (2015) Early formation of the ion-conducting pore in channelrhodopsin-2. *Angewandte Chemie* **54**, 4953-4957
7. Kato, H. E., Zhang, F., Yizhar, O., Ramakrishnan, C., Nishizawa, T., Hirata, K., Ito, J., Aita, Y., Tsukazaki, T., Hayashi, S., Hegemann, P., Maturana, A. D., Ishitani, R., Deisseroth, K., and Nureki, O. (2012) Crystal structure of the channelrhodopsin light-gated cation channel. *Nature* **482**, 369-374
8. Lorenz-Fonfria, V. A., Bamann, C., Resler, T., Schlesinger, R., Bamberg, E., and Heberle, J. (2015) Temporal evolution of helix hydration in a light-gated ion channel correlates with ion conductance. *Proceedings of the National Academy of Sciences of the United States of America* **112**, E5796-5804
9. Radu, I., Bamann, C., Nack, M., Nagel, G., Bamberg, E., and Heberle, J. (2009) Conformational changes of channelrhodopsin-2. *Journal of the American Chemical Society* **131**, 7313-7319
10. Packer, A. M., Roska, B., and Hausser, M. (2013) Targeting neurons and photons for optogenetics. *Nature neuroscience* **16**, 805-815
11. Oesterhelt, D. (1998) The structure and mechanism of the family of retinal proteins from halophilic archaea. *Current opinion in structural biology* **8**, 489-500
12. Spudich, J. L., and Luecke, H. (2002) Sensory rhodopsin II: functional insights from structure. *Current opinion in structural biology* **12**, 540-546
13. Moukhametzianov, R., Klare, J. P., Efremov, R., Baeken, C., Goppner, A., Labahn, J., Engelhard, M., Buldt, G., and Gordeliy, V. I. (2006) Development of the signal in sensory rhodopsin and its transfer to the cognate transducer. *Nature* **440**, 115-119
14. Crane, B. R., and Young, M. W. (2014) Interactive features of proteins composing eukaryotic circadian clocks. *Annual review of biochemistry* **83**, 191-219
15. Strotmann, R., Schrock, K., Boselt, I., Staubert, C., Russ, A., and Schoneberg, T. (2011) Evolution of GPCR: change and continuity. *Molecular and cellular endocrinology* **331**, 170-178
16. Kateriya, S., Nagel, G., Bamberg, E., and Hegemann, P. (2004) "Vision" in single-celled algae. *News in physiological sciences : an international journal of physiology*

produced jointly by the International Union of Physiological Sciences and the American Physiological Society **19**, 133-137

17. Muller, M., Bamann, C., Bamberg, E., and Kuhlbrandt, W. (2011) Projection structure of channelrhodopsin-2 at 6 A resolution by electron crystallography. *Journal of molecular biology* **414**, 86-95
18. Lorenz-Fonfria, V. A., and Heberle, J. (2014) Channelrhodopsin unchained: structure and mechanism of a light-gated cation channel. *Biochimica et biophysica acta* **1837**, 626-642
19. Lorenz-Fonfria, V. A., Resler, T., Krause, N., Nack, M., Gossing, M., Fischer von Mollard, G., Bamann, C., Bamberg, E., Schlesinger, R., and Heberle, J. (2013) Transient protonation changes in channelrhodopsin-2 and their relevance to channel gating. *Proceedings of the National Academy of Sciences of the United States of America* **110**, E1273-1281
20. Nack, M., Radu, I., Bamann, C., Bamberg, E., and Heberle, J. (2009) The retinal structure of channelrhodopsin-2 assessed by resonance Raman spectroscopy. *FEBS letters* **583**, 3676-3680
21. Becker-Baldus, J., Bamann, C., Saxena, K., Gustmann, H., Brown, L. J., Brown, R. C., Reiter, C., Bamberg, E., Wachtveitl, J., Schwalbe, H., and Glaubitz, C. (2015) Enlightening the photoactive site of channelrhodopsin-2 by DNP-enhanced solid-state NMR spectroscopy. *Proceedings of the National Academy of Sciences of the United States of America* **112**, 9896-9901
22. Bruun, S., Stoeppler, D., Keidel, A., Kuhlmann, U., Luck, M., Diehl, A., Geiger, M. A., Woodmansee, D., Trauner, D., Hegemann, P., Oschkinat, H., Hildebrandt, P., and Stehfest, K. (2015) Light-Dark Adaptation of Channelrhodopsin Involves Photoconversion between the all-trans and 13-cis Retinal Isomers. *Biochemistry* **54**, 5389-5400
23. Lorenz-Fonfria, V. A., Schultz, B. J., Resler, T., Schlesinger, R., Bamann, C., Bamberg, E., and Heberle, J. (2015) Pre-gating conformational changes in the ChETA variant of channelrhodopsin-2 monitored by nanosecond IR spectroscopy. *Journal of the American Chemical Society* **137**, 1850-1861
24. Neumann-Verhoefen, M. K., Neumann, K., Bamann, C., Radu, I., Heberle, J., Bamberg, E., and Wachtveitl, J. (2013) Ultrafast infrared spectroscopy on channelrhodopsin-2 reveals efficient energy transfer from the retinal chromophore to the protein. *Journal of the American Chemical Society* **135**, 6968-6976
25. Bamann, C., Kirsch, T., Nagel, G., and Bamberg, E. (2008) Spectral characteristics of the photocycle of channelrhodopsin-2 and its implication for channel function. *Journal of molecular biology* **375**, 686-694
26. Schneider, F., Grimm, C., and Hegemann, P. (2015) Biophysics of Channelrhodopsin. *Annual review of biophysics* **44**, 167-186
27. Ernst, O. P., Sanchez Murcia, P. A., Daldrop, P., Tsunoda, S. P., Kateriya, S., and Hegemann, P. (2008) Photoactivation of channelrhodopsin. *The Journal of biological chemistry* **283**, 1637-1643
28. Gadsby, D. C. (2009) Ion channels versus ion pumps: the principal difference, in principle. *Nature reviews. Molecular cell biology* **10**, 344-352
29. Nagel, G., Szellas, T., Huhn, W., Kateriya, S., Adeishvili, N., Berthold, P., Ollig, D., Hegemann, P., and Bamberg, E. (2003) Channelrhodopsin-2, a directly light-gated cation-selective membrane channel. *Proceedings of the National Academy of Sciences of the United States of America* **100**, 13940-13945

30. Kato, H. E., Kamiya, M., Sugo, S., Ito, J., Taniguchi, R., Orito, A., Hirata, K., Inutsuka, A., Yamanaka, A., Maturana, A. D., Ishitani, R., Sudo, Y., Hayashi, S., and Nureki, O. (2015) Atomistic design of microbial opsin-based blue-shifted optogenetics tools. *Nature communications* **6**, 7177
31. Bamann, C., Gueta, R., Kleinlogel, S., Nagel, G., and Bamberg, E. (2010) Structural guidance of the photocycle of channelrhodopsin-2 by an interhelical hydrogen bond. *Biochemistry* **49**, 267-278
32. Nack, M., Radu, I., Gossing, M., Bamann, C., Bamberg, E., von Mollard, G. F., and Heberle, J. (2010) The DC gate in Channelrhodopsin-2: crucial hydrogen bonding interaction between C128 and D156. *Photochemical & photobiological sciences : Official journal of the European Photochemistry Association and the European Society for Photobiology* **9**, 194-198
33. Stehfest, K., Ritter, E., Berndt, A., Bartl, F., and Hegemann, P. (2010) The branched photocycle of the slow-cycling channelrhodopsin-2 mutant C128T. *Journal of molecular biology* **398**, 690-702
34. Berndt, A., Yizhar, O., Gunaydin, L. A., Hegemann, P., and Deisseroth, K. (2009) Bi-stable neural state switches. *Nature neuroscience* **12**, 229-234
35. Ritter, E., Piwowarski, P., Hegemann, P., and Bartl, F. J. (2013) Light-dark adaptation of channelrhodopsin C128T mutant. *The Journal of biological chemistry* **288**, 10451-10458
36. McHaourab, Hassane S., Steed, P. R., and Kazmier, K. (2011) Toward the Fourth Dimension of Membrane Protein Structure: Insight into Dynamics from Spin-Labeling EPR Spectroscopy. *Structure* **19**, 1549-1561
37. Bill, R. M., Henderson, P. J., Iwata, S., Kunji, E. R., Michel, H., Neutze, R., Newstead, S., Poolman, B., Tate, C. G., and Vogel, H. (2011) Overcoming barriers to membrane protein structure determination. *Nature biotechnology* **29**, 335-340
38. Hedfalk, K. (2013) Further advances in the production of membrane proteins in Pichia pastoris. *Bioengineered* **4**, 363-367
39. Andre, N., Cherouati, N., Prual, C., Steffan, T., Zeder-Lutz, G., Magnin, T., Pattus, F., Michel, H., Wagner, R., and Reinhart, C. (2006) Enhancing functional production of G protein-coupled receptors in Pichia pastoris to levels required for structural studies via a single expression screen. *Protein science : a publication of the Protein Society* **15**, 1115-1126
40. Kirsch, T. (2007) Funktionelle Expression von Channelrhodopsin 2 (ChR2) in der methylotrophen Hefe Pichia pastoris und biophysikalische Charakterisierung. *Dissertation, Fachbereich Chemische und Pharmazeutische Wissenschaften der Johann Wolfgang Goethe-Universität in Frankfurt am Main*
41. Ahmad, M., Hirz, M., Pichler, H., and Schwab, H. (2014) Protein expression in Pichia pastoris: recent achievements and perspectives for heterologous protein production. *Applied microbiology and biotechnology* **98**, 5301-5317
42. invitrogen^{TM}. (2010) pPIC9K: A *Pichia* Vector for Multicopy Integration and Secreted Expression. *User Manual*
43. Byrne, B. (2015) Pichia pastoris as an expression host for membrane protein structural biology. *Current opinion in structural biology* **32C**, 9-17
44. Romanos, M. A., Scorer, C. A., and Clare, J. J. (1992) Foreign gene expression in yeast: a review. *Yeast* **8**, 423-488

45. Weiss, H. M., Haase, W., Michel, H., and Reilander, H. (1995) Expression of functional mouse 5-HT5A serotonin receptor in the methylotrophic yeast Pichia pastoris: pharmacological characterization and localization. *FEBS letters* **377**, 451-456
46. Talmont, F., Sidobre, S., Demange, P., Milon, A., and Emorine, L. J. (1996) Expression and pharmacological characterization of the human mu-opioid receptor in the methylotrophic yeast Pichia pastoris. *FEBS letters* **394**, 268-272
47. Tschopp, J. F., Brust, P. F., Cregg, J. M., Stillman, C. A., and Gingeras, T. R. (1987) Expression of the lacZ gene from two methanol-regulated promoters in Pichia pastoris. *Nucleic acids research* **15**, 3859-3876
48. Bornert, O., Alkhalfioui, F., Logez, C., and Wagner, R. (2012) Overexpression of membrane proteins using Pichia pastoris. *Current protocols in protein science / editorial board, John E. Coligan ... [et al.]* **Chapter 29**, Unit 29 22
49. Romanos, M. (1995) Advances in the use of Pichia pastoris for high-level gene expression. *Current Opinion in Biotechnology* **6**, 527-533
50. Looke, M., Kristjuhan, K., and Kristjuhan, A. (2011) Extraction of genomic DNA from yeasts for PCR-based applications. *BioTechniques* **50**, 325-328
51. Baneyx, F. (1999) Recombinant protein expression in Escherichia coli. *Current Opinion in Biotechnology* **10**, 411-421
52. Bayburt, T. H., Grinkova, Y. V., and Sligar, S. G. (2002) Self-Assembly of Discoidal Phospholipid Bilayer Nanoparticles with Membrane Scaffold Proteins. *Nano Letters* **2**, 853-856
53. Sligar Lab, U. o. I. a. U.-C. (2008) Protocols for Preparation of Nanodiscs.
54. Atkins, P. W., and De Paula, J. (2006) *Atkins' physical chemistry*, 8. ed., Oxford Univ. Press, Oxford u.a.
55. Fasman, G. D., and Chemical Rubber Company (Cleveland Ohio). *CRC handbook of biochemistry and molecular biology*, CRC Press, Cleveland, Ohio
56. Herres, W., and Gronholz, J. (1985) Understanding FT-IR Data Processing; Part 1: Data Acquisition and Fourier Transform. *Instruments & Computers*
57. Barth, A. (2007) Infrared spectroscopy of proteins. *Biochimica et biophysica acta* **1767**, 1073-1101
58. Altenbach, C., Marti, T., Khorana, H. G., and Hubbell, W. L. (1990) Transmembrane protein structure: spin labeling of bacteriorhodopsin mutants. *Science* **248**, 1088-1092
59. Milov, A. D., Salikhov, K. M., and Shchirov, M. D. (1981) Use of the double resonance in electron spin echo method for the study of paramagnetic center spatial distribution in solids. *Fizika Tverdogo Tela* **23**, 975-982
60. Bersohn, M., and Baird, J. C. (1967) *An introduction to electron paramagnetic resonance*, Printing with corr. ed., Benjamin, New York, NY u.a.
61. Jeschke, G. (2012) DEER distance measurements on proteins. *Annual review of physical chemistry* **63**, 419-446
62. Klug, C. S., and Feix, J. B. (2008) Methods and applications of site-directed spin labeling EPR spectroscopy. *Methods in cell biology* **84**, 617-658
63. Jeschke, G., Chechik, V., Ionita, P., Godt, A., Zimmermann, H., Banham, J., Timmel, C. R., Hilger, D., and Jung, H. DeerAnalysis2006 - a comprehensive software package for analyzing pulsed ELDOR data. *APPLIED MAGNETIC RESONANCE* **30**
64. Sakmann, B., and Neher, E. (1984) Patch clamp techniques for studying ionic channels in excitable membranes. *Annual review of physiology* **46**, 455-472

65. Schneider, F. (2014) Design and electrophysiological characterization of rhodopsin-based optogenetic tools - Entwicklung und elektrophysiologische Charakterisierung von rhodopsinbasierten, optogenetischen Werkzeugen. Mathematisch-Naturwissenschaftliche Fakultät I
66. Klare, J. P., Bordignon, E., Engelhard, M., and Steinhoff, H. J. (2004) Sensory rhodopsin II and bacteriorhodopsin: light activated helix F movement. *Photochemical & photobiological sciences : Official journal of the European Photochemistry Association and the European Society for Photobiology* **3**, 543-547
67. Omasits, U., Ahrens, C. H., Muller, S., and Wollscheid, B. (2014) Protter: interactive protein feature visualization and integration with experimental proteomic data. *Bioinformatics* **30**, 884-886
68. Furutani, Y., Sudo, Y., Wada, A., Ito, M., Shimono, K., Kamo, N., and Kandori, H. (2006) Assignment of the Hydrogen-Out-Of-Plane and -in-Plane Vibrations of the Retinal Chromophore in the K Intermediate of pharaonis Phoborhodopsin†. *Biochemistry* **45**, 11836-11843
69. Moh, P. P., Fiamingo, F. G., and Alben, J. O. (1987) Conformational sensitivity of .beta.-93 cysteine sulfhydryl to ligation of hemoglobin observed by FT-IR spectroscopy. *Biochemistry* **26**, 6243-6249
70. Arora, A., and Tamm, L. K. (2001) Biophysical approaches to membrane protein structure determination. *Current opinion in structural biology* **11**, 540-547
71. Spakowski, C. (2012) Herstellung und biophysikalische Untersuchungen von cystein-reduzierten Channelrhodopsin-2 Varianten. in *Fachbereich Physik*, Freie Universität Berlin
72. Krause, N., Engelhard, C., Heberle, J., Schlesinger, R., and Bittl, R. (2013) Structural differences between the closed and open states of channelrhodopsin-2 as observed by EPR spectroscopy. *FEBS letters* **587**, 3309-3313
73. Grigor'ev, I. A., Mitasov, M. M., Shchukin, G. I., and Volodarskii, L. B. (1979) Use of Raman spectroscopy to identify nitroxyl group of cyclic nitroxyl radicals. *Russ Chem Bull* **28**, 2421-2424
74. Rintoul, L., Micallef, A. S., and Bottle, S. E. (2008) The vibrational group frequency of the N-O* stretching band of nitroxide stable free radicals. *Spectrochimica acta. Part A, Molecular and biomolecular spectroscopy* **70**, 713-717
75. Rothblat, G. H., and Phillips, M. C. (2010) High-density lipoprotein heterogeneity and function in reverse cholesterol transport. *Current opinion in lipidology* **21**, 229-238
76. Denisov, I. G., Grinkova, Y. V., Lazarides, A. A., and Sligar, S. G. (2004) Directed Self-Assembly of Monodisperse Phospholipid Bilayer Nanodiscs with Controlled Size. *Journal of the American Chemical Society* **126**, 3477-3487
77. Li, Y., Kijac, A. Z., Sligar, S. G., and Rienstra, C. M. (2006) Structural analysis of nanoscale self-assembled discoidal lipid bilayers by solid-state NMR spectroscopy. *Biophysical journal* **91**, 3819-3828
78. Bayburt, T. H., and Sligar, S. G. (2010) Membrane protein assembly into Nanodiscs. *FEBS letters* **584**, 1721-1727
79. Bayburt, T. H., Grinkova, Y. V., and Sligar, S. G. (2006) Assembly of single bacteriorhodopsin trimers in bilayer nanodiscs. *Archives of biochemistry and biophysics* **450**, 215-222
80. Keller, S. L., Radhakrishnan, A., and McConnell, H. M. (2000) Saturated Phospholipids with High Melting Temperatures Form Complexes with Cholesterol in Monolayers. *The Journal of Physical Chemistry B* **104**, 7522-7527

81. Ritchie, T. K., Grinkova, Y. V., Bayburt, T. H., Denisov, I. G., Zolnerciks, J. K., Atkins, W. M., and Sligar, S. G. (2009) Chapter 11 - Reconstitution of membrane proteins in phospholipid bilayer nanodiscs. *Methods in enzymology* **464**, 211-231
82. Wilkins, M. R., Gasteiger, E., Bairoch, A., Sanchez, J. C., Williams, K. L., Appel, R. D., and Hochstrasser, D. F. (1999) Protein identification and analysis tools in the ExPASy server. *Methods in molecular biology* **112**, 531-552
83. Mach, H., Middaugh, C. R., and Lewis, R. V. (1992) Statistical determination of the average values of the extinction coefficients of tryptophan and tyrosine in native proteins. *Analytical biochemistry* **200**, 74-80
84. Timmel, C. R., and Harmer, J. R. (2014) Structural Information from Spin-Labels and Intrinsic Paramagnetic Centres in the Biosciences Preface. *Struct Bond* **152**, V-Vii
85. Rehorek, M., and Heyn, M. P. (1979) Binding of all-trans-retinal to the purple membrane. Evidence for cooperativity and determination of the extinction coefficient. *Biochemistry* **18**, 4977-4983
86. Ritter, E., Stehfest, K., Berndt, A., Hegemann, P., and Bartl, F. J. (2008) Monitoring light-induced structural changes of Channelrhodopsin-2 by UV-visible and Fourier transform infrared spectroscopy. *The Journal of biological chemistry* **283**, 35033-35041
87. Polyhach, Y., Bordignon, E., and Jeschke, G. (2011) Rotamer libraries of spin labelled cysteines for protein studies. *Physical Chemistry Chemical Physics* **13**, 2356-2366
88. Del Val, C., Royuela-Flor, J., Milenkovic, S., and Bondar, A. N. (2014) Channelrhodopsins: a bioinformatics perspective. *Biochimica et biophysica acta* **1837**, 643-655
89. Volz, P.[#], Krause, N.[#], Balke, J., Schneider, C., Walter, M., Schneider, F., Schlesinger, R., and Alexiev, U. (2016) Light and pH-induced changes in structure and accessibility of transmembrane helix B and its immediate environment in Channelrhodopsin-2. *The Journal of biological chemistry*
90. Gaiko, O., and Dempski, R. E. (2013) Transmembrane domain three contributes to the ion conductance pathway of channelrhodopsin-2. *Biophysical journal* **104**, 1230-1237
91. Lorenz-Fonfria, V. A., Muders, V., Schlesinger, R., and Heberle, J. (2014) Changes in the hydrogen-bonding strength of internal water molecules and cysteine residues in the conductive state of channelrhodopsin-1. *J Chem Phys* **141**, 22D507
92. Ogren, J. I., Yi, A., Mamaev, S., Li, H., Lugtenburg, J., DeGrip, W. J., Spudich, J. L., and Rothschild, K. J. (2015) Comparison of the structural changes occurring during the primary phototransition of two different channelrhodopsins from Chlamydomonas algae. *Biochemistry* **54**, 377-388
93. Rozenberg, M., Loewenschuss, A., and Marcus, Y. (2000) An empirical correlation between stretching vibration redshift and hydrogen bond length. *Physical Chemistry Chemical Physics* **2**, 2699-2702
94. Lorenz-Fonfria, V. A., Furutani, Y., and Kandori, H. (2008) Active internal waters in the bacteriorhodopsin photocycle. A comparative study of the L and M intermediates at room and cryogenic temperatures by infrared spectroscopy. *Biochemistry* **47**, 4071-4081
95. Ullrich, S., Gueta, R., and Nagel, G. (2013) Degradation of channelopsin-2 in the absence of retinal and degradation resistance in certain mutants. *Biological chemistry* **394**, 271-280

96. Berndt, A., Schoenenberger, P., Mattis, J., Tye, K. M., Deisseroth, K., Hegemann, P., and Oertner, T. G. (2011) High-efficiency channelrhodopsins for fast neuronal stimulation at low light levels. *Proceedings of the National Academy of Sciences* **108**, 7595-7600

97. Wietek, J., Wiegert, J. S., Adeishvili, N., Schneider, F., Watanabe, H., Tsunoda, S. P., Vogt, A., Elstner, M., Oertner, T. G., and Hegemann, P. (2014) Conversion of Channelrhodopsin into a Light-Gated Chloride Channel. *Science* **344**, 409-412

98. Bruun, S., Naumann, H., Kuhlmann, U., Schulz, C., Stehfest, K., Hegemann, P., and Hildebrandt, P. (2011) The chromophore structure of the long-lived intermediate of the C128T channelrhodopsin-2 variant. *FEBS letters* **585**, 3998-4001

99. Curnow, P., and Booth, P. J. (2010) The contribution of a covalently bound cofactor to the folding and thermodynamic stability of an integral membrane protein. *Journal of molecular biology* **403**, 630-642

100. Mors, K., Roos, C., Scholz, F., Wachtveitl, J., Dotsch, V., Bernhard, F., and Glaubitz, C. (2013) Modified lipid and protein dynamics in nanodiscs. *Biochimica et biophysica acta* **1828**, 1222-1229

101. Sattig, T. (2014) Selektion und Charakterisierung funktioneller Channelrhodopsin-2-Mutanten zur Studie von lichtinduzierten Konformationsänderungen. in *Fachbereich Biochemie*, Goethe-Universität, Frankfurt am Main

102. Sattig, T., Rickert, C., Bamberg, E., Steinhoff, H. J., and Bamann, C. (2013) Light-induced movement of the transmembrane helix B in channelrhodopsin-2. *Angewandte Chemie* **52**, 9705-9708

103. Pescitelli, G., Kato, H. E., Oishi, S., Ito, J., Maturana, A. D., Nureki, O., and Woody, R. W. (2014) Exciton circular dichroism in channelrhodopsin. *The journal of physical chemistry. B* **118**, 11873-11885

104. Richards, R., and Dempski, R. E. (2012) Re-introduction of transmembrane serine residues reduce the minimum pore diameter of channelrhodopsin-2. *PloS one* **7**, e50018

105. Hemminga, M. A., and Berliner, L. J. (2007) *ESR spectroscopy in membrane biophysics*, Springer, New York, NY

106. Sass, H. J., Schachowa, I. W., Rapp, G., Koch, M. H. J., Oesterhelt, D., Dencher, N. A., and Büldt, G. (1997) The tertiary structural changes in bacteriorhodopsin occur between M states: X-ray diffraction and Fourier transform infrared spectroscopy. *The EMBO journal* **16**, 1484-1491

107. Dencher, N. A., Dresselhaus, D., Zaccai, G., and Buldt, G. (1989) Structural changes in bacteriorhodopsin during proton translocation revealed by neutron diffraction. *Proceedings of the National Academy of Sciences of the United States of America* **86**, 7876-7879

108. Muller, M., Bamann, C., Bamberg, E., and Kuhlbrandt, W. (2015) Light-induced helix movements in channelrhodopsin-2. *Journal of molecular biology* **427**, 341-349

109. Altenbach, C., Kusnetzow, A. K., Ernst, O. P., Hofmann, K. P., and Hubbell, W. L. (2008) High-resolution distance mapping in rhodopsin reveals the pattern of helix movement due to activation. *Proceedings of the National Academy of Sciences of the United States of America* **105**, 7439-7444

110. Scheerer, P., Park, J. H., Hildebrand, P. W., Kim, Y. J., Krauss, N., Choe, H. W., Hofmann, K. P., and Ernst, O. P. (2008) Crystal structure of opsin in its G-protein-interacting conformation. *Nature* **455**, 497-502

111. Farrens, D. L., Altenbach, C., Yang, K., Hubbell, W. L., and Khorana, H. G. (1996) Requirement of rigid-body motion of transmembrane helices for light activation of rhodopsin. *Science* **274**, 768-770

112. Radzwill, N., Gerwert, K., and Steinhoff, H. J. (2001) Time-resolved detection of transient movement of helices F and G in doubly spin-labeled bacteriorhodopsin. *Biophysical journal* **80**, 2856-2866

113. Wegener, A. A., Chizhov, I., Engelhard, M., and Steinhoff, H. J. (2000) Time-resolved detection of transient movement of helix F in spin-labelled pharaonis sensory rhodopsin II. *Journal of molecular biology* **301**, 881-891

114. Matulef, K., and Maduke, M. (2007) The CLC 'chloride channel' family: revelations from prokaryotes. *Molecular membrane biology* **24**, 342-350

115. Tombola, F., Ulbrich, M. H., Kohout, S. C., and Isacoff, E. Y. (2010) The opening of the two pores of the Hv1 voltage-gated proton channel is tuned by cooperativity. *Nat Struct Mol Biol* **17**, 44-50

Acknowledgements

First of all I like to thank my supervisors Dr. Ramona Schlesinger and Prof. Joachim Heberle for all the kindhearted, considerate support and helpful advice. As well I like to thank enabling group activities as the “Winterseminar” in Klosters, which helped to create a pleasant, cooperative working atmosphere in the research group. Concerning the latter like to express my appreciation to all my colleagues in the AG Schlesinger and Heberle. I also like to thank Prof. Robert Bittl for taking part in the PhD examination committee.

Big thanks to Kirsten Hoffmann and Dorothea Heinrich for their hands-on and also moral support. I am also very thankful to Maria Walter for helping me out in the lab-work during the last period of my PhD.

A special thanks to Dr. Victor Lórenz Fonfria for many fruitful discussions and advice.

I like to thank Christopher Engelhard for the close collaboration and the insights into the EPR methodology.

I am grateful to Franziska Schneider and Peter Hegemann for the electrophysiological measurements.

My gratitude goes as well to Dr. Ulrike Alexiev and her research group for the exciting, complementary results of our collaboration.

I like to thank Christian Spakowski and Christopher Mielack from AG Bondar for discussing and sharing their results on molecular dynamics simulation of ChR2 with me.

Thanks goes also to Tom Resler, Dr. Sven Stripp, Mattia Saita and Bernd Schulz for advice and help on the spectroscopic techniques.

And last but not least I am very obliged to my parents for constant and unconditional support of my life (also outside the ivory tower;-).

Appendix

Abstract

Channelrhodopsins (ChRs) are ion channels that regulate phototaxis of green algae. (1,2). The functional unit comprises a retinal chromophore embedded in seven transmembrane helices (7TM). Up to now, ChRs are the only light gated ion channels found in nature. After the discovery in 2002 (3) the ChRs were soon exploited as a tool to trigger nerve cell action potentials (4). A new field of research, named optogenetics, was established. Since ChRs undergo a cyclic reaction triggered by light they can be investigated by a large set of different biophysical techniques and hence are ideal candidates to study the structure/function relationship on molecular level.

In this work three functional ChR2 cysteine-variants were engineered to enable the site specific labeling of the cytosolic end of helix B and additionally helix F or C. The labeling positions can be investigated in the ground state as well as in the accumulated open state, P_3^{530}. The variants were spin-labeled and subjected to pulsed electron double resonance (PELDOR) measurements. Thereby, an outward displacement of the cytosolic side of helix B and F in the open state could be observed. The helix B displacement persist also in the desensitized state, P_4^{480}. These results strengthen the hypothesis of a prolongation of the pore between helices A, B, C and G (13,28,33) by the observed outward movement of helix B in the open state. However, as suggested earlier (21,35), the major structural changes are to some extent decoupled from the on-gating, since the outward displacement of helix B persists in the desensitized state. Furthermore, we set the stage for the quantitative determination of the helix F movement, which is currently underway.

The results of this thesis will help to guide the developments and benchmark future open state models.

Kurzzusammenfassung

Kanalrhodopsine (KR) sind Ionenkanäle, die die Phototaxis von Grünalgen steuern (1,2). Die funktionale Einheit umfasst ein Retinal-Chromophor, das in sieben Transmembranhelices eingebettet ist. Kanalrhodopsine sind die einzigen, natürlichen, lichtgesteuerten Ionenkanäle, die bisher entdeckt wurden. Nach ihrer Entdeckung 2002 (3) wurde bald erkannt, dass mit ihnen Aktionspotentiale in Nervenzellen durch Licht ausgelöst werden können (4). Da KR eine zyklische Reaktion durchlaufen, die nichtinvasiv durch Licht ausgelöst wird und größere strukturelle Veränderungen umfasst, eignen sie sich ideal um an ihnen Struktur-Funktions-Zusammenhänge biophysikalisch zu ergründen.

In dieser Arbeit wurden drei aktive KR-Cysteinvarianten hergestellt, die spezifisch an dem zytosolischen Ende der Helix B und zusätzlich an Helix C oder F markiert werden können. Die markierten Positionen können im Grundzustand oder im akkumulierten offenen Zustand, P_3^{530}, untersucht werden. Die KR-Varianten wurden spinmarkiert und in gepulsten Elektronendoppelresonanzmessungen untersucht. Die Messungen belegen eine Auswärtsbewegung der zytosolischen Seite von Helix B und F im offenen Zustand. Auch im desensitivierten Zustand, P_4^{480}, bleibt Helix B nach außen versetzt. Die Ergebnisse untermauern die Hypothese einer Tunnelöffnung zwischen den Helices A, B, C und G (13,28,33). Gleichzeitig deuten die Resultate darauf hin, dass die großen Konformationsänderungen, wie bereits vermutet (21,35), zu einem gewissen Grad von der Tunnelöffnung entkoppelt sind, da Helix B auch im desensitivierten Zustand nach außen versetzt bleibt. Weiterhin wurde die Grundlage für eine quantitative Bestimmung der Helix F Bewegung bereitet, welche ein weiterhin laufendes Projekt ist.

Die Ergebnisse dieser Arbeit werden helfen Modelle des offenen Kanals zu entwickeln und zu beurteilen.

Selbstständigkeitserklärung

Hiermit versichere ich für diese Dissertation mit dem Titel

„Structural rearrangements upon opening of Channelrhodopsin-2“

alle Hilfsmittel und Hilfen angeben zu haben und auf dieser Grundlage die Arbeit selbstständig verfasst zu haben. Weiterhin versichere ich, dass diese Arbeit nicht schon einmal in einem früheren Promotionsverfahren angenommen oder als ungenügend beurteilt wurde.

Berlin, den 22.01.2016

Nils Krause

Curriculum vitae

For reasons of data protection, the curriculum vitae is not published in the electronic version.

PUBLICATIONS

Published:

1. ter Beek, J., Krause, N., Reimann, J., Lachmann, P., and Ädelroth, P. (2013) The nitric-oxide reductase from Paracoccus denitrificans uses a single specific proton pathway. The Journal of biological chemistry 288, 30626-30635

2. Krause, N.[#], Engelhard, C.[#], Heberle, J., Schlesinger, R., and Bittl, R. (2013) Structural differences between the closed and open states of channelrhodopsin-2 as observed by EPR spectroscopy. FEBS letters 587, 3309-3313

3. Lorenz-Fonfria, V. A., Resler, T., Krause, N., Nack, M., Gossing, M., Fischer von Mollard, G., Bamann, C., Bamberg, E., Schlesinger, R., and Heberle, J. (2013) Transient protonation changes in channelrhodopsin-2 and their relevance to channel gating. Proceedings of the National Academy of Sciences of the United States of America 110, E1273-1281

4. Salomonsson, L., Reimann, J., Tosha, T., Krause, N., Gonska, N., Shiro, Y., and Ädelroth, P. (2012) Proton transfer in the quinol-dependent nitric oxide reductase from Geobacillus stearothermophilus during reduction of oxygen. Biochimica et biophysica acta 1817, 1914-1920

5. Ter Beek, J., Krause, N., and Adelroth, P. (2016) Investigating the Proton Donor in the NO Reductase from Paracoccus denitrificans. *PloS one* **11**, e0152745

6. Volz, P.[#], Krause, N.[#], Balke, J., Schneider, C., Walter, M., Schneider, F., Schlesinger, R., and Alexiev, U. (2016) Light and pH-induced changes in structure and accessibility of transmembrane helix B and its immediate environment in Channelrhodopsin-2. *The Journal of biological chemistry*

[#]: Both authors contributed equally.

List of Tables

List of Figures

List of Abbreviations

4pELDOR	4-Pulse Electron Double Resonance
amp	Ampicillin
C. reinhardtii	*Chlamydomonas reinhardtii*
ChR	Channelrhodopsin
ChR1	Channelrhodopsin-1
ChR2	Channelrhodopsin-2
CW	Continuous Wave
DM	n-Decyl-β-D-Maltopyranoside
DMPC	1,2-dimyristoyl-*sn*-glycero-3-phosphocholine
DMSO	Dimethyl Sulfoxide
DNA	Deoxyribonucleic acid
E. coli	*Escherichia coli*
EPR	Electron Paramagnetic Resonance
FTIR	Fourier transformed Infra Red
gDNA	genomic Deoxyribonucleic acid
GPCR	GTP-binding Protein Coupled Receptors
HEK cell	Human Embryonic Kidney 293 cell
IR	Infra Red
km	Kanamycin
m/V	mass/Volume
MSP	Membrane Scaffold Protein
MTSL	(1-Oxyl-2,2,5,5-tetramethyl-Δ3-pyrroline-3-methyl) Methanethiosulfonate
P. pastoris	*Pichia pastoris*
PCR	Polymerase Chain Reaction
PELDOR	Pulsed Electron Double Resonance
POPC	1-palmitoyl-2-oleoyl-sn-glycero-3-phosphocholine (POPC)
RT	Room Temperature
UV/Vis	Ultra Violet/visible
UV/Vis	Ultra Violet
V/V	Volume/Volume
VGCC	Voltage Gated Cation Channel
WT	wild type